Electromechanical Characterization of Quasi-One Dimensional Nanostructures of Silicon, Carbon, and Molybdenum Disulfide via Symmetry-Adapted Tight-Binding Molecular Dynamics

A DISSERTATION
SUBMITTED TO THE FACULTY OF THE GRADUATE SCHOOL
OF THE UNIVERSITY OF MINNESOTA
BY

Dong-Bo Zhang

IN PARTIAL FULFILLMENT OF THE REQUIREMENTS
FOR THE DEGREE OF
DOCTOR OF PHILOSOPHY

Traian Dumitrică
William W. Gerberich

November 2010

Acknowledgements

Since September 2005, I have been receiving intensive training from the Materials Science program in the Department of Chemical Engineering and Materials Science. At this time, I would like to thank a number of people for their great help and contributions.

First, I would like to thank my advisors, Professor Traian Dumitrică and William W. Gerberich. I would also like to acknowledge insightful discussions with Professor Renata M. Wentzcovitch.

I also got help and useful suggestions from Professor Gotthard Seifert (Technische Universitaet Dresden, Germany), Professor Nan-Xian Chen (Tsinghua University & University of Science and Technology Beijing), Professor Eduardo Hernàndez (Spanish National Research Council), Professor Philip B. Allen (SUNY Stony Brook), Professor Sanford Lipsky (Chemistry, University of Minnesota), Professor J. Woods Halley (Physics, University of Minnesota), Professor Matteo Cococcioni (Chemical Engineering & Materials Science, University of Minnesota), Professor Richard D. James (Aerospace Engineering and Mechanics, University of Minnesota), Professor Valentin N. Popov (University of Sofia, Bulgaria), Professor Shan-Ying Wang (Tsinghua University).

Finally, I would like to thank the Dumitrică's group members, including Paolo Valentini, Ramesh Raghupathy, Ming Hua, Shaogang Hao, Evgeniya Akatyeva, and Ilia Nikiforov for helping me get up to speed with the available computational facilities. Finally, I would like to thank to my friends and family for support.

Abstract

With a newly developed symmetry-adapted tight-binding molecular dynamics (MD) capability, we performed microscopic calculations on a variety of quasi-one dimensional silicon, carbon, and molybdenum disulfide nanostructures. In symmetry-adapted MD the helical symmetry instead of the standard translational symmetry is used. In the considered nanostructures, equivalent calculations can now be performed with a substantial smaller, in terms of the number of atoms, repeating domain. The symmetry-adapted method was utilized in the studied highlighted below.

The stability of the most promising ground state candidate silicon nanowires with less than 10 nm in diameter was comparatively studied with with nonorthogonal tight-binding and classical potential models. The computationally expensive tight-binding treatment becomes tractable due to the substantial simplifications introduced by the presented symmetry-adapted scheme. It indicates that the achiral polycrystalline of fivefold symmetry and the hexagonal (wurtzite) wires of threefold symmetry are the most favorable quasi-one-dimensional silicon arrangements. Quantitative differences with the classical model description are noted over the whole diameter range. Using a Wulff energy decomposition approach it is revealed that these differences are caused by the inability of the classical potential to accurately describe the interaction of Si atoms on surfaces and strained morphologies.

The elastic response for a large catalog of carbon nanotubes subjected to axial and torsional strain was next derived from atomistic calculations that rely on an accurate tight-binding description of the covalent binding. The application of the computationally expensive quantum treatment is possible due to the simplification in the number of atoms introduced by accounting for the helical and angular symmetries exhibited by the elastically deformed nanotubes. The elasticity of nanotubes larger than 1.25 nm in diameter can be represented with an isotropic elastic continuum.

The torsional plastic response of single-walled carbon nanotubes is studied with tight-binding objective molecular dynamics. In contrast with plasticity under

elongation and bending, a torsionally deformed carbon nanotube can slip along a nearly axial helical path, which introduces a distinct $(+1,-1)$ change in wrapping indexes. The low energy realization occurs without loss in mass via nucleation of a 5-7-7-5 dislocation dipole, followed by glide of 5-7 kinks. The possibility of nearly axial glide is supported by the obtained dependence of the plasticity onset on chirality and handedness and by the presented calculations showing the energetic advantage of the slip path and of the initial glide steps.

Symmetry-adapted MD combined with density-functional-based tight-binding made possible to compute chiral nanotubes as axial-screw dislocations. This enabled the surprising revelation of a large catalog of MoS_2 nanotubes that lack the prescribed translational symmetry and exhibit chirality-dependent electronic band-gaps and elastic constants. Helical symmetry emerges as the natural property to rely on when studying quasi-one dimensional nanomaterials formally derived or grown via screw dislocations.

The nonlinear elastic response of carbon nanotubes in torsion was derived with the symmetry-adapted MD and a density-functional-based tight-binding model. The critical strain beyond which tubes behave nonlinearly, the most favorable rippling morphology, and the twist- and morphology-related changes in fundamental band gap were identified from a rigorous atomistic description. There is a sharply contrasting behavior in the electronic response: while in single-walled tubes the band-gap variations are dominated by rippling, multiwalled tubes with small cores exhibit an unexpected insensitivity. Results are assistive for experiments performed on nanotubes-pedal devices.

Despite its importance, little is known about how complex deformation modes alter the intrinsic electronic states of carbon nanotubes. We considered the rippling deformation mode characterized by helicoidal furrows and ridges and elucidate that a new intralayer strain effect rather than the known bilayer coupling and σ-π orbital mixing effects dominates its gapping. When an effective shear strain is used, it is possible to link both the electrical and the mechanical response of the complex rippled morphology to the known behavior of cylindrical tubes.

Moving on to graphene, to describe the strain stored in helical nanoribbons, we supplement the standard elasticity concepts with an effective tensional strain. Using π-orbital tight binding and objective molecular dynamics coupled with density functional theory, we show that twisting couples the frontier conduction and valence bands, resulting in band-gap modulations. In spite of the edges and ridges of the helical nanoribbons, from the effective strain perspective these band-gap modulations appear strikingly similar with those exhibited by the seamless carbon nanotubes.

Contents

List of Figures

List of Tables

Biographical Sketch

I was born in November 1979 in Guotan, a town located in the province of Henan in central China. The main occupations in my hometown are cultivation of sesame and making sesame oil. I attended my primary school and middle school in this town while for the high school I commuted to the county of Tanghe, about 20 miles away from home.

In the summer of 1998, I took the entrance examination to College and I was admitted into the Applied Physics Program in the Department of Physics at the University of Science and Technology, Beijing, which is considered a top school in my country. Keeping a good standing in the undergraduate program, I was recommended to enter the graduate school to study condensed matter physics. I received my M.S. degree in the summer of 2005. During both my undergraduate and graduate studies I carried out my research in the lab named "State Key Laboratory of Material Simulation and Design" supported by the Ministry of Science and Technology of China, and directed by Professor Nan-Xian Chen. He and his collaborator, Professor Jiang Shen, were my M.S. thesis advisors for the topic titled "First-principles study of lanthanum clusters".

In 2005, I entered the Ph.D grogram of Materials Science in the Chemical Engineering and Materials Science at University of Minnesota. I am advised by Professor Traian Dumitrică (Mechanical Engineering) and Professor William W. Gerberich (Chemical Engineering and Materials Science). When I started my research, I found my interests to be in quantum mechanical computations. I have developed a full *spd* Symmetry-Adapted Tight-Binding code, as well as Wulff energy-decomposition and effective strain theories aimed at understanding the physics hidden in simulation results. My work was conducted in the Computational Nanomechanics Laboratory located in the Department of Mechanical Engineering. My simulations were carried out at the Minnesota Supercomputing Institute. While research took most of my time, in the free time I enjoyed playing table tennis (ping-pong) and watching american classic movies.

Chapter 1

Introduction

The discovery of quasi one-dimensional organizations of matter with distinct shapes - nanotubes [9, 10], nanowires [11, 12], and nanoribbons [13, 14] - opened a new frontier in science and engineering. Understanding the behavior of these structures is not only of fundamental but also of practical importance because by capitalizing on the science emerging from the newly accessible size range, engineers can develop technologies that will benefit humankind. The success of these nanotechnologies depends on our ability to understand and control the nanoscale mechanics. As experimental difficulties are numerous on this small scale, computer simulations emerge as a powerful predictive tool with great effects on technological innovation.

It should be noted that atomistic simulation methods are required at the nanoscale. However, because of the structure of interest extent over several micrometers or more in one direction, a full atomistic treatment is prohibitive. This situation demands new simulation methods and the vision is that nanoscale modeling will be achieved through a multiscale approach, where the continuum emerges from a precise, quantum mechanical description of the atomic scale [15].

The first important step to achieve multiscale modeling is designing an atomistic scheme to compute the nanomechanical response with high accuracy. Based on the obtained result, one can further construct a continuum model of the nano objects. The research proposed here is addressing this first critical step by implementing

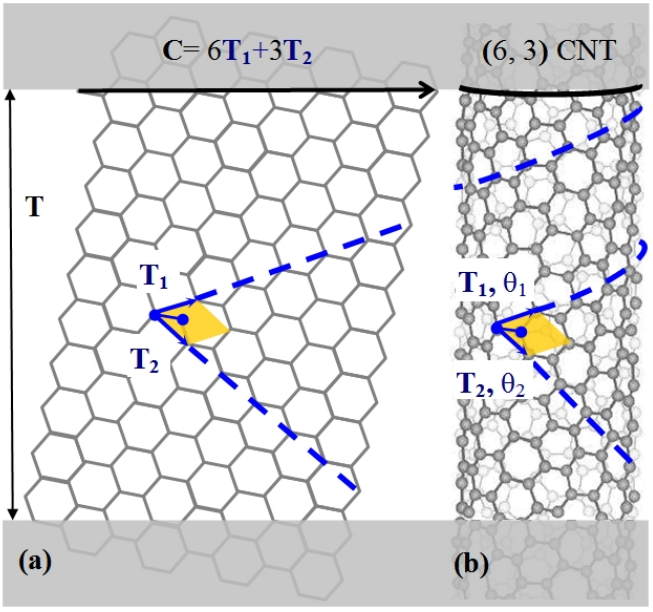

FIGURE 1.1: Translational cell of a (6,3) nanotube in the (a) unfolded and (b) folded representation.

a new *symmetry-adapted microscopic modeling approach*, which is applicable to a large class of quasi one-dimensional nanostructures.

Since computing nanomechanical response requires relatively large systems (at least a few hundred of atoms), computationally affordable but less accurate classical atomistic treatments of the atomic scale are heavily adopted [5, 16–20]. To date, only multiscale classical atomistic-to-continuum bridging is achieved [21–28]. Unfortunately, the inaccuracy of the "parent" atomistic model directly transfers to the continuum one and this severely limits our predictive power. The accurate atomistic tools to study the properties of matter are the methods that explicitly account for the quantum mechanics of the electrons. Originally developed in the context of quantum chemistry and condensed matter physics, these powerful methods combine fundamental quantum-mechanical predictive power with atomic resolution in length and time. These methods include density-functional theory [29–31] and tight-binding [32, 33] molecular dynamics.

An accurate atomistic description is highly desirable in computational nanomechanics. In order to deliver quantitative prediction, suited for further engineering use, the accurate quantum-mechanical description of chemical bonding is needed.

Furthermore, because the electronic subsystem is treated explicitly, electronic, optical or piezoelectric properties can be also derived. Unfortunately, the size range covered by quantum-mechanical methods (of a few hundred atoms) is the major impediment for using these methods in nanomechanics. (This is in spite of the face that the size limit increases rapidly due to parallel computing.)

This work does not intend to advance nanomechanics by trying to enlarge the current computational limit for number of atoms that can be treated with quantum mechanical accuracy. Instead, within the current computational limits, the main idea is to introduce a substantial simplification in the atomistic computations by making recourse to the helical symmetry of the nano objects.

The concept is illustrated in Figure 1.1 for a single walled carbon nanotube structure, which can be viewed as the result of rolling up into a seamless tube a flat sheet of graphite, called graphene. The hexagonal structure of graphene, see Figure 1.1(a), is described by translating a two-atom cell (orange shaded) along the lattice vectors $\mathbf{T_1}$ and $\mathbf{T_2}$. Rolling into a tube can be performed under various curvatures in different directions. For example, Figure 1.1(b) shows a chiral tube obtained by rolling the graphene along the circumference vector $\mathbf{C}$ having distinct components (6 and 3, respectively) along $\mathbf{T_1}$ and $\mathbf{T_2}$. Through folding, the $\mathbf{T_1}$ and $\mathbf{T_2}$ directions wind up in helixes. To describe the resulting tube structure, one must apply both translations ($\mathbf{T_1}$ and $\mathbf{T_2}$) and rotations (θ_1 and θ_2) around the tube axis to the shown two-atom cell.

When computing properties of a system with crystalline order, current implementation operating under periodic boundary condition, makes recourse to the specific translational symmetry of the structure to simplify the problem to the extent that microscopic calculations are performed on the small translational repeating cells. For example, to obtain bulk properties of graphene [Figure 1.1(a)], a calculation on the two-atom unit cell suffices [34]. However, in a system with helical symmetry the translational periodicity doesn't bring the same advantage. For example, Figure 1.1(b) shows that the translational cell of a chiral nanotube (with axial periodicity T) contains a large number of atoms. As discussed in Chapter 2, often such translational cells are even too large to allow a quantum treatment. However, calculations would become as convenient as in the flat graphene, if one can

take advantage of the helical symmetry and further reformulate the problem with augmented repetition rule to include translations and rotations.

The use of helical symmetry at the nanoscale is very much in its infancy. To date, it has attracted the interest of the research community working on carbon nanotubes [35–37]. Fortunately, the type of simplification portrayed in Figure 1.1 actually applies to a large category of quasi one-dimensional nanostructures, recently called objective structures [38, 39]. In Chapter 2 we present the structure of single-walled carbon nanotubes as the prototype structure suitable to apply the helical symmetry ideas.

In the first part, our main research objective is to develop a versatile tight-binding computational tool able to operate under the new helical boundary condition. We will call symmetry-adapted modeling, the new scheme that operates under helical boundary condition. It is not necessary to create this capability from scratch. Instead, the strategy is to implement the new helical boundary condition into an existing tight-binding solver, now able to operate with the translational periodic boundary conditions. Chapter 3 details the necessary steps that were be undertaken to modify the existing computational package *Trocadero* [40]. This code is well tested and it is intensely used in our group [41]. By using this code we inherited important features such as atomistic models for various chemical elements as well as numerical algorithms (such as dynamics under constant temperature) that can be immediately used in conjunction with the new symmetry-adapted boundary conditions. Some of these features are summarized in the last section of this chapter.

In the second part, our goal is to employ the created computational capability to obtain the accurate modeling and the nanomechanical response of various one-dimensional nanostructures to various types of deformations. Besides the immediate interest, these results will be of great interest for multiscale modeling since such data is needed to construct and validate continuum models (However, this is aspect is beyond the scope of the present work).

In Chapter 4 we study the stability of the most promising ground state candidate silicon nanowires. We demonstrate that the achiral polycrystalline of fivefold symmetry and the hexagonal (wurtzite) wires of threefold symmetry are the most

favorable quasi-one-dimensional silicon arrangements. Furthermore, we highlight the inability of the classical potential to accurately describe the interaction of Si atoms on surfaces and strained morphologies.

In Chapter 5 we study the elastic properties – linear or nonlinear – of carbon nanotubes under fundamental type deformations, including tension, torsion and bending. We address the limitations of the current periodic boundary condition formulation of the atomistic methods for applying mechanical deformations. Meanwhile, we show that to compute the nanomechanical response for structures with helical symmetry, it is not essential to enlarge the size range (in terms of the number of atoms) covered with quantum-mechanical accuracy. Instead, this can be achieved through the simplifications introduced by the new scheme that performs calculations on the small repeating cells under the helical boundary condition (translations + rotations).

Chapter 6 discusses the plastic properties of carbon nanotubes. When carbon nanotubes is under tensional deformation, the onsets of dislocation can be initialed and a possible glide takes place along the near circumferential direction. On the contrary, we show that a nearly axial glide could be achieved in carbon nanotubes in torsion with symmetry-adapted MD. We find that this glide can change the index of carbon nanotubes from (n, n) to any chiral nanotubes $(n + i, n - i)$ via i steps of such glide. We also notice that this is not only for carbon nanotubes but can happen to any nanotubes structures with hexagonal wall such as MoS_2 and BN nanotubes. With this knowledge, we discover an intrinsic twist in MoS_2 nanotubes, a phenomenon hidden by imposing periodic boundary conditions.

Besides the mechanical properties, we are also interested in electronic properties of carbon nanotubes, especially in the strain-turnable electromechanical response aspects. With the one-atom-layer wall, carbon nanotubes are susceptible to helically ripple, developing helicoidal furrows and ridges. Even though the electronic structures of idealized-twist carbon nanotubes with cylindrical shape is well understood theoretically, little is known about how rippling in carbon nanotubes under mechanical manipulation, affects the electronic states. In Chapter 7, we use symmetry-adapted MD to obtain the important electromechanical data

of helical rippled carbon nanotubes in torsion. To understand the electromechanical response of this complex morphology, we introduce the new concept of *effective strain*. With the concpet, the electronic structure of helically rippled carbon nanotubes can be linked to the known electronic properties of flat graphene.

Most importantly, the *effective strain* concept can be applied to a variety of carbon nanostructures, such as graphene nanoribbons. Despite the complex helical morphology, using an *effective tensional strain*, we demonstrate that for graphene nanoribbons with armchair shaped edges, the electromechanical response appears strikingly similar with those encountered in carbon nanotubes. A detailed discussion can be found in Chapter 8.

Finally, Chapter 9 presents the conclusions of this work and suggested research directions for the future.

Chapter 2

The Structure of Carbon Nanotubes

To illustrate the special symmetries encountered at the nanoscale we discuss in this chapter the structure of single-walled carbon nanotubes (SWCNTs). A SWCNT can be regarded as a strip of graphene (a single layer of crystalline graphite) rolled into a seamless cylinder. The structural properties of SWCNT can be conveniently understood by analyzing this corresponding graphene ribbon.

2.1 Graphene

A single graphene sheet consists of sp^2-hybridized carbon atoms packed in a two-dimensional (2D) hexagonal lattice. As shown in Figure 2.1, the Cartesian coordinate system is oriented with respect to the hexagonal lattice in such a way that the armchair (A) direction lies along the x-axis and the zigzag (Z) direction along the y-axis. The graphene sheet is generated from the unit cell by the lattice vectors $\mathbf{a_1}$ and $\mathbf{a_2}$, which make an angle of 60°:

$$\begin{cases} \mathbf{a_1} = \dfrac{\sqrt{3}a}{2}\hat{\mathbf{x}} + \dfrac{a}{2}\hat{\mathbf{y}} \\ \mathbf{a_2} = \dfrac{\sqrt{3}a}{2}\hat{\mathbf{x}} - \dfrac{a}{2}\hat{\mathbf{y}}. \end{cases} \tag{2.1}$$

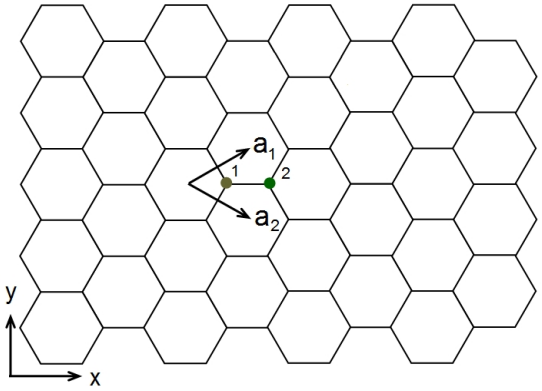

FIGURE 2.1: A single graphene sheet. The unit cell is composed of the two atoms labeled by 1 and 2. The lattice vectors $\mathbf{a_1}$ and $\mathbf{a_2}$ are shown by arrows.

Here $a = \sqrt{3}a_{CC} = 0.246$ nm is the lattice constant for the graphene sheet, $a_{CC} = 0.142$ nm is the nearest-neighbor interatomic distance, and $(\hat{\mathbf{x}}, \hat{\mathbf{y}})$ are the unitary basis vectors. The vectors $\mathbf{a_1}$ and $\mathbf{a_2}$ are shown by arrows in Figure 2.1. Note that the choice of the unit cell is arbitrary due to the random selection of the center of the coordinate system. Considering that the symmetry of the graphene sheet is described by the point group D_{6h}, we place the center of the coordinate system at the center of the hexagon through which the high-symmetry rotation axis C_6 goes. Knowing the lattice vectors $\mathbf{a_1}$ and $\mathbf{a_2}$ and the positions of the two carbon atoms labeled by 1 and 2, $\mathbf{X}_n$, we can construct the whole 2D graphene layer as:

$$\mathbf{X}_{n,(\zeta_1,\zeta_2)} = \zeta_1\mathbf{a_1} + \zeta_2\mathbf{a_2} + \mathbf{X}_n, \quad n = 1, 2. \tag{2.2}$$

where ζ_1 and ζ_2 are integer numbers labeling the various replicas of the initial unit cell containing the two atoms.

2.2 Translational Symmetry

The fundamental property of an infinitely long SWNT is its translational periodicity. The purpose of this section is to briefly describe the translational unit cell structure.

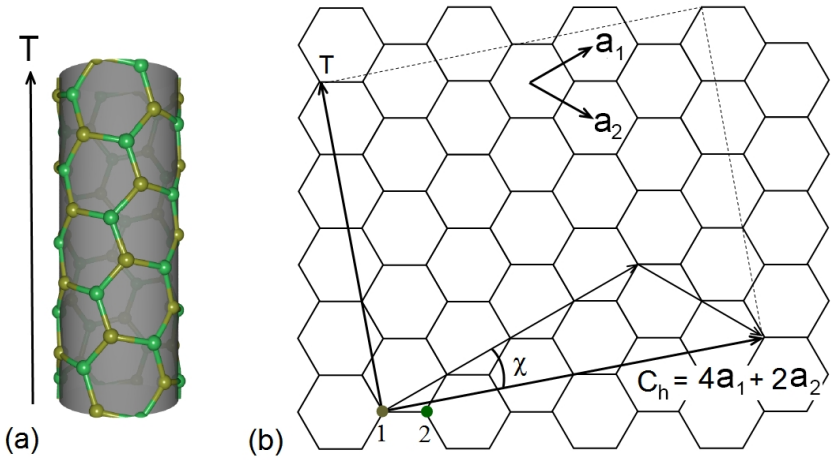

FIGURE 2.2: (a) A $(4,2)$ SWCNT. The translational periodicity vector $\mathbf{T}$ is shown. (b) The rectangle shows the translational unit cell of the $(4,2)$ SWCNT projected on the graphene sheet. The dashed lines indicate the edges of the graphite ribbon corresponding to the unrolled SWCNT. The arrows show the chiral vector $\mathbf{C}_h$ that spans the circumference of the SWCNT and the translational vector $\mathbf{T}$. The chiral angle χ is also shown.

2.2.1 The Chiral Vector

When matching a SWCNT with the corresponding nanographite ribbon, the circumference of SWCNT corresponds to the width of the nanographite ribbon. Plotted on a flat graphene sheet, this width is known as the chiral vector $\mathbf{C}_h$. When decomposed along the $\mathbf{a_1}$ and $\mathbf{a_2}$ vectors, the chiral vector writes:

$$\mathbf{C}_h = l_1\mathbf{a}_1 + l_2\mathbf{a}_2. \tag{2.3}$$

where, (l_1, l_2) is a pair of integers, which conveniently label a SWCNT. For example Figure 2.2(a) shows a (4,2) SWCNT and its unfolded graphene ribbon Figure 2.2(b) of width

$$\mathbf{C}_h = 4\mathbf{a}_1 + 2\mathbf{a}_2. \tag{2.4}$$

Further, a chiral angle labeled by χ in Figure 2.2(b), is defined as the angle made by the vector $\mathbf{C}_h$ with the graphene's lattice vector $\mathbf{a_1}$. Considering that the symmetry of the graphene sheet is described by the point group D_{6h}, all *unique* chiral vectors could be confined in a 30°-section. In other words, χ and (l_1, l_2) are in the ranges: $0° \leqslant \chi \leqslant 30°$ and $0 \leqslant l_2 \leqslant l_1$.

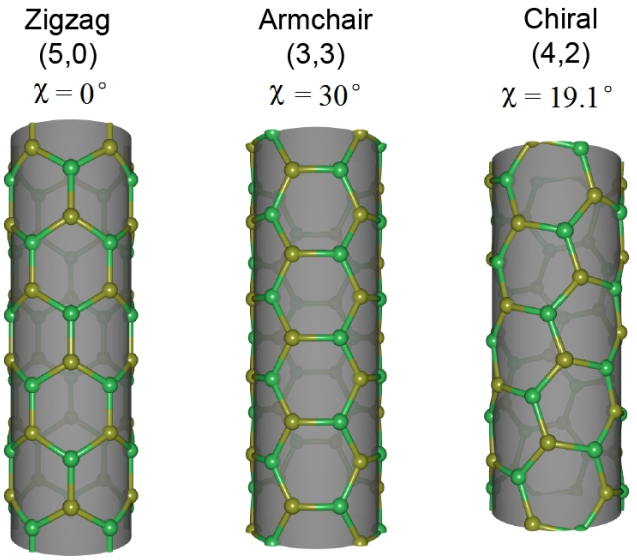

FIGURE 2.3: The schematic models of zigzag $(5,0)$, armchair $(3,3)$, and chiral $(4,2)$ SWCNTs that contain 3, 5, and 1 translational unit cells, respectively. The chiral angle χ is given for each SWCNT.

Note that at the lower limit $\chi = 0$ and $l_2 = 0$, $\mathbf{C}_h$ is along the zig-zag direction and nanotubes are labeled as $(l_1, 0)$ SWCNTs. At the upper limit $\chi = 30°$ and $l_1 = l_2$, $\mathbf{C}_h$ is along the armchair direction and nanotubes are labeled as (l_1, l_1) SWCNTs. These SWCNTs are also called achiral. The general case $0° < \chi < 30°$ or $0 < l_2 < l_1$ corresponds the chiral SWCNTs.

To visualize the concept of the SWCNT chirality, the schematic models of zigzag $(5,0)$, armchair $(3,3)$, and chiral $(4,2)$ are drawn in Figure 2.3. The length of chiral vector, which is π multiplied by the diameter of the SWCNT, as well as the chiral angle are easily related to the l_1 and l_2:

$$\begin{cases} |\mathbf{C}_h| = a\sqrt{l_1^2 + l_1 l_2 + l_2^2} \\ \chi = tan^{-1}\dfrac{\sqrt{3}l_2}{2l_1 + l_2} \end{cases} \tag{2.5}$$

2.2.2 The Translational Vector

The translational vector is defined as a vector starting from one hexagon and ending at another equivalent one in the direction perpendicular to the chiral vector

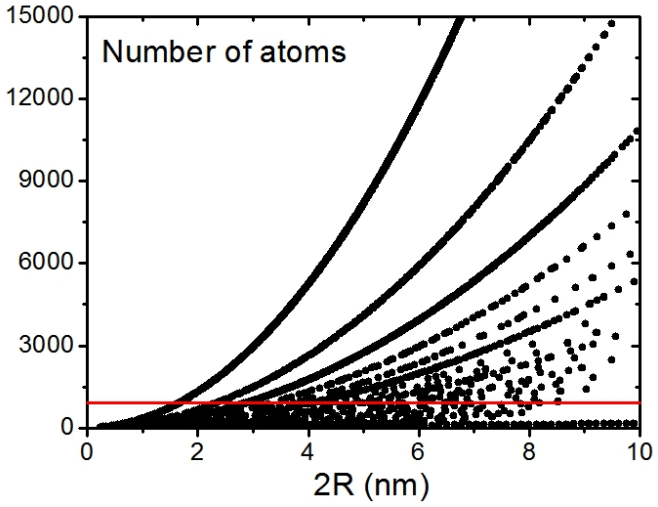

FIGURE 2.4: Number of atoms (N_0) in the translational unit cell for all (l_1, l_2) as a function of diameter. The red solid line corresponds to $N_0 = 1000$. Below this line there are about 1100 SWCNTs.

$\mathbf{C}_h$, as shown in Figure 2.2(b) for the $(4, 2)$ SWCNT. Mathematically, it can be easily obtained that:

$$\mathbf{T} = t_1\mathbf{a}_1 + t_2\mathbf{a}_2, \tag{2.6}$$

where $t_1 = (2l_2 + l_1)/d_R$, $t_2 = -(l_2 + 2l_1)/d_R$, $d_R = \mathrm{GCD}(2l_2 + l_1, l_2 + 2l_1)$ and the function $\mathrm{GCD}(i, j)$ denotes the greatest common divisor of the two integers i and j.

The rectangle area confined by chiral vector $\mathbf{C}_h$ and the translational vector $\mathbf{T}$ corresponds the translational unit cell of the SWCNT (see Figure 2.2). The number of carbon atoms in the translational unit cell N_0 is calculated by dividing this area by the area of unit cell of graphene. Using equations (2.1) (2.3), and (2.6):

$$N_0 = 2\frac{|\mathbf{C}_h \times \mathbf{T}|}{|\mathbf{a}_1 \times \mathbf{a}_2|} = \frac{4(l_1^2 + l_1 l_2 + l_2^2)}{d_R}. \tag{2.7}$$

For the $(4, 2)$ SWNT, we find $d_R = 2$, $(t_1, t_2) = (4, 5)$, and $N_0 = 56$. One can see in Figure 2.2(b) that the vector $\mathbf{T}$ connects the two equivalent hexagons in the adjacent translational unit cells. Since $\mathrm{GCD}(t_1, t_2) = 1$, the vector $\mathbf{T}$ can never connect the two inequivalent hexagons within the same translational unit cell. On the contrary, the structural indices can be arbitrary within the range $0 < l_2 < l_1$,

so that $d = \mathrm{GCD}(l_1, l_2)$ can take any values between 1 and l_1. Therefore, the chiral vector $\mathbf{C}_h$ connects d nonequivalent hexagons in the circumferential direction of the SWNT. The rotational vector in the circumferential direction, corresponding to the azimuthal symmetry of the SWCNT, is thus given by $|\mathbf{C}_h|/d$.

N_0 is plotted for (l_1, l_2) SWCNTs as a function of diameter $|\mathbf{C}_h|/\pi$. One sees that the number of carbon atoms grows rapidly with both diameter and chirality, see Figure 2.4.

Knowing the translational vector $\mathbf{T}$ and the position of the N_0 in the translational cell, $\mathbf{X}_n$, the infinite nanotube structure can be described as:

$$\mathbf{X}_{n,\zeta} = \zeta\mathbf{T} + \mathbf{X}_n, \quad n = 1, ..., N_0. \tag{2.8}$$

where integer ζ labels the various replicas of the initial translational cell containing the N_0 atoms.

2.3 Helical Symmetry of SWCNTs

The vectors $\mathbf{C}_h/d$ and $\mathbf{T}$ define the pure rotational and translational symmetries, respectively. Additionally, SWCNT has helical symmetry described by the helical vector comprised of both rotational and translational components. Exploiting this symmetry is central for the proposed work. The purpose of this section is to present an equivalent description of the infinitely long SWCNT from smaller cells, by augmenting the repeating rules from *translation* to *translation+rotation*, i.e., *screw* operations.

2.3.1 The Helical Vector Z

To describe a SWCNT, the choice for the screw operation is not unique. We propose to work with the helical vector $\mathbf{Z}$ proposed by M. Damnjanovic et al [42]. Among other possibilities, this vector has the smallest component in the axial direction of the SWNT. For the $(4, 2)$ SWNT, the helical vector satisfying this constraint is given by the vector $\mathbf{Z} = \mathbf{a}_1$, see Figure 2.5. For the general (l_1, l_2) SWCNT

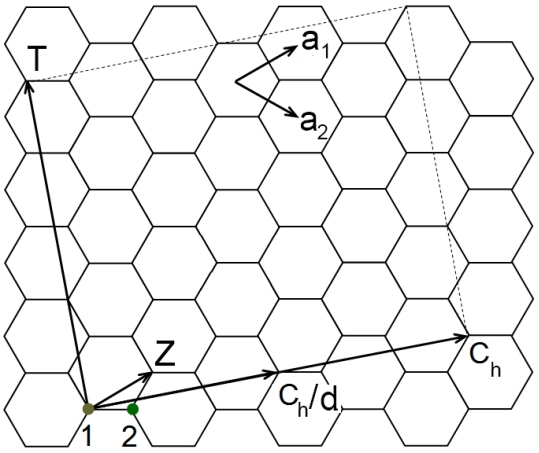

FIGURE 2.5: The unfolded representation of the (4,2) SWCNT showing the rotational vector $\mathbf{C}_h/d$, the translational vector $\mathbf{T}$, and the helical vector $\mathbf{Z}$.

we write the helical vector $\mathbf{Z}$ in the form

$$\mathbf{Z} = v_1\mathbf{a}_1 + v_2\mathbf{a}_2. \tag{2.9}$$

In order to find the unknown integers (v_1, v_2), we rewrite the aforementioned constraint in terms of vector algebra. Having the smallest component in the axial direction yields

$$|\mathbf{Z} \times \mathbf{C}_h| = d|\mathbf{a}_1 \times \mathbf{a}_2|. \tag{2.10}$$

There are d distinct vectors that satisfy this condition. Among these d vectors, choosing the one with the smallest component in the circumferential direction implies $0 < |\mathbf{Z} \times \mathbf{T}| < N_0/d|\mathbf{a}_1 \times \mathbf{a}_2|$. Substituting $\mathbf{Z}$, $\mathbf{C}_h$, and $\mathbf{T}$ into these expressions, we obtain

$$\begin{cases} l_2v_1 - l_1v_2 = d, \\ 0 < t_1v_2 - t_2v_1 < N_0/d. \end{cases} \tag{2.11}$$

These equations uniquely determines the (v_1, v_2) components of the helical vectors $\mathbf{Z}$. For the $(4, 2)$ SWNT, we find $(v_1, v_2) = (1, 0)$, as expected.

The helical vector $\mathbf{Z}$ defined by eq. (2.11) is expressed in terms of the graphene unit vectors $\mathbf{a_1}$ and $\mathbf{a_2}$. However, it is more instructive to rewrite them in terms of the SWNT unit vectors $\mathbf{C_h}$ and $\mathbf{T}$. Reversing eqs. (2.3) and (2.6) and utilizing eq. (2.7) gives $N\mathbf{a_1} = l_2\mathbf{T} - t_2\mathbf{C_h}$ and $N\mathbf{a_2} = t_1\mathbf{C_h} - l_1\mathbf{T}$. Substituting these

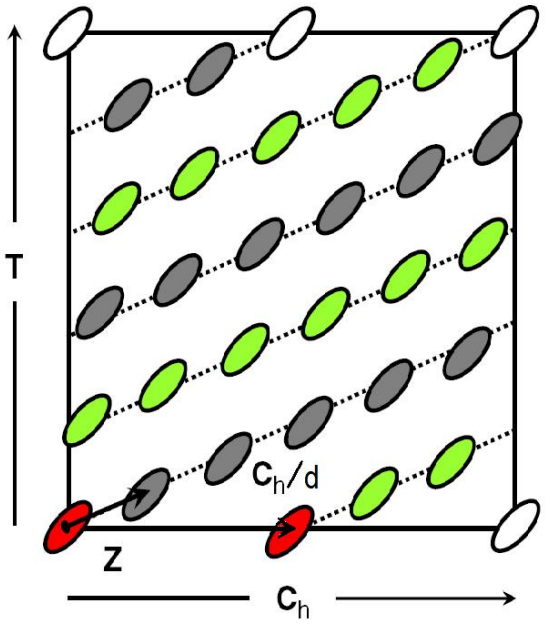

FIGURE 2.6: Constructing the translational unit cell of the (4, 2) SWCNT in the "angular-helical+translation" representation. Helical vector **Z** is applied for 14 times to the two-atom domains depicted here as filled red ellipses. The ellipse at the middle of chiral vector is obtained by applying the rotational vector $\mathbf{C}_h/2$ on the red ellipse at the origin. Once the translational unit cell is obtained, the infinite SWCNT is constructed by repeated translations.

expressions into eq. (2.9) and using eq. (2.11) one finds:

$$\mathbf{Z} = \frac{2W}{N_0}\mathbf{C_h} + \frac{2d}{N_0}\mathbf{T}, \tag{2.12}$$

where the new quantity $W = t_1 v_2 - t_2 v_1$ is defined. For the $(4, 2)$ SWNT, we obtain W = 5.

We next present two possibilities for generating the whole SWCNT structure from a reduced unit cell composed of only two atoms.

2.3.2 SWCNT in the "Angular-Helical+Translation" Representation

Figure 2.6 vividly illustrates how a (4, 2) SWCNT can be generated by applying the rotational vector $\mathbf{C}_h/d$, the helical vector **Z**, and translational vector **T**, hence

the name "angular-helical+translation" representation. For simplicity the reduced two-atom domain was lumped into the red ellipse the lower-left corner. Note that a $(4, 2)$ SWCNT has a two-fold rotational symmetry ($d = 2$) and 28 two-atom pairs in the translational unit cell. By applying once a $\mathbf{C}_h/d$ vector on the red ellipse at the origin, another red ellipse is obtained at the end of $\mathbf{C}_h/d$. Next, applying the helical vector $\mathbf{Z}$ for 14 times on these two red ellipse, all shown gray and green ellipses are obtained. This way the translational unit cell is generated. Finally, the infinite SWCNT can be obtained by applying translations $\mathbf{T}$ on the translational unit cell.

Mathematically, a SWCNT could be described in the "angular-helical+translation" representation, with

$$\mathbf{X}_{n,(\zeta,\zeta_1,\zeta_2)} = \mathbf{R}_2^{\zeta_2}\,\mathbf{R}_1^{\zeta_1}\mathbf{X}_n + \zeta_1\mathbf{T}_1 + \zeta\mathbf{T}. \tag{2.13}$$

Index n runs over the two atoms at locations $\mathbf{X}_n$ inside the reduced domain, while integers ζ, ζ_1 and ζ_2 label various replicas of this block. Note that both ζ_1 and ζ_2 take finite values and $-\infty < \zeta < \infty$. As before, $\mathbf{T}$ is the axial translational vector. Rotational matrix $\mathbf{R}_1$ of angle $\theta_1 = 360^\circ \cdot 2W/N_0$ and the axial vector $\mathbf{T}_1 = 2d\mathbf{T}/N_0$ indicate a screw transformation corresponding to $\mathbf{Z}$ applied to the reduced domain while the rotational matrix $\mathbf{R}_2$ indicates an axial rotation of angle $\theta_2 = 360^\circ/d$ corresponding to $\mathbf{C}_h/d$. For example, for $(4, 2)$ SWCNT where $W = 5$, $d = 2$ and $N_0 = 56$, we have $\theta_1 = 64.28^\circ$ and $\theta_2 = 180^\circ$.

2.3.3 SWCNT in the "Angular-Helical" Representation

It is also possible to construct a SWCNT from the reduced two-atom unit cell without making recourse to the translational symmetry: In Figure 2.7, the red ellipse at the end of the rotational vector $\mathbf{C}_h/d$ is obtained by applying the rotational vector $\mathbf{C}_h/d$ on the red ellipse at the origin. To generate the infinite SWCNT, we apply the helical vector on these two cells. This is the "angular-helical" representation. Mathematically, we adapt eq. (2.13) to:

$$\mathbf{X}_{n,(\zeta_1,\zeta_2)} = \mathbf{R}_2^{\zeta_2}\,\mathbf{R}_1^{\zeta_1}\mathbf{X}_n + \zeta_1\mathbf{T}_1, \tag{2.14}$$

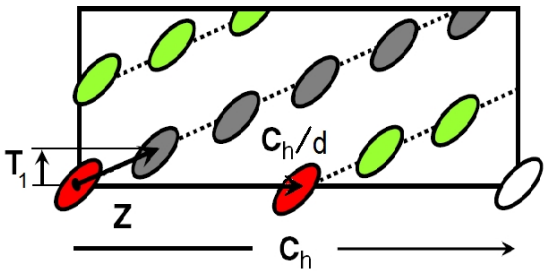

FIGURE 2.7: Construction of a $(4, 2)$ SWCNT in the "angular-helical" representation. Helical vector $\mathbf{Z}$ is applied an infinite amount of times to the two-atom domains depicted here with filled red ellipses. The ellipse at the middle of chiral vector is obtained by applying the rotational vector $\mathbf{C}_h/2$ on the red ellipse at the origin. The translational unit cell is not explicitly accounted.

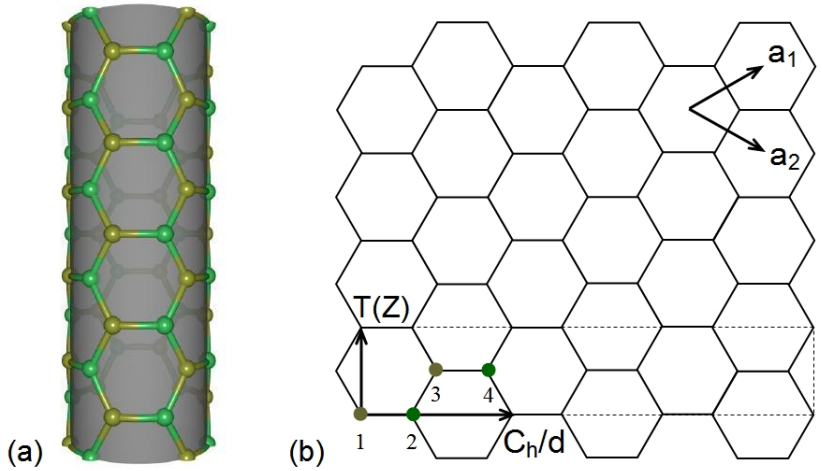

FIGURE 2.8: (a) a (3,3) SWCNT with 5 translational cells; (b) Construction of a (3,3) SWCNT by a four-atom domain labeled from 1 to 4. The arrows indicate the translational vector ($\mathbf{T}$), helical vector ($\mathbf{Z}$), and rotational vector ($\mathbf{C}_h/d$). Here $\mathbf{Z}$ coincides with $\mathbf{T}$.

where integer ζ_2 takes a finite number of values (sufficient to cover the circumference of the nanotube with no overlap) and $-\infty < \zeta_1 < \infty$. The translational vector $\mathbf{T}$ is not explicitly accounted for and all the axial translations are performed with the help of the screw operation. As before, $\mathbf{X}_n$ label the positions of the two atoms situated in the reduced unit cell, i.e., the red ellipse.

Both representations discussed above are equivalent. However, the "angular-helical" one is more general since it can be applied to describe situations where there is no translational symmetry, such as in arbitrarily twisted SWCNTs.

It is important to note that although both "angular-helical+translation" and "angular-helical" representations discussed above used a minimal "two-atom" reduce cell, it is also possible to describe the SWCNTs with these representations from somewhat larger domains. Of course, the parameters for the rotational and screw operators should be readjusted. For example, the (3,3) SWCNT shown in Figure 2.8 can be also generated from a four-atom domain: The rotational vector C_h/d with $d = 3$ is applied three times on this four-atom domain to generate the translational cell, boxed with dashed lines. Next, to generate the infinite SWCNT translational operations $\mathbf{T}$ are applied. Thus, eq. (2.13) becomes

$$\mathbf{X}_{n,(\zeta,\zeta_2)} = \mathbf{R}_2^{\zeta_2}\,\mathbf{X}_n + \zeta\mathbf{T}, \tag{2.15}$$

where index n runs over the four atoms of the employed "super-cell". Therefore, these two representations are general and can be extended to nanotubes and chiral nanowires by adjusting the input parameters, $\mathbf{T}$, $\mathbf{T_1}$, θ_1 and θ_2. Finally, other representations are possible, such as a "helical-helical" one (see Figure 1.1 from Chapter 1) but they will not be used here.

Chapter 3

Development of a Symmetry-Adapted Tight-Binding Molecular Dynamics Code

Tight-binding is a basic semi-empirical method which offers a satisfying description of the electronic structure and bonding of covalent systems in an intuitive localized picture. The tight-binding method of modelling materials lies between the very accurate, very expensive, *ab initio* methods and the fast but limited *empirical* methods. When compared with *ab initio* methods, tight-binding is typically two to three orders of magnitude faster, but suffers from a reduction in transferability due to the approximations made; when compared with *empirical* methods, tight-binding is two to three orders of magnitude slower, but the quantum mechanical nature of bonding is retained, ensuring that the angular nature of bonding is correctly described far from equilibrium structures. Tight-binding is therefore useful for the large number of situations in which quantum mechanical effects are significant, but the system size makes ab initio calculations impractical. More specifically, with relatively modest resources up to about 500 atoms can be comfortably treated with tight-binding.

Invoking the Born-Oppenheimer approximation, from the electronic structure one can extract a tight-binding potential that can be used to carry out tight-binding molecular dynamics simulations.

Most existing tight-binding implementations are designed for modeling a bulk infinite crystalline system. In this formulation, calculations are performed on atoms situated in one repeated translational unit cell, while the rules describing the repetition are strictly translations. The approach reduces the infinite-size problem to a finite number of atoms, typically within the tight-binding reach. For example, to obtain bulk properties for a graphitic layer, a minimal size unit cell containing only two atoms can be used. However, exploiting translational symmetry of chiral nano-objects does not bring the same degree of simplification. As illustrated in Chapter 2, translational unit-cells for most carbon nanotubes have computationally prohibitive sizes. In fact, due to this size limitation only low diameter/achiral symmetric nanotubes (with manageable sizes of the translational unit cells) have been simulated with quantum methods. On the other hand, smaller repeating cells can be identified if one takes advantage of the helical symmetry and augments the repetition rule to include translations and rotations. In this case, calculations would become as convenient as in the flat graphene.

Our objective is to create a symmetry-adapted tight-binding facility that explicitly accounts for helical symmetry and thus will significantly reduce the computational effort through a drastic reduction in the number of atoms to be accounted for.

This Chapter first describes the widely used formulation of tight-binding under periodic boundary condition. Next, it identifies the technical changes that need to be implemented in order to make possible performing simulations on the reduced domains under the new helical boundary condition. In the first part of this research, these changes will be implemented in the computational package *Trocadero* [40], which is well tested and growing in popularity in the simulation community. A brief description of this code is given.

3.1 Formulation of Tight-Binding Molecular Dynamics in a One-Dimensional Bravais Lattice

In tight-binding the electronic states of a periodic structure are obtained by solving the one-electron Schrödinger equation

$$[-\frac{\hbar^2}{2m}\bigtriangledown^2 + V(\mathbf{r})]|j\rangle = \epsilon_j|j\rangle, \tag{3.1}$$

where m is the electron mass, $\hbar$ the Plank's constant, $V(\mathbf{r})$ an effective periodic potential, and $|j\rangle$ and ϵ_j are the one-electron wavefunction and energy for the state j, respectively. This equation is solved with the ansatz that the single electron states can be represented in terms of atomic orbitals located on each single atom. The number of atomic orbitals n_α is usually taken equal with the number of valence electrons for the atomic species (for example $n_\alpha = 4$ for carbon and silicon). Let N_t (usually a large number) the number of translational cells over which periodic boundary condition are imposed and let N_0 be the number of atoms in each cell. If no explicit recourse to translational symmetry is made, the one-electron eigenfunctions $|j\rangle$ are represented in terms of localized orbitals functions $|\alpha n\rangle$, where α labels the orbital symmetry (s, p_x, p_y, p_z for our case) and n the atomic location:

$$|j\rangle = \sum_{\alpha,n} C_{\alpha n}(j)|\alpha n\rangle, \quad j = 1, ..., N. \tag{3.2}$$

The number of eigenstates $N = n_\alpha \cdot N_0 \cdot N_t$ equals the total number of valence electrons in the N_t translational cells considered. The expansion coefficients grouped in the vector $\mathbf{C}(j)$ should be obtained from the one-electron generalized $N \times N$ eigenvalue problem

$$\mathbf{H} \cdot \mathbf{C}(j) = \epsilon_j \mathbf{S} \cdot \mathbf{C}(j), \quad j = 1, ..., N, \tag{3.3}$$

which can be easily obtained by substituting equation (3.2) into (3.1). Equation (3.3) is known as the matrix form of the Schrödinger equation. In tight-binding, the matrix the elements of the Hamiltonian $\mathbf{H}$ matrix – e^0_α diagonal and $t^0_{\alpha',\alpha}$ off-diagonal – and of the overlap $\mathbf{S}$ matrix $s^0_{\alpha',\alpha}$ are not explicitly calculated. They are replaced with a parameter which depends only on the internuclear distance

and the symmetry of the orbitals involved. The parameterization is performed by using the available experimental data [43, 44] or by making recourse to more accurate but computationally expensive *first principles* [45, 46] calculations.

The total energy contained in the electronic states writes:

$$E_{band} = 2\sum_{j=1}^{N} f_j \epsilon_j, \tag{3.4}$$

where f is the Fermi distribution function.

3.1.1 Tight Binding under Periodic Boundary Condition – The Electronic Structure

Of course, in a crystalline structure with N on the order of 10^{23}, the $N \times N$ eigenvalue problem (3.3) cannot be solved directly. The usual approach is to introduce a significant computational simplification by explicitly accounting for the *translational* symmetry. For simplicity, we are next presenting this approach only for the one-dimensional crystal. (The expansion to the three-dimensional case is trivial.)

Let $\mathbf{T}$ be the lattice periodicity vector and $\{\mathbf{X}_n : n = 1, \ldots, N_0\}$ the atomic positions within the unit cell. The atomic locations in one-dimensional periodic structure can be obtained with

$$\mathbf{X}_{n,\zeta} = \zeta\mathbf{T} + \mathbf{X}_n, \tag{3.5}$$

where $\zeta = 0, \ldots, N_t - 1$, and $n = 1, \ldots, N_0$. To incorporate the translational symmetry, instead of eq. (3.2) the one-electron solutions are represented in terms of the Bloch sums:

$$|\alpha n, k\rangle = \frac{1}{\sqrt{N_t}} \sum_{\zeta} e^{ikT\zeta} |\alpha n, \zeta\rangle, \tag{3.6}$$

where the wavenumber k takes N_t uniformly spaced values in the interval $-\pi/T \leq k < \pi/T$, with $\delta k = 2\pi/TN_t$. $|\alpha n, \zeta\rangle$ represents the orbital α located on atom n located in the translational cell ζ, with $\zeta = 1, ..., N_t$. The advantage is that in the

representation (3.6), the tight-binding Hamiltonian and overlap matrix elements between two $\langle \alpha n', k'|$ and $|\alpha n, k\rangle$ sums are vanishing unless $k = k'$. Thus, the eigenvalue problem becomes block-diagonal and it can be solved separately for each N_t block labeled by k and having dimension $(N/N_t)\times(N/N_t)$:

$$\mathbf{H}(k) \cdot \mathbf{C}(j,k) = \epsilon_j(k)\mathbf{S}(k) \cdot \mathbf{C}(j,k), \quad j = 1, ..., N/N_t. \tag{3.7}$$

In other words, instead of solving the single $N \times N$ eigenvalue problem (3.3) to obtain the N electronic states, one solves instead N_t eigenvalue problems (3.7) of size $N/N_t \times N/N_t$ to obtain the same N electronic states, now labeled by j and k.

Formally, in the two-center approximation, the k-dependent elements of Hamiltonian $\mathbf{H}$ and overlap $\mathbf{S}$ matrices write:

$$\langle \alpha' n', k|H|\alpha n, k\rangle = \sum_{\zeta} e^{-ikT\zeta} t^0_{\alpha'\alpha}(\mathbf{X}_{n',\zeta} - \mathbf{X}_n), \tag{3.8}$$

$$\langle \alpha' n', k|\alpha n, k\rangle = \sum_{\zeta} e^{-ikT\zeta} s^0_{\alpha',\alpha}(\mathbf{X}_{n'\zeta} - \mathbf{X}_n). \tag{3.9}$$

As before, $\mathbf{X}_n$ represent the atomic coordinates in the initial $\zeta = 0$ cell.

3.1.1.1 Illustrative Example: Tight-Binding π Electronic Bands in Polyacetylene

We now illustrate how a simple tight-binding model in the translational formulation can be used to describe the electronic states in polyacetylene, shown schematically in Figure 3.1. As one-dimensional zigzag chain with an angle of 120°, polyacetylene has two sp^2-hybridized carbon atoms and two hydrogen atoms in the translational unit cell. We would like to describe only the π bonding between localized p_z orbitals. The hydrogen atoms have no π electrons and each carbon atom has single π electron. Thus, for the π band problem, $N_0 = 2$. With one $\alpha = p_z$ orbital for each carbon atom, the k-dependent Hamiltonian and overlap matrices are small 2×2 matrices. We label the C-C bond length as a. The translational vector $\mathbf{T}$ is of a length of $\sqrt{3}a$, and the wavevector k varies within the interval

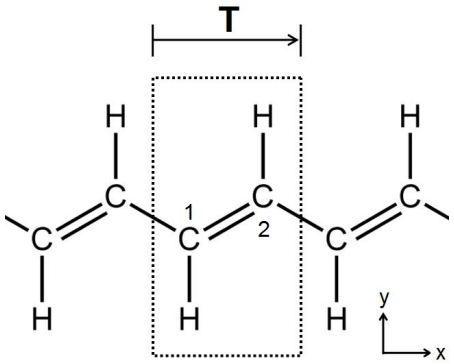

FIGURE 3.1: A segment polyacetylene as a periodic structure. The translational unit cell is bounded by a box defined by the dotted lines. Beyond the box, the arrow shows the translational vector **T**. The two non-equivalent carbon atoms are labeled by 1 and 2, respectively.

$-\pi/T \leq k < \pi/T$. Within the nearest-neighbor approximation, the k-dependent Hamiltonian and overlap matrices are

$$\mathbf{H} = \begin{bmatrix} \epsilon^0_{p_z} & (1+e^{ikT})t^0_{p_zp_z} \\ (1+e^{-ikT})t^0_{p_zp_z} & \epsilon^0_{p_z} \end{bmatrix},$$

$$\mathbf{S} = \begin{bmatrix} 1 & (1+e^{ikT})s^0_{p_z} \\ (1+e^{-ikT})s^0_{p_z} & 1 \end{bmatrix}.$$

The secular equation writes:

$$\begin{vmatrix} \epsilon^0_{p_z} - E(k) & (1+e^{ikT})(t^0_{p_zp_z} - E(k)s^0_{p_z}) \\ (1+e^{-ikT})(t^0_{p_zp_z} - E(k)s^0_{p_z}) & \epsilon^0_{p_z} - E(k) \end{vmatrix} = 0 \qquad (3.10)$$

The eigenvalues $E(k)$ are obtained in term of $\epsilon^0_{p_z}$, $t^0_{p_zp_z}$ and $s^0_{p_zp_z}$, viewed as parameters:

$$E_\pm(k) = \frac{\epsilon^0 \pm 2t^0\cos(k\sqrt{3}a/2)}{1 \pm 2s^0\cos(k\sqrt{3}a/2)}. \qquad (3.11)$$

As a visualization, Figure 3.2 shows the obtained π bands as functions of wavevector k. E_+, the lower valence band is called bonding while the E_- is called the antibonding energy band. When periodic boundary condition is imposed over a finite number of cells ($N_t = 20$ in Figure 3.2(a)), the wavevector k is discrete and the interval between the allowed values is $\Delta k = 2\pi T/N_t$. As $N_t \to \infty$, $\Delta k \to 0$ and the energy bands become continuous, as shown in Figure 3.2(b).

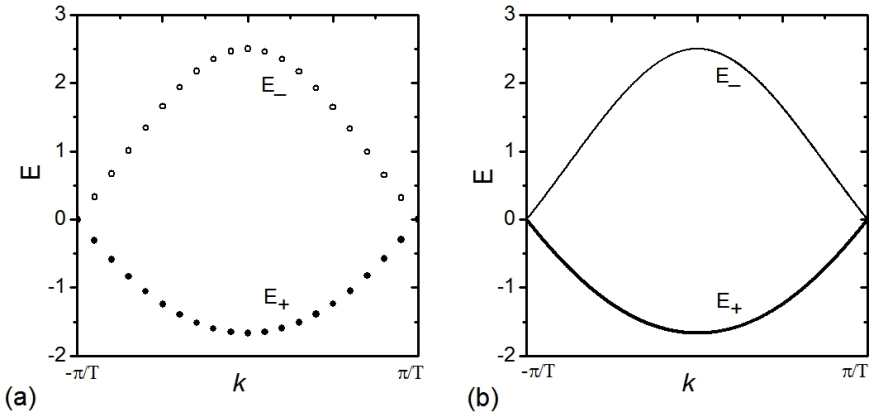

FIGURE 3.2: The energy dispersion relation $E_{\pm}$ as functions of wavevector k given by eq.(3.11) letting $t^0_{p_z p_z} = -1$, $s^0_{p_z} = 0.2$ and $\epsilon^0_{p_z} = 0$: (a) the energy was computed at each discrete k where $N_t = 20$; (b) The electronic energy becomes continuous with k when $N_t \to \infty$.

3.1.2 Tight-Binding Molecular Dynamics under Periodic Boundary Condition

In the translational formulation, the total energy contained in the electronic states writes:

$$E_{band} = 2 \sum_{j=1}^{N/N_t} \sum_{k=-\delta k(N_t-1)/2}^{\delta k(N_t-1)/2} f_j(k) E_j(k), \tag{3.12}$$

and depends parametrically on the coordinates of the nuclei. In the framework of the Born-Oppenheimer approximation [47], once the electronic energy is found, it can be directly used to give the motion of the nuclei, which are treated classically. More precisely, to perform molecular dynamics, the forces acting on the N_0 atoms located in the initial cell, are needed. In tight-binding molecular dynamics, the force due to the band energy on the atom at $\mathbf{X}_m$ located in the initial cell due to the band energy, $\mathbf{F}_m = -\partial E_{band}/\partial \mathbf{X}_m$, writes:

$$\mathbf{F}_m = -2 \sum_{j,k} f_j(k) \left(\mathbf{C}^{\dagger}(j,k) \cdot \frac{\partial \mathbf{H}(k)}{\partial \mathbf{X}_m} \cdot \mathbf{C}(j,k) - \varepsilon_j(k) \mathbf{C}^{\dagger}(j,k) \cdot \frac{\partial \mathbf{S}(k)}{\partial \mathbf{X}_m} \cdot \mathbf{C}(j,k) \right), \tag{3.13}$$

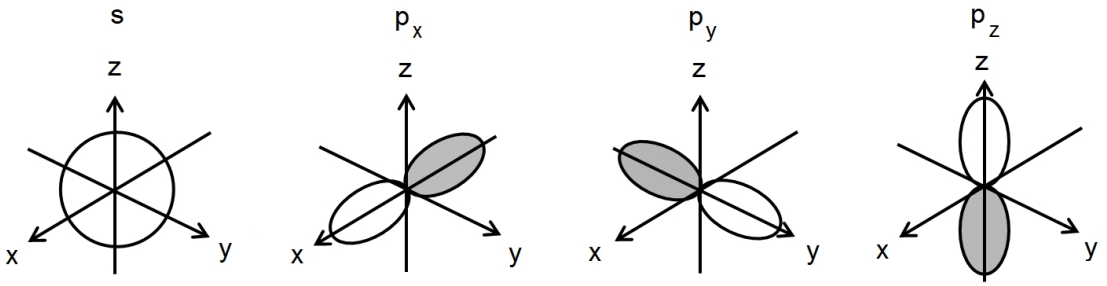

FIGURE 3.3: A schematic of the localized valence orbitals s, p_x, p_y, and p_z atomic orbitals of the carbon atom. The white shaded area corresponds to the positive sign of the wavefunction amplitude while the gray shaded area indicates the negative wavefunction amplitude.

which is the Hellmann-Feynman force. Typical derivatives of the TB Hamiltonian and overlap matrix elements are:

$$\frac{\partial\langle\alpha' n', \kappa|H|\alpha m, \kappa\rangle}{\partial \mathbf{X}_m} = \frac{1}{N_t}\sum_{\zeta} e^{-i\kappa\zeta}\frac{\partial t^0_{\alpha',\alpha}(\mathbf{X}_{n',(\zeta)} - \mathbf{X}_m)}{\partial \mathbf{X}_m}. \tag{3.14}$$

$$\frac{\partial\langle\alpha' n', k|\alpha m, k\rangle}{\partial \mathbf{X}_m} = \frac{1}{N_t}\sum_{\zeta} e^{-ik\zeta}\frac{\partial s^0_{\alpha',\alpha}(\mathbf{X}_{n',(\zeta)} - \mathbf{X}_m)}{\partial \mathbf{X}_m}. \tag{3.15}$$

In tight-binding one assumes a form for the Hamiltonian and overlap matrix elements without specifying anything about the atomic orbitals except their symmetry. The values of the matrix elements may be derived approximately or may be fitted to experiment or other theory.

3.1.3 Harrison's Two-Centre Tight-Binding Model

Among the various models, a simple orthogonal (i.e., $\mathbf{S}$=0) tight-binding model was proposed by Harrison [48] in which the hopping element $t^0_{\alpha',\alpha}$ scales as d^{-2}, where d is the interatomic distance. For *sp* system, such as C and Si, the localized atomic orbitals are shown in Figure 3.3. In this convenient approximation, the

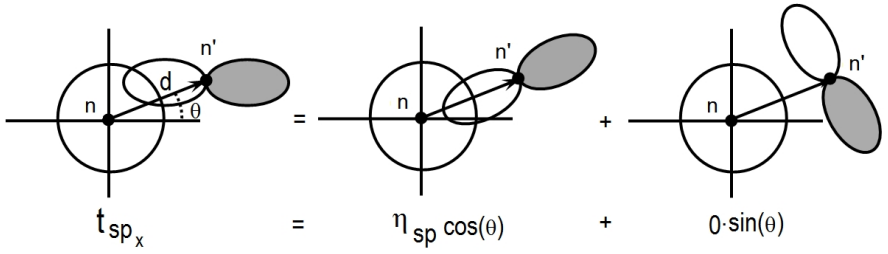

FIGURE 3.4: Schematic representation of off-orthogonal matrix element $t_{sn,p_x n'}$. The σ and π interactions respectively involve orbitals oriented parallel and perpendicular to a joining vector $\mathbf{d}$ from site n to n'. The π interaction vanishes because p and s orbitals have odd and even parity, respectively.

hopping Hamiltonian matrix elements are given by [48]:

$$\begin{cases} t_{sn,sn'} = & \eta_{ss}\dfrac{\hbar^2}{m_e}\dfrac{1}{d^2}, \\ t_{sn,p_\mu n'} = & l_\mu \eta_{sp}\dfrac{\hbar^2}{m_e}\dfrac{1}{d^2} = -t_{p_\mu n,sn'}, \\ t_{p_\mu n,p_v n'} = & [l_v l_\eta(\eta_{pp}-\eta'_{pp})+\delta_{v\eta}\eta'_{pp}]\dfrac{\hbar^2}{m_e}\dfrac{1}{d^2} = t_{p_v n,p_\mu n'}. \end{cases} \tag{3.16}$$

Here μ and v denote the cartesian index, i.e., x, y or z. $l_v = d_v/d$ and $l_\mu = d_\mu/d$ are the direction cosine between sites n and n' separated by distance d. η_{pp} and η'_{pp} correspond to the σ and π bonds, respectively. m_e is the electron mass and the quantity $\hbar/m_e$ is approximately 7.62 eV/$\mathring{A}^2$. As an example, Figure 3.4 shows how the matrix element $t_{sn,p_x n'}$ is evaluated. The η's are parameters which characterize the amount of overlap between orbitals of particular symmetries. They are responsible therefore for the strength of the chemical bonds. They are empirically adjusted to correctly reproduce electronic properties such as the band gap. A widely used set of parameters was given by Vogl et al [49]. Because of the explicit distance dependence, the Hellmann-Feynman forces can be computed analytically and molecular dynamics can be performed. The ability of a potential to work properly in different environments is called transferability. Although the model offers an excellent description of the bulk configuration for which it was fitted (in some sense better than *ab initio* methods) it is less transferable to other configurations such as when modeling surfaces.

3.1.4 Two-Centre Density-Functional-Based Tight-Binding Model

First-principles calculations can be used to generate data for the tight-binding parametrizations. One possible approach consists of using first-principles calculations with an atomic-like basis set to obtain band structures that can then be used as input data to fit the Hamiltonian and overlap matrix elements. This has been done by Porezag et al [45], that constructed a model known as density functional tight-binding (DFTB). In their approach the tight-binding energy is written as a sum of a band-structure term and a pair-repulsion term. Slater-type orbitals and spherical harmonics $Y_{l_j m_j}$ are used to construct an atomic basis:

$$|\alpha\rangle = \sum_{n,\beta,l_\alpha,m_{alpha}} a_{n\beta} r^{l_j+n} e^{-\beta r} Y_{l_\alpha m_\alpha}\left(\frac{\mathbf{r}}{r}\right). \tag{3.17}$$

Using this ansatz, a modified Kohn-Sham equation was solved self-consistently:

$$[-\frac{\hbar^2}{2m} \bigtriangledown^2 + V^{ps-at}(\mathbf{r})]|\alpha\rangle = \epsilon_\alpha^{psat}|\alpha\rangle, \tag{3.18}$$

where V^{ps-at} is the one-electron effective pseudo-atom potential

$$V^{ps-at}(\mathbf{r}) = V_{nucleus}(\mathbf{r}) + V_{Hartree}[n(\mathbf{r})] + V_{xc}^{LDA}[n(\mathbf{r})] + \left(\frac{\mathbf{r}}{r_0}\right)^N, \tag{3.19}$$

consisting of ionic potential $V_{nucleus}$, repulsion potential of all the other electrons $V_{Hartree}$ and exchange-correlation potential in LDA approximation V_{xc}^{LDA}. $n(\mathbf{r})$ is the charge density at $\mathbf{r}$. The additional term $(\mathbf{r}/r_0)^N$ is used to avoid the wavefunction extending far away and results in a compressed electron density. Porezag et al. [45] indicated that good choices for these parameters are $N = 2$ and $r_0 = 2r_{cov}$, where r_{cov} is the covalent radius of the element in question.

Once the $|\alpha\rangle$ have been obtained, it was used as the localized basis function of the system and the tight-binding parametrization was carried out. The overlap matrix elements are tabulated as a function of the internuclear distance directly. In order to obtain the Hamiltonian matrix elements, an effective potential V_{eff} is

constructed for each structure from atomic contributions:

$$V_{eff}(\mathbf{r}) = \sum_n V_0^n(\mathbf{r} - \mathbf{R}_n), \tag{3.20}$$

where $\mathbf{R}_n$ is the atomic position vector and V_0 is the Kohn-Sham potential due to this atom, i.e. (3.19) but without the term $(\mathbf{r}/r_0)^N$. Using this potential, the Hamiltonian matrix elements are tabulated from:

$$H_{\alpha\alpha'} = \begin{cases} \epsilon_\alpha^{freeatom} & \alpha = \alpha' \\ \langle \alpha'_{n'} | [-\frac{\hbar^2}{2m} \bigtriangledown^2 + V_o^n + V_o^{n'}] | \alpha_n \rangle & n \neq n' \\ 0 & otherwise \end{cases} \tag{3.21}$$

where, n and n' label different atoms on which the atomic functions and the Kohn-Sham potentials are centered. As can be seen, only two-center Hamiltonian matrix elements are treated. Note that the correct energy limit of isolated atom is guaranteed since the eigenvalue of free atom, $\epsilon_j^{free\ atom}$ is used as the diagonal matrix elements.

The DFTB total energy consists of both the electronic band energy and a short-range repulsive two-body potential E_{rep}:

$$\begin{aligned} E_{tot} &= E_{band} + E_{rep} \\ &= \sum_i f_i \epsilon_i + \sum_n \sum_{n'>n} V_{rep}(|\mathbf{R}_{n'} - \mathbf{R}_n|). \end{aligned} \tag{3.22}$$

E_{rep} models the ion-ion repulsion and the electron-electron interaction which is double counted in the sum over electronic eigen-states. Here f_i is the occupation number of orbital i. The repulsive potential is usually fitted to results for diatomic molecules, though in some cases this could lead to difficulties arising from level-crossings, in which case it is possible to fit using results from other structures.

The DFTB approach has been successfully applied to various problems in different systems and materials, covering carbon [45], silicon [54], germanium structures [55], boron [56], carbon nitrides [57], silicon carbide [58], oxide [52], and GaAs surfaces [59].

TABLE 3.1: Comparison of Young's modulus (TPa) of SWCNTs obtained with the DFTB model, the classical Tersoff-Brenner model, experiment, and DFT calculations.

SWCNT	DFTB [50]	Tersoff-Brenner [51]	Experiment [52]	DFT [53]
$(10, 0)$	1.22	-	-	-
$(10, 10)$	1.24	0.69	1.25	1.20

Perhaps the most transferable and widely used DFTB parameterizations are for carbon materials [45]. Indeed, the model was proved extremely useful in modeling the amazing variety of structures found, including graphite, diamond, buckyballs [60], nanoclusters, and nanotubes. The fact that it compares in accuracy with density functional theory modeling of molecules, clusters and bulk phases, it demonstrates that, in spite of its simple nature, this method produces parametrizations with good transferability properties. In comparison with the widely used empirical models, significantly improved results have been reported. For example, in Table 3.1, the Young's modulus of zigzag $(10, 0)$ and armchair $(10, 10)$ carbon nanotubes are summarized, as obtained with various theoretical and experimental approaches. In experiment, the Young's modulus is measured by thermally inducing vibration in cantilevered SWCNTs. Comparing with the average value of 1.25 TPa measured in experiment [52] and the average 1.20 TPa of DFT [53], we see that the classical Tersoff-Brenner potential [51] severely underestimates the Young's modulus. The DFTB model [50] is in agreement with both the experiment and DFT calculations.

The parameterization for silicon [54] shows again significant advantages over the existing classical potential descriptions. Consider for instance the surface reconstruction of the (001) surface of silicon shown in Figure 3.5(a). With the most popular classical potentials, Stillinger-Weber [61] and Tersoff [62], the $p(2\times1)$ symmetric dimer pattern shown in Figure 3.5(b), was found to be the most stable [63] with energetic benefit of $\sim$ 2 eV/dimer over the unreconstructed surface shown in Figure 3.5(a). However, with density-functional theory it was found that the asymmetric buckling of the dimers in a $p(2\times1)$ asymmetric pattern (Figure 3.5(c)) lowers the energy significantly, by $\sim$ 150 meV/dimer. A further $\sim$ 80 meV/dimer

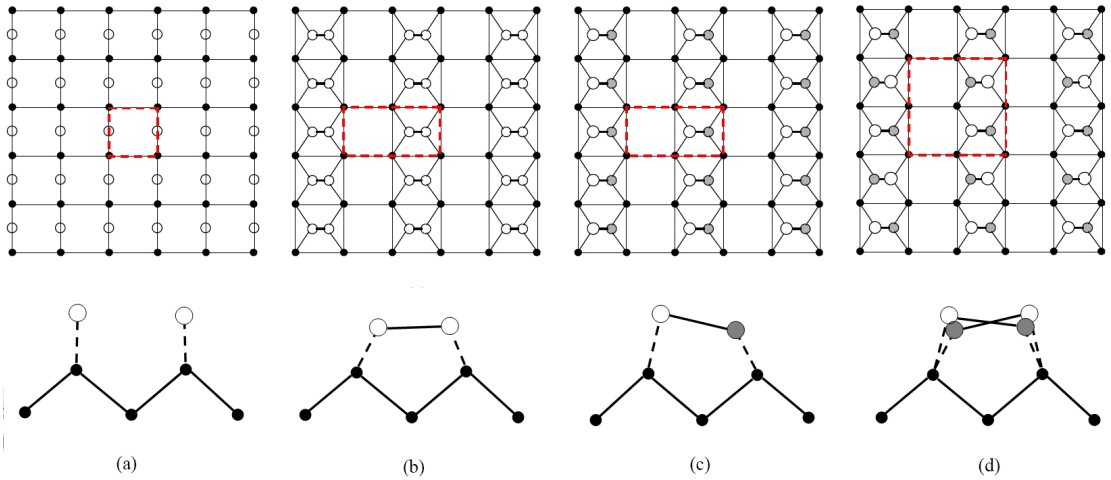

FIGURE 3.5: Top view and side view of different patterns of surface reconstruction of silicon (001) surface. Large white circles and grey circles represent the atoms in the surface layer while the small dark circles represent the atom in the second layer. The non-reconstructed surface (a), the (2×1) symmetric reconstruction (b), the $p(2 \times 1)$ asymmetric buckling reconstruction (c), the $p(2 \times 2)$ alternating asymmetric buckling reconstruction (d). The red dashed boxes define the surface translational unit cell for each reconstruction pattern.

energy lowering was obtained in a $p(2 \times 2)$ reconstruction with alternating asymmetric buckling of surface dimers (Figure 3.5(d)). Remarkably, both asymmetric $p(2 \times 1)$ and alternating asymmetric $p(2 \times 2)$ patterns could be described with DFTB [54].

DFTB parameterizations exist not only for monoelemental but also for multielemental systems, where the chemical bonding is more complex. Consider the case of boron nitride [64], where the model must account for the partially ionic character in addition to the covalent bonding. This parameterization is successfully describing the linear properties of boron nitride nanotubes, which has the largest elastic modulus among the insulator nanomaterials. The Young's modulus of exemplified BNNTs obtained by different methods are listed in Table 3.2 where the experiment data [65] were obtained via the same way as the measurement of CNTs in the above. All the theoretical models lead to positive deviation from the average of 0.722 TPa of experiment. The Tersoff-Brenner models [66] even overestimates the Young's modulus by about 50%. Both DFTB [50] and *ab initio* [67] models give good values around 0.85 TPa,in good agreement with experiments.

TABLE 3.2: Comparison of Young's modulus (in unit of TPa) of BNNTs obtained by DFTB model, Tersoff-Brenner model, *ab initio* model and experiment.

(n, m):	DFTB [50]	Tersoff-Brenner [66]	*ab initio* [67]	Experiment [65]
$(10, 0)$	0.837	-	-	
$(12, 0)$	-	1.078	0.850	0.722
$(10, 10)$	0.901	1.064	-	

The above examples show that DFTB model offers a significant advantage over empirical treatment while avoids the high DFT computational costs. Because of the the high transferability and the large database of available parameterizations (see www.dftb.org), the DFTB approach is becoming increasingly popular in modeling low dimensional structures. In fact, DFTB has already been applied to many different nanomaterials, such as hydrogen passivated carbon [68] and silicon systems [69] and other multi-component systems including WS_2 and MoS_2 nanotubes [70]. DFTB model was also applied to the metal systems such as gold nanowires [71] and copper clusters [72] for both elastic and electronic properties.

Because the DFTB approach is becoming increasingly popular in modeling low dimensional structures with the high transferability and the variety of available parameterizations, we have selected this microscopic model to couple it to the symmetry-adapted tight-binding molecular dynamics.

3.2 Detailed Formulation of the Proposed Symmetry-Adapted Tight-Binding Molecular Dynamics

A major disadvantage of DFTB is still its high computational cost: Computing the electronic structure energy and forces from a TB Hamiltonian by direct diagonalization results in a cubic scaling of the computational time with the number of electrons considered $[O(N^3)]$. This limits the system size to about 1000 Si or C atoms. In a Bravais lattice, the number of atoms is small. Thus, the above

approach is suitable in simulations of bulk crystals. However, the simplifications due to the periodic boundary condition are insufficient for comprehensive calculations of quasi one-dimensional objects such as nanowires and nanotubes. This is because the number of atoms in the translational unit cells can be very large, leading to a large-size matrix equation for the electronic problem. Note that there is a current research line that attempts to alleviate this notorious dependence of computation time with $O(N)$ methods [73]. However, the errors introduced [74] in the electronic band structure could affect the outcome.

As described in Chapter 2, chiral nanostructures can be described more economically using two representations – "angular-helical+translation" and "angular-helical"– which are equivalent as long as there is translational symmetry. Obviously, the "angular-helical+translation" is invalid if the nanostructure does not posses translational symmetry (such as arbitrarily twisted structures).

The "angular-helical" representation, on the other hand, is always valid, as it requires the helical and rotational symmetries. For a higher flexibility, both representations will be implemented. The "angular-helical+translation" representation is particularly useful for band structure calculations, as the linear wavenumber k shows up in the formulation. An example showing the utility of this representation in computing the band structure of a (3,3) SWCNT is given in subsection 3.2.2.1. We now discuss the tight-binding implementation of the more general "angular-helical" representation.

3.2.1 Symmetry-Adapted Tight-Binding Molecular Dynamics in the "Angular-Helical" Representation

As discussed in Chapter 2, in the "angular-helical" representation, a chiral structure can be described with

$$\mathbf{X}_{n,(\zeta_1,\zeta_2)} = \mathbf{R}_2^{\zeta_2}\,\mathbf{R}_1^{\zeta_1}\mathbf{X}_n + \zeta_1\mathbf{T}_1, \tag{3.23}$$

where index n runs over the N_0 atoms at locations $\mathbf{X}_n$ inside the repeating symmetry-adapted domain (only two-atoms for carbon nanotubes), while integers

ζ_1 and ζ_2 label various replicas of the domain. Rotational matrix $\mathbf{R}_1$ of angle θ_1 and the axial vector $\mathbf{T}_1$ indicate a screw transformation applied to the symmetry-adapted domain while the rotational matrix $\mathbf{R}_2$ indicates an axial rotation of angle θ_2.

We will accommodate this representation into the one-electron wavefunction solutions by representing them in terms of symmetry-adapted sums [35–37, 75–77] of localized orbitals, suitable for the helical and angular symmetry. We discuss next the steps that will be undertaken to enhance to symmetry-adapted modeling the current periodic boundary condition implementation in the computational package *Trocadero* [40]. We remind the reader that the microscopic model of interest is the nonorthogonal density functional theory-based tight binding model with two-center terms of Porezag et al. [54].

3.2.2 Symmetry-Adapted Tight Binding – Treatment of The Electronic Structure

Consider N_s the number of screw operations (typically ∞) over which the helical boundary condition is imposed and let N_a be the number of θ_2 rotations needed to fill the circumference of the quasi one-dimensional nanostructure. The symmetry-adapted Bloch sums write

$$|\alpha n, l\kappa\rangle = \frac{1}{\sqrt{N_a \cdot N_s}} \sum_{\zeta_1=0}^{N_s-1} \sum_{\zeta_2=0}^{N_a-1} e^{il\theta_2\zeta_2 + i\kappa\zeta_1} |\alpha n, \zeta_1\zeta_2\rangle, \tag{3.24}$$

where the phase factors [78] are the eigenvalues of the commuting rotation and screw operators [36]. Here $l = 0, 1, ..., (N_a - 1)$ represents the angular number. To avoid the discomfort of introducing helical distances, $-\pi \leq \kappa < \pi$ represents the helical wavevector already normalized by the helical periodicity. As in eq. (3.23), index n runs over the atoms located in the symmetry-adapted computational cell and $|\alpha n, \zeta_1\zeta_2\rangle$ refers to the orbital with symmetry α located on atom n, all in the symmetry-adapted cell indexed by ζ_1 and ζ_2. Lastly, to satisfy the generalized Bloch theorem, the $|\alpha n, \zeta_1\zeta_2\rangle$ orbitals are obtained by applying a $\mathbf{R}^{(\zeta_1,\zeta_2)}$ rotation to the orbitals $|\alpha n\rangle$ located in the (ζ_1, ζ_2) cell that are parallel with those situated

in the initial $(0,0)$ cell . Specifically, for our *sp* case:

$$\begin{pmatrix} |sn,\zeta_1\zeta_2\rangle \\ |p_x n,\zeta_1\zeta_2\rangle \\ |p_y n,\zeta_1\zeta_2\rangle \\ |p_z n,\zeta_1\zeta_2\rangle \end{pmatrix} = \begin{pmatrix} 1 & 0 & 0 & 0 \\ 0 & \cos(\zeta_1\theta_1+\zeta_2\theta_2) & -\sin(\zeta_1\theta_1+\zeta_2\theta_2) & 0 \\ 0 & \sin(\zeta_1\theta_1+\zeta_2\theta_2) & \cos(\zeta_1\theta_1+\zeta_2\theta_2) & 0 \\ 0 & 0 & 0 & 1 \end{pmatrix} \cdot \begin{pmatrix} |sn\rangle \\ |p_x n\rangle \\ |p_y n\rangle \\ |p_z n\rangle \end{pmatrix}. \tag{3.25}$$

Note that the s orbitals are not affected because of their intrinsic symmetry while the p_z ones are invariant as they are oriented along the NW axis.

The symmetry-adapted Bloch elements between different angular and helical numbers of the Hamiltonian and overlap matrices vanish. Therefore, the eigenvalue problem for the atoms contained in the $N_s \cdot N_a$ symmetry-adapted domains becomes block-diagonal and it can be solved separately for each block labeled by l and κ:

$$\mathbf{H}(l\kappa)\cdot\mathbf{C}(j,l\kappa) = \varepsilon_j(l\kappa)\mathbf{S}(l\kappa)\cdot\mathbf{C}(j,l\kappa), \quad j=1,...,N. \tag{3.26}$$

The elements of eigenvector $\mathbf{C}$ represent the expansion coefficients in the basis (3.24) of the one-electron wavefunction solutions of the Schrödinger equation. Having [54] the elements of the Hamiltonian matrix – ϵ^0_α diagonal and $t^0_{\alpha',\alpha}$ off-diagonal – and of the overlap matrix $s^0_{\alpha',\alpha}$, the elements of $l\kappa$-dependent Hamiltonian $\mathbf{H}$ and overlap $\mathbf{S}$ matrices are:

$$\langle\alpha' n',l\kappa|H|\alpha n,l\kappa\rangle = \epsilon^0_\alpha\delta_{nn'}\delta_{\alpha\alpha'} + \sum_{\zeta_2,\zeta_1} e^{-il\theta_2\zeta_2 - i\kappa\zeta_1} t_{\alpha'\alpha}(\mathbf{X}_{n',(\zeta_1,\zeta_2)} - \mathbf{X}_n), \tag{3.27}$$

$$\langle\alpha' n',l\kappa|\alpha n,l\kappa\rangle = \delta_{nn'}\delta_{\alpha\alpha'} + \sum_{\zeta_2,\zeta_1} e^{-il\theta_2\zeta_2 - i\kappa\zeta_1} s_{\alpha',\alpha}(\mathbf{X}_{n',(\zeta_1,\zeta_2)} - \mathbf{X}_n), \tag{3.28}$$

where

$$t_{\alpha'\alpha}(\mathbf{X}_{n',(\zeta_1,\zeta_2)} - \mathbf{X}_n) = \sum_{\alpha''=1}^{n_\alpha} t^0_{\alpha'',\alpha}(\mathbf{X}_{n',(\zeta_1,\zeta_2)} - \mathbf{X}_n) R^{(\zeta_1,\zeta_2)}_{\alpha',\alpha''}, \tag{3.29}$$

$$s_{\alpha',\alpha}(\mathbf{X}_{n',(\zeta_1,\zeta_2)} - \mathbf{X}_n) = \sum_{\alpha''=1}^{n_\alpha} s^0_{\alpha'',\alpha}(\mathbf{X}_{n',(\zeta_1,\zeta_2)} - \mathbf{X}_n) R^{(\zeta_1,\zeta_2)}_{\alpha',\alpha''}. \tag{3.30}$$

In comparison with the tight-binding under periodic boundary conditions [33], in

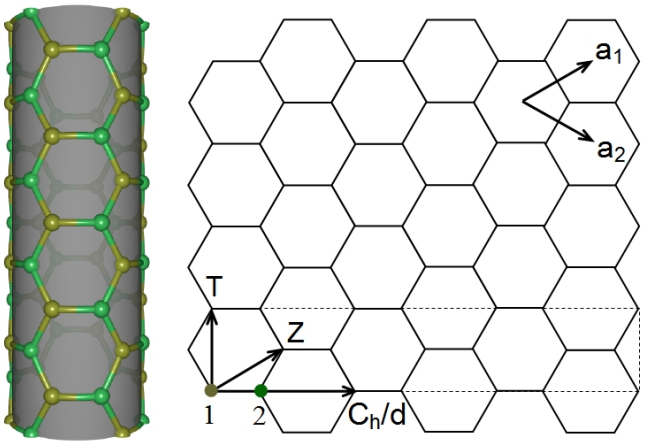

FIGURE 3.6: A (3, 3) single walled carbon nanotube (left panel) projected on a graphene sheet (right panel). On the graphene sheet, the arrows show the translational vector $\mathbf{T}$, rotational vector $\mathbf{C}_h/d$ and helical vector $\mathbf{Z}$. The translational cell is bounded by a box defined by dash lines. $\mathbf{a_1}$ and $\mathbf{a_2}$ are the basis vectors. The solid 1 and 2 dots, colored by yellow and green, respectively, indicate the two sublattices.

eq. (3.26) we obtained a size reduction of the eigenvalue problem at the expense of carrying out diagonalizations at additional $l\kappa$ points. In view of the $O(N^3)$ computational time scaling, the advantage of the symmetry-adapted basis is evident.

3.2.2.1 Illustrative Example: Band Structure of Carbon Nanotubes

We now illustrate the above ideas to describe the band structure for the simple case of the (3,3) carbon nanotube shown in Figure 3.6. In the unfolded picture, the parameters of the (3, 3) carbon nanotube are: translational vector $\mathbf{T} = \mathbf{a}_1 - \mathbf{a}_2$, circumference vector $\mathbf{C}_h/d = \mathbf{a}_1 + \mathbf{a}_2$, and the screw vector $\mathbf{Z} = \mathbf{a}_1$. If we label C-C bond length with a, the length of translational vector $\mathbf{T}$ is $T = \sqrt{3}a$. The two atoms, labeled by 1 and 2 represent the domain needed to describe the nanotube structure in either representation. The translational cell bounded by the translational vector $\mathbf{T}$ and circumference vector $\mathbf{C}_h$ contains 12 atoms.

We would like to now illustrate that the symmetry-adapted approach gives a periodic boundary condition equivalent answer to the electronic band structure problem. For the convenience of direct comparison with periodic boundary conditions,

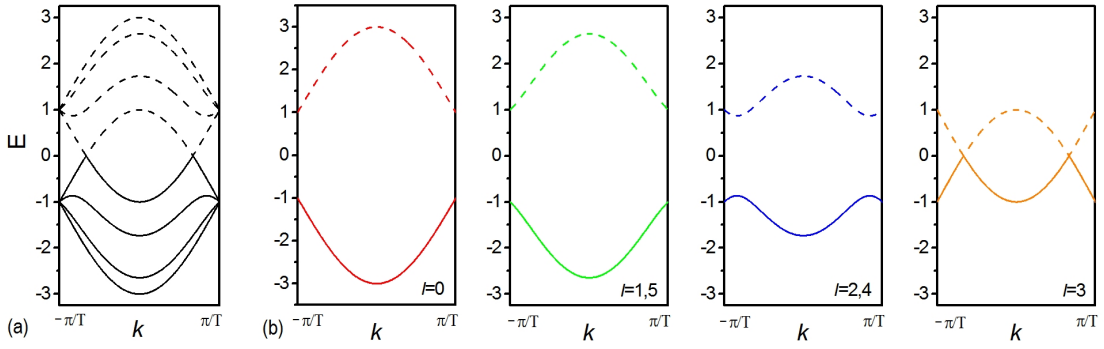

FIGURE 3.7: Analytical energy bands for π bonding in a (3, 3) armchair SWCNT as obtained in (a) translational and (b) symmetry-adapted tight-binding. The symmetry-adapted domain contains 2 atoms with single localized π (p_z) orbital on each atom while the translational cell contains 12 atoms. Valence (conduction) bands are represented with continuous (dashed) lines.

we will show this equivalence in the symmetry-adapted tight-binding basis corresponding to the "angular-helical+translation" formulation. This is because the translational vector is explicitly accounted and the linear wavevector k still stands. In this representation the Bloch sum writes [36]

$$|\alpha n, lk\rangle = \frac{1}{\sqrt{N_a \cdot N_s}} \sum_{\zeta_1=0}^{N_s-1} \sum_{\zeta_2=0}^{N_a-1} e^{il(\theta_2\zeta_2+\theta_1\zeta_1)+ik\zeta_1} |\alpha n, \zeta_1\zeta_2\rangle. \tag{3.31}$$

In comparison with formula (3.24) κ is replaced by the linear wavevector k. Here $l = 0, 1, ..., (N_a - 1)$ represents the angular number. For the (3, 3) SWCNT, N_a=6, θ_1=60°, T_1=$T/2$ and θ_2=120° The elements of Hamiltonian and overlap matrices are:

$$\langle \alpha' n', lk|H|\alpha n, lk\rangle = \epsilon^0_\alpha \delta_{nn'}\delta_{\alpha\alpha'} + \sum_{\zeta_2,\zeta_1} e^{-il(\theta_2\zeta_2+\theta_1\zeta_1)-ik\zeta_1} t_{\alpha'\alpha}(\mathbf{X}_{n',(\zeta_1,\zeta_2)} - \mathbf{X}_n), \tag{3.32}$$

$$\langle \alpha' n', lk|\alpha n, lk\rangle = \delta_{nn'}\delta_{\alpha\alpha'} + \sum_{\zeta_2,\zeta_1} e^{-il(\theta_2\zeta_2+\theta_1\zeta_1)-ik\zeta_1} s_{\alpha',\alpha}(\mathbf{X}_{n',(\zeta_1,\zeta_2)} - \mathbf{X}_n). \tag{3.33}$$

Considering the one p_z orbital on each carbon atom, two Bloch sums are built to construct the 2×2 Hamiltonian and overlap matrices. The elements of Hamiltonian

and overlap matrices are:

$$\mathbf{H} = \begin{bmatrix} \epsilon^0 & t^0(1+e^{il\theta-ik\frac{T}{2}}+e^{il\theta+ik\frac{T}{2}}) \\ t^0(1+e^{-il\theta+ik\frac{T}{2}}+e^{-il\theta-ik\frac{T}{2}}) & \epsilon^0 \end{bmatrix},$$

$$\mathbf{S} = \begin{bmatrix} 1 & s^0(1+e^{il\theta-ik\frac{T}{2}}+e^{il\theta+ik\frac{T}{2}}) \\ s^0(1+e^{-il\theta+ik\frac{T}{2}}+e^{-il\theta-ik\frac{T}{2}}) & 1 \end{bmatrix}.$$

With these two matrices, the secular equation is written in a full matrix form as:

$$\begin{vmatrix} \epsilon^0 - E & (1+e^{il\theta-ik\frac{T}{2}}+e^{il\theta+ik\frac{T}{2}})(t^0-s^0E) \\ (1+e^{-il\theta+ik\frac{T}{2}}+e^{-il\theta-ik\frac{T}{2}})(t^0-s^0E) & \epsilon^0 - E \end{vmatrix} = 0.$$

The eigenvalue E is then solved as:

$$E(lk) = \frac{\epsilon^0 \pm t^0\sqrt{3+4\cos\frac{kT}{2}+2\cos\frac{l\pi}{3}}}{1 \pm s^0\sqrt{3+4\cos\frac{kT}{2}+2\cos\frac{l\pi}{3}}}. \tag{3.34}$$

Using $\epsilon^0 = 0$, $t^0 = -1$ and $s^0 = 0$, we are plotting in Figure 3.7(b) the obtained energy bands separately for different l values. Note that due to symmetry, the $l = 1, 5$ and $l = 2, 4$ bands are degenerate. Since there are two π electrons per cell, these two π electrons fully occupy the lower π band (the solid line). The anti-bonding π band is empty (the dash line). For a comparison, we have separately calculated the bands of the full translational cell by solving instead the 12×12 eigenvale problem. The obtained result was plotted in Figure 3.7(a), showing 12 bands . Because both the usual translational and the symmetry-adapted one are associated with unitary transformations, the electronic eigenvalue spectrum should be the same. Indeed, the equivalence of the two approaches can be seen by inspecting Figure 3.7(a) and Figure 3.7(b). If all bands corresponding to all 6 l values shown in Figure 3.7(a) would be plotted on the same graph, we would see perfect overlap with the ones computed from the full translational cell of Figure 3.7(a). Thus, in the symmetry-adapted formulation the same result can be obtained by solving six 2×2 eigenvalue problems.

3.2.3 Symmetry-Adapted Tight-Binding Molecular Dynamics

The total electronic energy contained in the $N_s \cdot N_a$ symmetry-adapted domains writes:

$$E_{band} = 2 \sum_{j=1}^{n_\alpha N_0} \sum_{\kappa=-\delta\kappa(N_s-1)/2}^{\delta\kappa(N_s-1)/2} \sum_{l=0}^{N_a-1} f_j(l\kappa)\varepsilon_j(l\kappa), \tag{3.35}$$

where f is the Fermi function and $\delta\kappa = 2\pi/N_s$. Because E_{band} is invariant under the screw and angular rotations as well as under the permutations of atoms, the conditions for carrying out Symmetry-adapted MD from the TB potential are fulfilled. To perform MD, the forces acting on the N_0 atoms are needed. The force on the atom at $\mathbf{X}_m$ located due to the band energy, $\mathbf{F}_m = -\partial E_{band}/\partial \mathbf{X}_m$, writes:

$$\begin{aligned} \mathbf{F}_m = -2 \sum_{j,l\kappa} f_j(l\kappa)(\mathbf{C}^\dagger(j,l\kappa) \cdot \frac{\partial \mathbf{H}(l\kappa)}{\partial \mathbf{X}_m} \cdot \mathbf{C}(j,l\kappa) \\ - \varepsilon_j(l\kappa)\mathbf{C}^\dagger(j,l\kappa) \cdot \frac{\partial \mathbf{S}(l\kappa)}{\partial \mathbf{X}_m} \cdot \mathbf{C}(j,l\kappa)), \end{aligned} \tag{3.36}$$

which is the Hellmann-Feynman force. The above expressions are considered as $N_s \to \infty$ and κ becomes continuous. The derivatives of the Hamiltonian and overlap matrix elements are:

$$\frac{\partial \langle \alpha' n', l\kappa | H | \alpha m, l\kappa \rangle}{\partial \mathbf{X}_m} = \frac{1}{N_a N_s} \sum_{\zeta_2,\zeta_1} e^{-il\theta_2\zeta_2 - i\kappa\zeta_1} \sum_{\alpha''=1}^{n_\alpha} \frac{\partial t^0_{\alpha'',\alpha}(\mathbf{X}_{n',(\zeta_1,\zeta_2)} - \mathbf{X}_m)}{\partial \mathbf{X}_m} R^{(\zeta_1,\zeta_2)}_{\alpha',\alpha''}. \tag{3.37}$$

$$\frac{\partial \langle \alpha' n', l\kappa | \alpha m, l\kappa \rangle}{\partial \mathbf{X}_m} = \frac{1}{N_a N_s} \sum_{\zeta_2,\zeta_1} e^{-il\theta_2\zeta_2 - i\kappa\zeta_1} \sum_{\alpha''=1}^{n_\alpha} \frac{\partial s^0_{\alpha'',\alpha}(\mathbf{X}_{n',(\zeta_1,\zeta_2)} - \mathbf{X}_m)}{\partial \mathbf{X}_m} R^{(\zeta_1,\zeta_2)}_{\alpha',\alpha''}. \tag{3.38}$$

Derivatives $\partial t^0_{\alpha'',\alpha}/\partial \mathbf{X}_m$ and $\partial s^0_{\alpha'',\alpha}/\partial \mathbf{X}_m$ are given in Ref. [54]. We note that the two-body repulsive part of the tight-binding potential [54] does not necessitate specific adjustments for symmetry-adapted molecular dynamics.

3.3 The Atomistic Simulation Package *Trocadero*

The changes highlighted above will be implemented in the computational package *Trocadero* [40], which already can perform tight-binding molecular dynamics under periodic boundary conditions. A brief description of this code is given next.

This multiple-algorithms multiple-models strategy allows for an easy expansion of both new models and algorithms (our case). This code organisation allows for the easy expansion of the program, as both new models and new simulation algorithms can be incorporated into the program with minimum disruption to the pre-existing program.

In terms of available simulation algorithms, the simplest form currently implemented is what we refer to as *a single configuration calculation*, in which, given a model and a configuration of the system (a set of atomic coordinates, and in the case of periodic systems also the lattice vectors), the program returns the energy of the configuration, the atomic forces, and in a periodic system also the stress on the simulation cell. Information on the neighbours of each atom is provided, and in the case of electronic structure models the electronic density of states is calculated. However, single configuration calculations are not in themselves terribly useful, and are rarely used with the simple models currently implemented.

More useful is the possibility of performing *structural relaxation calculations*, i.e. moving the atoms in the simulation box so as to reduce the forces acting on them to zero, thus reaching a configuration of minimum energy, which in general will be a local minimum. The implemented conjugate gradients algorithm efficiently performs such structural relaxation calculations.

Both single configuration calculations and structural relaxation are concerned with the static properties of the system under study, and thus are not appropriate for studying the thermal properties of the system. For doing this we need to involve the temperature, or in other words, atomic motion. There are two well-established families of methods for doing this, namely Monte Carlo and molecular dynamics methods. The code contains only *molecular dynamics methods* and several different techniques have been implemented. *Standard microcanonical molecular dynamics* consists of numerically integrating the Newtonian equations of motion for the

atoms. These equations conserve the total energy of the system, and therefore this procedure samples the microcanonical ensemble, in which the number of particles, the volume and the energy are conserved quantities. A standard algorithm for integrating Newton's equations of motion is that due to Verlet and this is actually the one implemented in for microcanonical MD simulations.

The microcanonical ensemble is not, however, the most appropriate one in which to perform simulations, as it does not correspond to the conditions under which experiments are most commonly carried out; it is usually the temperature and/or pressure that are kept constant. These conditions correspond to the *canonical* and *isothermalisobaric* ensembles, respectively [79–82]. Molecular dynamics calculations in these ensembles are also possible in *Trocadreo*.

Regarding the microscopic models currently implemented, besides orthogonal and non-orthogonal tight-binding models, *Trocadero* has *Tersoff* and *EDIP* [83] classical potentials designed with the aim of modelling covalent systems, in which the bonding has a well-defined directionality. This feature will facilitate performing symmetry-adapted calculations under both tight-binding and classical microscopic descriptions. Note that the symmetry-adapted modeling was previously implemented [38] in conjunction with the Tersoff potential. For modeling metallic systems, where the packing density is larger and the bonding has a less directional character, a *Glue* potential [84, 85] is available to use. The symmetry-adapted implementation for the Glue potential follows the lines described in Chapter 4 for the Tersoff potential.

Chapter 4

Investigating the Stability of Silicon Nanowires via Symmetry-Adapted Tight-Binding Molecular Dynamics

In spite of a large body of experimental [86–89] and theoretical [90–98] research, the ground state of quasi one-dimensional silicon structure at the lowest diameters is not yet known. Relying on thermodynamic arguments, one conjectures that in relatively thick NWs the influence of surfaces is less important and arrangements with bulklike cores are more likely. However, as the diameter is decreased, surfaces are becoming increasingly important in the NW energetic balance [94], and quasi one-dimensional organizations with non-cubic core structures but low surface energies are possible.

To describe the ground state Si NW structure at sizes of below 10 nm, several candidates have been already envisioned: It was predicted [94] that an enhanced stability can be obtained in polycrystalline achiral Si NWs constructed with five identical crystalline prisms exposing only low energy (001) Si surfaces. In another recent study [95], wurtzite NWs with hexagonal cross sections were found to be

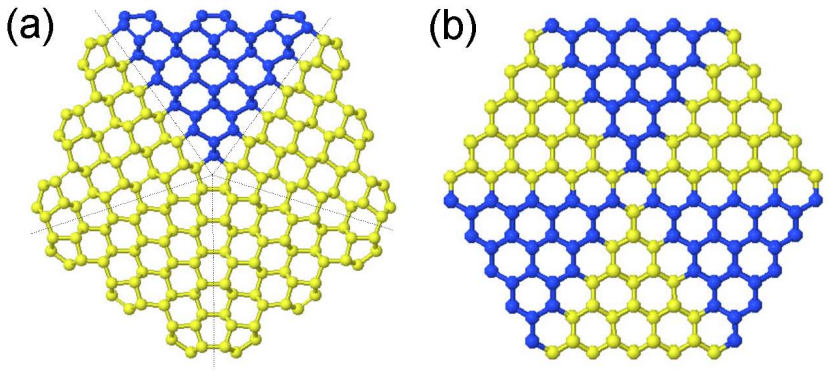

FIGURE 4.1: (a) Pentagonal Si NW (labeled P). Surface is shown in a reconstruction with *symmetric* dimers, as described with a Tersoff potential. Dotted lines indicate the stacking fault planes. The computational "angular-helical" domains are shown in blue atoms. (b) Wurtzite Si NW (labeled H) with hexagonal cross section. The surface is shown as unrelaxed. Domains with same ζ_1 are shown in same color. For both NWs only axial views are shown.

the most stable. Note that although NWs with wurtzite cores are prevalent in III-V zinc-blende semiconductors [99], they have been synthesized also in Si [89]. Finally, icosahedral Si quantum dots [100, 101] constructed from tetrahedral blocks were proposed. Because of the low formation energy of the exposed (111) surfaces, these dots are very stable. One-dimensional NWs assembled from icosahedral dots appeared [97] more favorable than the achiral pentagonal NWs of Ref. [94].

4.1 Structures of the Considered Si Nanowires

We now discus the structure of the three NW motifs presented in Figure 4.1 and 4.2. Although all three motifs have translational symmetry, they can be more economically described in the "angular-helical" representation discussed in Chapter 2.

Table 1 summarizes the exact values of the domain parameters θ_1 and θ_2 as well as algebraic expressions for the number of atoms N_0 and the number of surface atoms N_{sf} in the Symmetry-adapted domain as a function of the number of atomic layers L. The precise T_1 value is model dependent and will be determined by simulations.

TABLE 4.1: Comparison of the symmetry-adapted cells for the P, H, and I NWs. L is the number of layers, N_0 is the total number of atoms, and N_{sf} is the number of surface atoms.

NW:	P	H	I
θ_1:	0	$\pi/3$	$\pi/5$
θ_2:	$2\pi/5$	$2\pi/3$	$2\pi/5$
N_0:	$2(L-1)(2L-1)$	$2L^2$	$0.5L(L+1)(2L+1)$
N_{sf} :	$2(L-1)$	$2L$	$L(L+1)$

The NW shown in Figure 4.1(a), labeled P, exhibits a five-fold rotational symmetry. The exposed five equivalent (001) surfaces have dimer rows oriented parallel with respect to the NW axis. At the center of this NW there is a channel of pentagonal rings. The symmetry-adapted computational domain shown in blue (dark gray) is a triangular prism limited by two (111) and one (001) surfaces. The associated angular parameters are $\theta_1 = 0$ and $\theta_2 = 2\pi/5$ while T_1 equals the periodic boundary condition periodicity T. Thus, in comparison with the traditional periodic boundary condition scheme, symmetry-adapted molecular dynamics reduces to 1/5 the number of atoms that need to be accounted for. Note that to form the NW, the (111) surfaces of the symmetry-adapted domains are connected through low energy stacking fault defects. Because in the bulk Si the two (111) planes of the triangular prism form an angle $\theta = 2tan^{-1}(1/\sqrt{2})$, which is slightly different from θ_2, each domain stores elastic energy corresponding to a shear deformation with $\varepsilon = \theta_2 - \theta$.

Figure 4.1(b) shows the structure of a NW motif with a hexagonal cross section, but three-fold rotational symmetry. This NW, labeled H, has a wurtzite core structure. Although its surfaces are equivalent, they are shifted in an alternating manner along the NW axis by half of the translational period T. The symmetry-adapted computational domain represents 1/6 of the translational domain. Its parameters are $\theta_1 = \pi/3$, $T_1 = 0.5T$, and $\theta_2 = 2\pi/3$. The non-zero value of θ_1 indicates that the H NWs is generated by repeated screw and pure rotations.

The last NW motif considered, labeled I, also exhibits a five-fold rotational symmetry. The tetrahedron block shown in Figure 4.2(a) is truncated directly from

the bulk. It exposes only low-energy (111) surfaces and all faces are equilateral triangles. Twenty such blocks are combined through low-energy stacking faults to form the dot shown in Figure 4.2(b), having icosahedral I_h symmetry. The combination of three blocks shown in Figure 4.2(c) represents the symmetry-adapted domain for the I NW shown in Figure 4.2(d). The associated angular parameters are $\theta_1 = \pi/5$, $\theta_2 = 2\pi/5$. Thus, with eq. (3.23) this NW is built from screw and pure rotation isometries.

In the I NW one can identify two types of blocks: blocks (shown with yellow/light gray and blue/dark gray) that, like in the I_h dot, expose one facet and blocks (shown in gray) in which all facets are in contact with other blocks. As discussed before [97], the I NW can be also thought of as being composed of aligned polycrystalline I_h Si quantum dots that share the tetrahedron blocks shown in gray (i.e., five tetrahedral blocks at each interface). In this respect, the two crosses separated by a distance T_1 in Figure 4.2(c) mark the centers of two virtual I_h dots sharing the gray blocks. This picture helps to comprehend the strain accumulated in the I NW, discussed next.

As in the case of the P NWs, the mismatch resulted when combining the bulk tetrahedron blocks to form the I_h dot and the I NW introduces strain. In the high symmetry of the I_h dot the 20 tetrahedron blocks are equivalent and thus the mismatch strain will be equally distributed among them. More specifically, since at each vortex a radial channel of pentagonal rings is formed, each tetrahedron block around it accumulates elastic shear energy corresponding to a strain $\varepsilon = \theta_2 - \theta$. As each tetrahedron is delimited by three radial channels, it follows that the exposed faces are equilateral triangles, as can be also noted from Figure 4.2(b). The symmetry lowering to the I NW superposes additional elastic energy. In an icosahedron the tetrahedron building blocks are not regular (i.e., the exposed faces are equilateral while the internal ones are isosceles triangles). Thus, the (110) planes of the gray blocks of Figure 4.2(b) (to be shared in the I NW construction) are not perpendicular on the NW long axis. Consequently, the internal blocks will undergo additional elastic deformation, specifically by decreasing the angle made by the two (111) facets that join into the circumferential edge, Figure 4.2(b), such that the middle transversal (110) plane becomes perpendicular to the NW axis. The other tetrahedron type will also be affected by this adjustment and

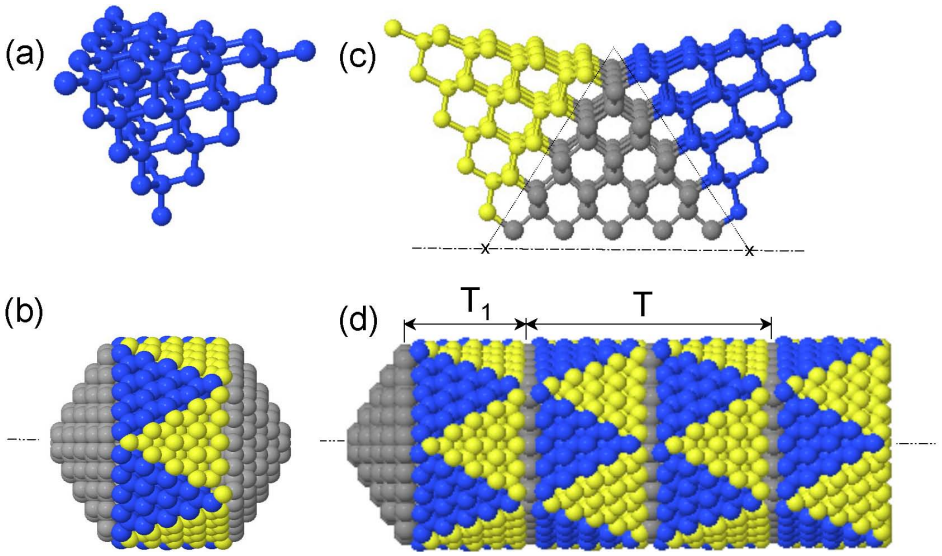

FIGURE 4.2: (a) A tetrahedron building block truncated from the bulk Si exposes four (111) surfaces. (b) Icosahedral Si dot composed of twenty equivalent tetrahedron building blocks. With a domain composed of three tetrahedron blocks, shown in (c), a NW (labeled I) with pentagonal cross section, shown in (d), can be constructed based on formula describing the NW in the "angular-helical" and parameters entered in Table 4.1 corresponding to $L = 5$. Alternatively, the I NW can be constructed from aligned icosahedral Si dots sharing the tetrahedron building blocks shown in gray.

the exposed faces will become isosceles triangles in the one-dimensional structure. From this qualitative picture one can immediately conjecture that the I NWs will store a larger strain than the P NWs and the I_h dots.

We finally note that in the I NWs the periodic boundary condition treatment is unnatural as T is L-dependent and the number of atoms in the cell under periodic boundary condition increases significantly (as $\sim L^3$). For example, for $L = 6$ there are 2730 Si atoms in the cell under periodic boundary condition but only 273 atoms in the symmetry-adapted one.

4.2 Structural Optimizations

Which non-bulk NW structural motif is in fact more energetically favorable and therefore more likely to be stable? To answer this question we recognize that the accuracy of any microscopic investigation depends critically on the level of theory

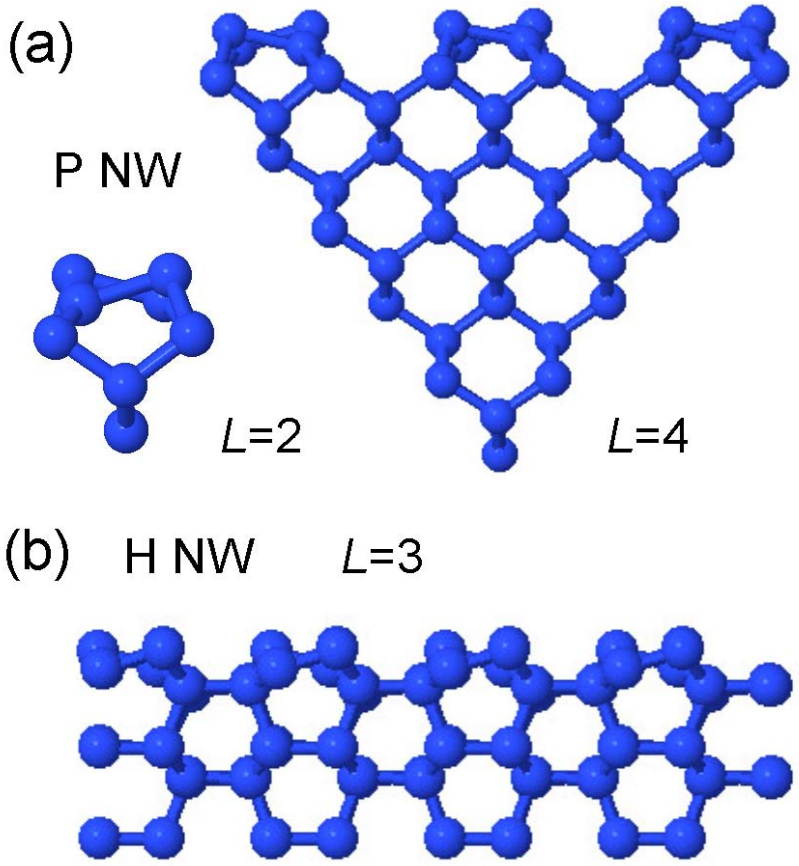

FIGURE 4.3: (a) Symmetry-adapted domain (axial view) for the P NWs with $L = 2$ and $L = 4$. The alternating buckled dimer reconstruction pattern of the surface can be observed. (b) Side view of the symmetry-adapted domain for the H NWs with $L = 3$ of length $4T_1$, showing on top the buckled dimer alternating pattern.

behind the description of the Si-Si interatomic interactions. Unfortunately, accurate *ab initio* methods formulated in the typical periodical boundary conditions context are computationally demanding and studies employing these methods can be carried out only at the smallest diameters [91, 93, 96]. They are used to complement larger scale microscopic calculations based on empirical classical potentials [61, 62], which are typically assumed to be less accurate only in the smallest size range due to the enhanced role of surfaces.

Consider for instance the description of the surface reconstruction as obtained with the widely used Stillinger-Weber [61] and Tersoff [62] classical potentials,

both used in Refs. [94, 95, 97] to describe the pentagonal NW that exposes (001) facets. The (001) Si surface has been studied with these potentials [63] and a p(2×1) *symmetric* dimer pattern was found to be the most stable. However, with density-functional theory (DFT) it was found [102] that the *alternating* asymmetric buckling of surface dimers p(2×2) is more favorable (see Figure 3.5). Since the *asymmetric* buckling is not captured, the classical treatment [61, 62] for the thinnest NWs exposing (001) surfaces will not be accurate.

We performed the structural optimization on the three selected NWs by the proposed symmetry-adapted tight-binding molecular dynamics method, carried out with a 1 fs time step, followed by conjugate gradient energy minimization scans for several T_1 parameter values until the optimal configuration was identified. Computations were carried out on the fundamental domains addressed in Table 4.1 for all I NWs and for the H NWs with odd L. Larger domains, with $2T_1$ for the P NWs and $2\theta_2$ for the H NWs with even L, were also used in order to describe the alternating reconstructions of the surfaces. Exploiting symmetry has the potential danger of missing minima with lower symmetry. Our additional calculations under periodic boundary condition carried out for the smallest NWs (with L=2) showed agreement with the symmetry-adapted data.

Figure 4.3(a) presents the optimal surface reconstruction for two P NW domains, showing an alternating buckled dimer reconstruction on top. Accounting correctly for the surface reconstruction appeared important especially for the thinnest NWs where the surface to volume ratio is largest. For example, we obtained a 20 meV/atom energy lowering from the non-alternating buckled to the alternating buckled pattern for the P NW with $L = 2$.

Remarkably, our simulations indicated that symmetry-adapted molecular dynamics is more efficient than periodic molecular dynamics under periodic boundary condition in finding the optimal surface reconstruction of the NWs. In general, during molecular dynamics the system samples many different potential energy minima, spending more time in the deeper ones. Because the small symmetry-adapted domain forbids several local minima, the system avoids these unimportant states and thus can reach faster the lowest potential energy state. This is demonstrated in Figure 4.4, which compares the evolution of temperature for a P

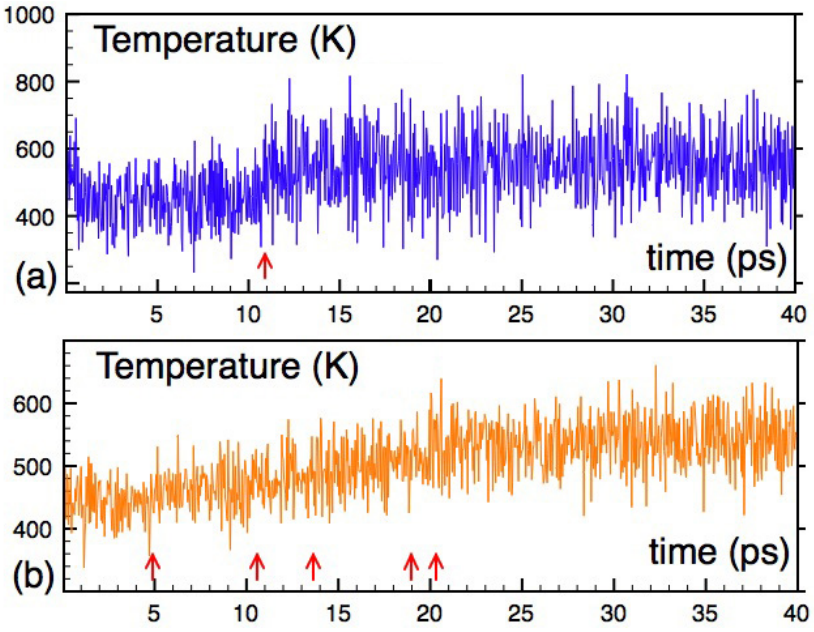

FIGURE 4.4: Temperature as a function of time in (a) symmetry-adapted molecular dynamics and (b) periodic DFTB molecular dynamics for the P NW with $L = 2$. Arrows mark transitions to an alternating surface dimer buckling.

NW with $L = 2$ in symmetry-adapted molecular dynamics and periodic molecular dynamics. To make the comparison meaningful, both simulations were initiated with velocities corresponding to the same temperature while the initial configurations exhibited an asymmetric non-alternating buckling of the surface dimers. On one hand, symmetry-adapted molecular dynamics shows for the first 10 ps an equilibration to an average temperature of $\sim$ 450 K, followed by a sharp increase to a new equilibrium temperature of $\sim$ 550 K. The $\sim$ 100 K temperature increase is caused by the lowering of the potential energy caused by the concerted transformation event to an *asymmetric* alternating buckling of the dimers on all five surfaces. The actual configuration (after the conjugate gradient run) can be seen in Figure 4.3(a). On the other hand, the temperature evolution in periodic molecular dynamics, shown in Figure 4.4 (b) exhibits a gradual increase to the $\sim$ 550 K final equilibrium temperature. When analyzing the NW structure we noted a sequence of transformations to an alternating buckled pattern occurring at the simulation times marked by arrows. Thus, although under the same temperature conditions the transformation starts earlier in periodic molecular dynamics, after 4.9 ps, and it is completed on all five faces after 20 ps. None of the states in the 5-20 ps

interval are described in symmetry-adapted molecular dynamics. In contrast, the concerted transformation occurs on all faces in the symmetry-adapted molecular dynamics run after 10.8 ps (see the up arrow in Figure 4.4 (a)). Similar comparisons were carried out for the next two larger P NWs and the symmetry-adapted molecular dynamics advantage was still noted.

The H NW surface exposes dimer rows aligned perpendicularly on the NW axis. Our symmetry-adapted tight-binding molecular dynamics optimization procedure obtained again an alternating buckled pattern of the surface dimers, as presented in Figure 4.3(b). This appears in disagreement with our obtained classical description which does not account for the buckling effect. Regarding the surfaces of the I NWs, we noted that the characteristic surface buckling of the (111) surface was severely reduced with the increase in diameter. In fact, above $2R = 2.5$ nm the surface was practically built up from flat hexagonal rings. The alternating buckled pattern was obtained on the edge surface dimer rows formed at the interface between tetrahedrons. By contrast, the surface did not appear flattened and the edge dimers did not buckle in the classical treatment.

In Figure 4.5 we report the obtained stability data for the three NW motifs as described by the two microscopic models. As can be seen from Figure 4.5(a), which plots the NWs formation energies E (measured with respect to atomic energy values) in the TB model as a function of diameter $2R$, the P and H NW motifs emerge as the most favorable. (Practically the two curves are overlapping at diameters above 2 nm.) Surprisingly, the I NW is favorable only at the very small diameters, below ~ 2.5 nm, when the I curve intersects the P one. Above this value, this NW becomes unfavorable. Interestingly, Figure 4.5(b) shows that a very different conclusion can be obtained if one relies on the classical potential data. The formation energy curves for the three NWs are very close together. In agreement with previous investigations [97], the I wire appears now more favorable than the P one and the intersections between the I and P curves, marked by the down arrow, is delayed until ~ 9 nm. In agreement also with the previous comparison [95] based on the classical Stillinger-Weber potential, the H NW motif appears overall more favorable than the P one. Comparing now the I and H NWs, we see that below 6 nm in diameter the I NW is favored.

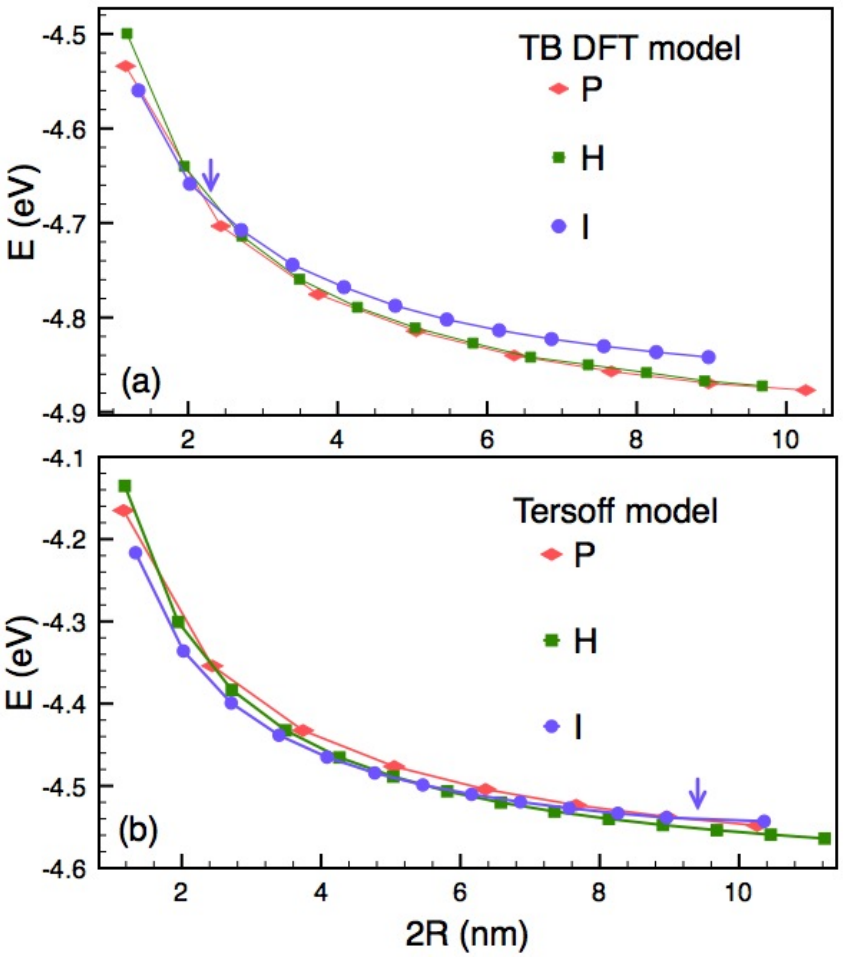

FIGURE 4.5: Size dependence of the cohesive energy for the P, H, and I Si NWs. The (a) DFT-based TB potential and (b) classical Tersoff potential give different energetic orderings. Arrows mark intersections of I and P energy curves.

4.3 Comparison of the Tight-Binding and Classical Simulation Results

To rationalize the differences between Figure 4.5(a) and (b) we have analyzed in more detail how the two microscopic models are describing each NW motif. Figure 4.6(a)-(c) plots over a large diameter range the obtained $E - E_{bulk}$ values for all NWs as obtained with the TB and Tersoff atomistic descriptions. We found it instructive to perform a Wulff decomposition of the obtained cohesive energy

data as:

$$E - E_{bulk} = \delta E_{bulk} + E_{sf} + E_e, \tag{4.1}$$

where E_{bulk} represents the cohesive energy of the crystalline NW bulk, i.e., cubic diamond bulk (-4.953 eV and -4.628 eV for TB and Tersoff potential, respectively) for the P and I NWs and the wurtzite bulk Si (-4.943 eV and -4.625 eV for the TB and Tersoff potential, respectively) for the H NW. In (13) δE_{bulk} is the bulk energy correction, which captures the elastic strain stored in the NW core. The surface E_{sf} and edge E_e energies have analytic expressions constructed by taking into account the structural parameters of the NWs. A Wulff decomposition extrapolation approach was used before to predict formation energies of NWs at larger sizes [94]. Here, by identifying in the atomistic data the magnitude of the various contributions, we use it to obtain more insight about the differences between the two models.

In Figure 4.6(a) we see that overall the TB description of the P NW gives a lower energy. The differences are especially significant at the smaller sizes (44 meV at $L = 2$) and they diminish as the NW diameter is increased. Using the structural information entered in Table 1 and recognizing that this NW structure has no edge energy penalty, we obtain that the cohesive energy should scale with the number of layers L as

$$E_P(L) - E^c_{bulk} = \delta E_{bulk} + \frac{\gamma_P}{2L - 1}, \tag{4.2}$$

where γ_P is the surface energy penalty per surface atom and δE_{bulk} represents the shear elastic energy stored in these structures. Fitting to the atomistic data we obtained γ_P of 1.25 eV/atom with TB and 1.39 eV/atom with Tersoff description. For both models we found that δE_{bulk} is small and can be neglected. Thus, the energetic differences noted in Figure 4.6(a) can be attributed mainly to the inability of the Tersoff potential to correctly describe the exposed Si (001) surfaces.

Moving on to the H NW, Figure 4.6(b) shows similar differences with a classical–TB agreement at large diameters. The H NW does not contain edge and bulk correction terms. Relying on the algebraic form

$$E_H(L) - E^w_{bulk} = \frac{\gamma_H}{L}, \tag{4.3}$$

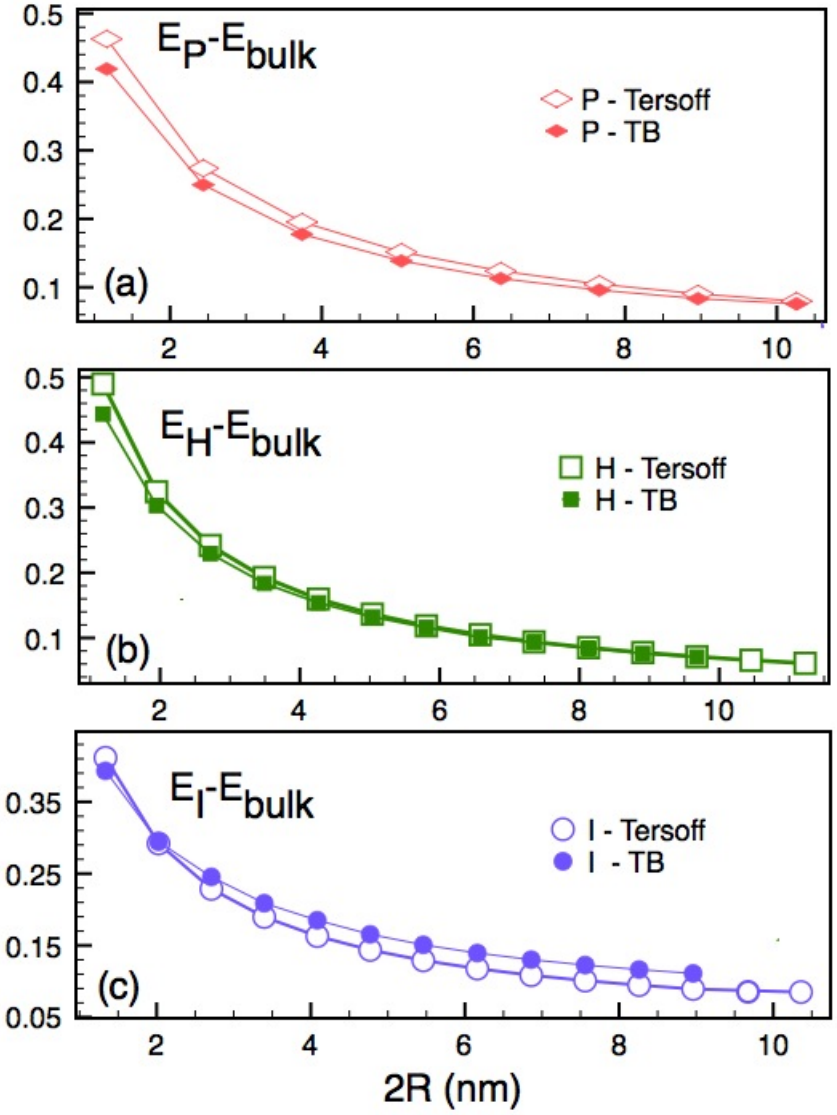

FIGURE 4.6: (a) P, (b) H, and (c) I Si NWs described with the TB (full markers) and Tersoff (open markers) potential. The zero of energy is taken to be the cohesive energy of the cubic diamond Si in (a) and (c), and the wurtzite Si in (b).

a least-squares fitting of the two data sets obtained γ_H as 0.88 eV/atom in TB and 0.97 eV/atom with the classical potential.

Figure 4.6(c) shows even larger differences between the two I NW descriptions. While at the lowest diameter the TB model yields a lower energy, the classical potential-based modeling gives a lower energy for $L \geq 4$ or $2R \geq 2.5$ nm. We fitted the data to the algebraic form

$$E_I(L) - E^c_{bulk} = \delta E_{bulk} + \frac{\gamma_I}{L + 0.5} + \frac{12\delta}{(L+1)(2L+1)}, \tag{4.4}$$

which was constructed based on the structural parameters entered in Table 4.1 and the observation that there are $6L$ edge atoms in each computational domain. Due to the different surface reconstruction above 2.5 nm in diameter, the first two TB data points were not included in the fitting. For δE_{bulk} we obtained 36 meV/atom with TB versus 21 meV/atom with classical. Both models confirm the I NW stores significant strain energy but due to the errors in reproducing the elastic constants, the strain component is not well represented by the classical model. Further, we found the flattened surface obtained with TB has a higher 980 meV/atom cost when compared with the 900 meV/atom obtained classically. Finally, we found that the buckling of the dimers located on the edges lowers the TB energy as $\delta = -37$ meV/atom. A δ value of 38 meV/atom obtained from the classical data agrees with our observation that this model does not capture the dimer buckling. As can be seen from eq. (4.4), the edge energy component is the least important, and the TB description gives a higher energy because the bulk correction and the surface energy count more in the energy balance. We have summarized all the fitted data of the energy components in the Wulff decomposition in Table 4.2.

In conclusion, from our investigations on the stability of Si NWs we see that the use of a quantum-mechanical description of the atomic bonding is critical as the classical potentials [62] introduces significant errors. Moreover, these errors are not systematic: On one hand, for the P and H NWs the errors are larger at smaller diameters as they are mainly caused by the inability of the classical potential to describe the surface reconstruction. On the other hand, for the I NW the errors are large even at large diameters, as they are due to the inability to describe the strain stored in the NW core as well as the higher surface energy penalty. The

TABLE 4.2: Summary of energy values obtained from the Wulff-like energy decomposition of the three NWs.

NW:		P	H	I
E_{bulk}	TB	-4.953	-4.943	-4.953
(eV)	Tersoff	-4.628	-4.625	-4.628
δE_{bulk}	TB	0	–	36
(meV)	Tersoff	0	–	21
γ	TB	1.25	0.88	0.98
(eV)	Tersoff	1.39	0.97	0.90
δ	TB	–	–	-37
(meV)	Tersoff	–	–	38

magnitude of these errors are causing the energetic ordering of the NW structures not to be identical in the two microscopic descriptions. Hence, different stability conclusions [95, 97] can be reached from the two data sets. We note that the usual approach [94, 95] of complementing the large scale classical calculations with expensive quantum calculations carried out at the smallest diameters (i.e., that assumes that corrections are needed at the smallest diameters only) should be used with care. For example, judging the I NW stability by combining the Tersoff data with the affordable first two TB data points under periodic boundary condition would be deceiving.

We plan to further investigate with symmetry-adapted tight-binding molecular dynamics the mechanical response of the H, P, and I NWs to mechanical deformations. In addition to the already noted advantage of the method in imposing mechanical deformation, with tight-binding we will also have an accurate description of the surface reconstruction. Thus, we will be able to capture correctly the influence of the surface stress on the mechanical response. It will be very interesting to see wether the Young's modulus increases or decreases with size. We will consider not only NWs with bare Si surfaces but also with hydrogen termination. The deformation-induced changes in the electronic band structure will be quantified. The response of these NWs to severe bending deformations will be also

studied. Unlike with the classical potential treatment, brittle failure is described by the tight-binding model and thus it can be a possible way of response. We will also continue our comparison with the behavior obtained with the Tersoff potential. The obtained results will be able to clarify whether or not the quantum mechanical description of bonding is necessary in describing Si NWs.

Chapter 5

Studies for the Mechanical Properties of Carbon Nanotubes via Symmetry-Adapted Molecular Dynamics

Among the numerous subjects of nanomechanics research (tips, contact junctions, pores, whiskers, etc.), carbon nanotubes have earned a special place, receiving much attention. Their molecularly precise structure, elongated and hollow shape, effective absence of a surface (which is of no difference from the bulk, at least for the single-walled carbon nanotubes), and superlative covalent bond strength are among the traits that put carbon nanotubes in the focus of nanomechanics. However, experiments are difficult at this small scale. A detailed understanding of CNTs' mechanical response is essential for advancing applications [103, 104]. Atomistic calculations prove to be valuable tools of investigations. Often they are used to provide the necessary input for deriving practical continuum models [5, 21, 105], such as the linear-elastic isotropic continuum [5], which can be used for understanding the CNTs' mechanics using the well-established relations of macroscopic elasticity, without the need of repeating the microscopic calculations.

Multi-scale modeling of CNTs has been recently addressed. Belytschko et al. [21] developed a membrane model tied to the atomistic description provided by the

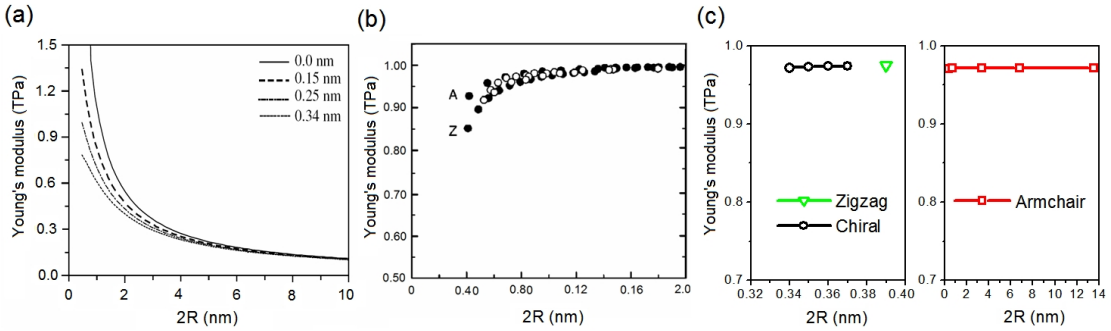

FIGURE 5.1: Scaling of the Young's modulus with diameter (2R), as obtained with different theoretical approaches: (a) a continuum model relying atomistic computational data, from Ref. [1]. (The Young's modulus is plotted considering several values for the thickness of the associated nanoshell (b) a lattice dynamics model from Ref. [2]. For the solid circles, "A" stands for "armchair" and "Z" for "zigzag". Between them, the open circles correspond the chiral SWCNTs; (c) a force-constant model, from Ref. [3].

Brenners potential [106]. Huang et al. [107] developed an atomic scale finite-element method linked to the same potential. Both approaches are valuable because they show how continuum can be built from the atomic scale by means of the Cauchy-Born rule [108]. However, both methods are lacking predictive accuracy. Briefly, the continuum elastic potential is obtained by equating the deformation energy of an symmetry-adapted cell of the lattice to that of an equivalent volume of the continuum. The resulting constitutive model will depend only on the accurate atomistic description of the system, without additional phenomenological input. Thus, any inaccuracy of the "parent" classical atomistic model directly transfers to the continuum. In the classical potential of Brenner [106] the inaccuracy is severe. For example, the computed CNTs Young's moduli deviate by ~ 0.5 TPa from experiment or quantum mechanical predictions [53].

It is important to note that it is not a coincidence that both approaches mentioned above are relying on a short-ranged classical potential. The atomistic-continuum linking procedure equates the energy dependence on stretch and curvature of the hyperelastic field with the one obtained from the atomistic description of graphene. As it also becomes apparent from the next section, the atomistic bending calculations can be carried out with classical potentials but not with the quantum mechanical description under periodic boundary conditions.

5.1 Difficulties of the Traditional Periodic Boundary Condition Formulations in Modeling Linear Elastic Properties of SWCNTs

Young's modulus of elongated achiral SWCNTs was accurately computed with density functional theory [67] and tight-binding [50] methods. However, because of the large number of atoms in the translational unit cells of chiral nanotubes (see Figure 2.4 from Chapter 2), the scaling with chirality and diameter cannot not be computed with the most accurate quantum method in the periodic boundary condition formulations. As a result most scaling laws for the Young's modulus were obtained either from direct empirical atomistic molecular dynamics simulations or from continuum elastic models build on an empirical atomistic description [1, 3, 51, 109, 110]. Contradictory results were reported: For example, (i) calculations carried out with the continuum model of SWCNT proposed by Endo et al. [1] predicted that the Young's modulus decreases with diameter, from $\sim$ 1.2 TPa at 1 nm to $\sim$ 0.1 TPa at 10 nm. Yet, (ii) a model based on lattice dynamics by Popov et al. [2] obtained a qualitatively different behavior: in the range of 0.4 nm to 0.8 nm the Young's modulus increases with diameter, from 0.8 TPa to 1.0 TPa. Beyond the 0.8 nm diameter, the Young's modulus remained constant at about 1.0 TPa, regardless of chirality. Although this second trend seems reasonable, the values predicted by Popov do not compare well with the values predicted with DFT and tight-binding methods. Finally, (iii) full atomistic calculation [3] using force-constant pair potential showed that the Young's modulus is roughly constant over the whole range of diameter. We have summarized the results (i)-(iii) in Figure 5.1, which illustrates the unreliability of modeling the mechanical properties of SWCNTs within the classical empirical approaches.

Very important, we have to note that because the CNT's walls are monolayers, their thickness h is not well defined. There is debate [5] centered around the appropriate h value. To see the differences that arise solely due to the interatomic potential one can compare the surface Young's modulus [50] $Y_s = Yh$, which is independent of h. With Brenner's first- and second-generation potentials [106,

111], Y_s is 159 GPa·nm [112, 113] and 236 GPa·nm [112], respectively, much lower than the 345 GPa·nm reported with DFT [67].

Imposing torsional deformation to SWCNTs described under the traditional periodic boundary condition is cumbersome. This is because under periodic boundary condition, the "available" torsional angles are discrete and constrained by the rotational symmetry of the SWCNTs and the number of translational cells satisfying periodic boundary condition. The large number of translational cells needed to carry out calculations of SWCNTs under small torsional angles prohibit a quantum microscopic approach even for achiral SWCNTs. For instance, a medium-sized $(12, 12)$ SWCNT has a translational unit cell with only 48 atoms. However, 300 such cells, containing $14,400$ atoms are needed to impose a $0.04°/\mathring{A}$ torsional deformation. Thus, only continuum model and atomistic classical potentials are feasible to calculate quantities such as the torsional modulus.

5.2 Elasticity of Ideal Single-Walled Carbon Nanotubes via Symmetry-Adapted Molecular Dynamics

Since we want to establish the scaling of the elastic response, the range of the isotropic continuum have to be clarified in advance. Therefore calculations have to be performed to cover a wide diameter range and most possible chirality. Under periodic boundary conditions, such calculations can not be accomplished.

As in Chapter 2, a carbon nanotube (Figure 2.5) can be descried with only two-atom repeating domain (objective domain) under a "helical-angular representation" with

$$\mathbf{X}_{n,(\zeta_1,\zeta_2)} = \mathbf{R}_2^{\zeta_2}\,\mathbf{R}_1^{\zeta_1}\mathbf{X}_n + \zeta_1\mathbf{T}_1, \tag{5.1}$$

where, θ_1, θ_2 and $\mathbf{T}_1$ stand for the parameters for a (n, m) carbon nanotubes.

In order to define infinitesimal elastic moduli of a CNT, it is essential to first identify the stress-free equilibrium states. Note that given the (n, m) indexes, the values for θ_1 and θ_2 are exact. However, the isometric mapping that wraps the

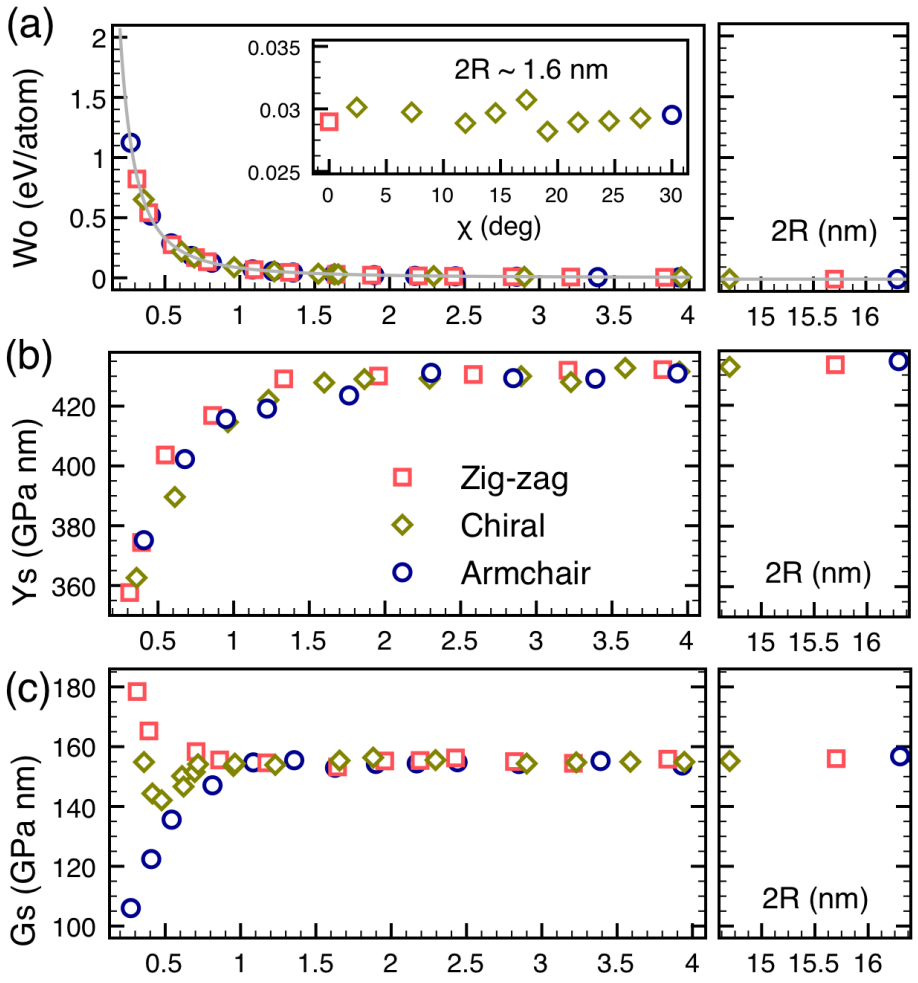

FIGURE 5.2: (a) Curvature-strain energy W_0. (b) Young's Ys and (c) shear modulus Gs as a function of the CNT diameter 2R. Inset shows W_0 dependence with χ at a constant diameter.

graphene sheet into the cylindrical geometry is not precisely a CNT at equilibrium as the carbon-carbon bond lengths will differ in general from their values in the flat geometry. We identified the equilibrium CNT configurations through conjugate gradient potential energy surface scans performed on the two-atom reduced cell under different $|\mathbf{T}_1|$ values.

In Figure 5.2(a) we plot the obtained strain energy W_0, defined as the difference in energy (measured per atom) between the optimal CNT configuration and the corresponding flat sheet, as a function of the CNT diameter $2R$. The characteristic behavior $W_0 = C/2R^2$ is obtained with $C = 4.13$ eV$\mathring{A}^2/atom$, which is in very good agreement with the DFT data [67]. Note the large difference with

the 2.2 eV$\mathring{A}^2/atom$ and 1.8 eV$\mathring{A}^2/atom$ values obtained [21] using the first- and second-generation Brenner's potentials, respectively. No χ-dependence was obtained, as can be noted also from the insert showing W versus χ for an equal-radius CNT family. Adopting a surface-without-thickness membrane [21] representation of graphene, the associated bending rigidity is $D_b = C/S_0$, where $S_0 = 2.6$ $\mathring{A}^2$ is the surface per atom defined by the tube at equilibrium.

Axial extension and compression to a (n, m) CNT was applied by changing $|\mathbf{T}_1|$ to $(1+\varepsilon)|\mathbf{T}_1|$, with the applied strain ε being varied in the $(-0.5\% : 0.5\%)$ range. The intrinsic θ_1 and θ_2 angles were kept fixed. The obtained size dependence of $Y_s = (1/S_o)d^2W/d\varepsilon^2$ is displayed in Figure 5.2(b). In contrast with other results [114], Y_s appears insensitive to χ. The axial elasticity of CNTs appears similar to the in-plane one of graphene apart from effects due the tube curvature. Above $\sim$ 1.25 nm Y_s is practically constant and takes the 430 GPa·nm value of graphene. The agreement with previous TB calculations [50], carried out in the translational representation of the CNTs, confirms the validity of our symmetry-adapted scheme. For $2R < 1.25$ nm Y_s softens, which is in disagreement for example with the data [107] obtained using the second-generation Brenner's potential [111].

An axial twist rate γ was imposed by varying the intrinsic angle θ_1 to $\theta_1 + \gamma|\mathbf{T}_1|$. Because translational periodicity is not explicitly accounted for in our symmetry-adapted MD [115], any torsional strain rate can be prescribed. By contrast, in the translational formulation limited choices for γ are available [116], making calculations of elastic moduli cumbersome. The resulting shear strain $\varepsilon' = \gamma R$ was varied in the $(-0.5\% : 0.5\%)$ range, while $|\mathbf{T}_1|$ was kept constant.

Figure 5.2(c) displays the obtained surface shear modulus, $G_s = (1/S_o)d^2W/d\varepsilon'^2$. For $2R > 1.25$ nm, G_s is not sensitive to χ and converges quickly to the 156 GPa·nm value of graphene. This value is higher than the 113 GPa·nm [117] reported recently from the second-generation Brenner's potential [111] and is in excellent agreement with the 157 GPa·nm from DFT [116]. For $2R < 1.25$ nm there is a pronounced splitting over χ with G_s bounded from above by zig-zag tubes and from below by armchair CNTs.

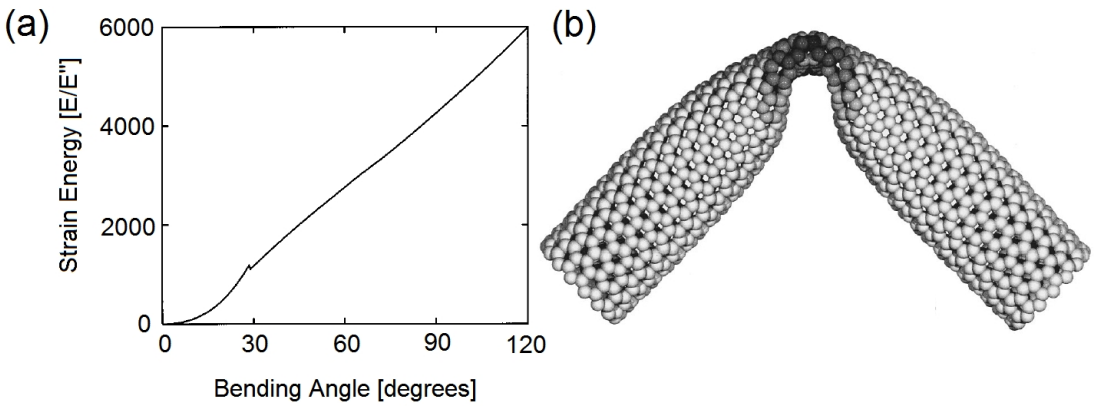

FIGURE 5.3: (a) The strain energy of a SWCNT with diameter ~ 1.2 nm as a function of the bending angle. The tip in the curve is associated with the emergence of buckling. (b) Buckled SWCNT corresponding to the linear region of the strain energy shown in (a). Adapted from Ref. [4]

The χ-dependence for G_s for $2R < 1.25$ nm unequivocally shows anisotropy. Interestingly, the HiPco-produced CNTs fall within this size-range. However, our TB data for $2R > 1.25$ nm shows that both Y_s and G_s are practically converged to the values of isotropic graphene. Thus, the isotropic CNT model is justified and we have [21] $G_s = Y_s/2(1+\nu_s)$. The resulting value for the Poisson ratio $\nu_s = 0.38$ is lower than the one obtained with the Brenner's potential [21] but still larger than in experiment. In spite of previous criticism [21], for practical reasons it is also useful to give a CNT elastic thin-shell model [5]. Thus, we expressed $D_b = Yh^3/12$ and $Y_s = Yh$. Using our TB data we obtained $h = 0.8$ $\mathring{A}$ and $Y = 5.2$ TPa.

In summary, we performed an extensive study of CNTs' elasticity. The use of the TB potential is needed since the transferability of commonly used bond-order potentials for hydrocarbons is very limited. The good agreement obtained here for Y_s and G_s with the available DFT data assures that the employed TB potential gives a reliable quantitative description of CNTs' elasticity. We addressed a large catalog of CNTs and obtain the scaling of the elastic response beyond the errors of the numerical procedures. Calculations were possible due to the substantial simplifications in the number of atoms introduced by the symmetry-adapted description of mechanically deformed CNTs. The unique conjuncture of the size and chirality dependence for both Y_s and G_s validates the isotropic continuum idealization for CNTs with $2R > 1.25$ nm.

5.3 Improper Boundary Conditions of Conventional Formulations in Modeling Non-linear Elastic Properties of SWCNTs

Beyond the linear regime, the SWCNTs exhibit buckling both under extreme bending [4, 5] and torsional [5] deformations. Buckling has been the subject of a number of theoretical investigations, most dealing with the understanding of the morphology of the buckling and how their emergence scales with the nanotube diameter. On one hand, atomistic calculations based on the classical Tersoff-Brenner potential [62, 106] showed that SWCNTs under severe bending strains [5, 118, 119] are reaching a critical curvature beyond which buckling occurs. In the two regimes the strain energy varies qualitatively different with the bending curvature. While initially the strain energy increases quadratically, it becomes linear beyond a critical curvature. For example [4], Figure 5.3(a) plots the strain energy as a function of bending angle (curvature). One can see that the linear region of strain energy is up to 120° where the CNT is free of defect or fracture even under severe strain. When the bending strain is released, the SWCNT returns to its initial straight configuration without any hysteresis. Figure 5.3(b) shows the atomistic structure of the buckled SWCNT, showing a characteristic kink in the middle. On the other hand, simulations based on continuum models of SWCNTs considered longer nanotubes [18, 22, 120, 121] and found the existence of an additional intermediate post-buckling regime where a rippling mode is developed consisting of multiple kinks instead of local kink.

It should be noted that in all atomistic simulations [18, 22, 118–123] bending was imposed by fixing the two ends of SWCNTs. More precisely, the SWCNTs were fully relaxed and then bent with uniform curvature. Finally, the ends were fixed and the SWCNTs were again relaxed. Clearly, in addition to bending, this procedure introduces a surplus of strain that is not properly quantified. For small computational cells, such as in the simulations reported in Ref. [4], this effect could dominate the observed behavior.

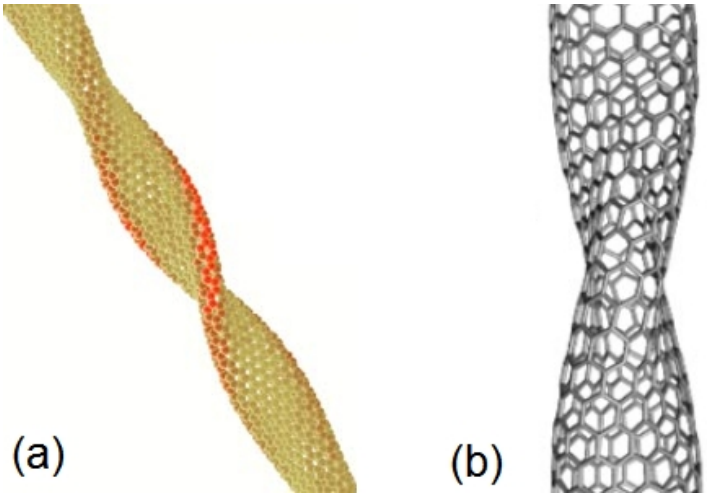

FIGURE 5.4: A longer SWCNT cylinder flattens into a straight axial spiral (a). A shorter SWCNT collapses locally from the cross-section (b). In both simulations the torsional deformation was imposed by keeping fixed the end atoms (which are not shown in (a)). Adapted from Ref. [5] and [6]

The torsional deformation of CNTs were also intensively studied theoretically [22, 124–126] under the same type of boundary condition in which the end atoms are kept fixed and circular. On one hand, this approximation could be physically justifiable by a presence of rigid caps on normally closed ends of a molecule, which deter the through flattening necessary for the helix to form. On the other hand, this approximation is too strong considering that the simulated nanotube is much shorter than the experimentally observed. Indeed, to describe the structural instability of SWCNTs when the torsional strain is beyond the linear elastic regime, two-buckling states were identified [5, 6, 127]. For longer nanotubes, a global torsional buckling in terms of a flattened axial spiral across the whole length of CNTs was obtained [5]. As shown in Figure 5.4(a), see Ref. [5], the buckling deformation distributes uniformly along the SWCNT. In Figure 5.4(b), see Ref. [6] we show the result of a simulation on a shorter SWCNT under severe torsional strain. The two ends of SWCNT were kept fixed. When the buckling deformation is initiated, a local collapse at the cross-section is developed. However, the relaxation is prohibited at the fixed ends. This ending effect will reinforce the applied strain more than the torsional strain of interest.

Finally, we emphasize that because of the high computational demand in terms of the number of atoms, all microscopic studies of SWCNTs under severe bending

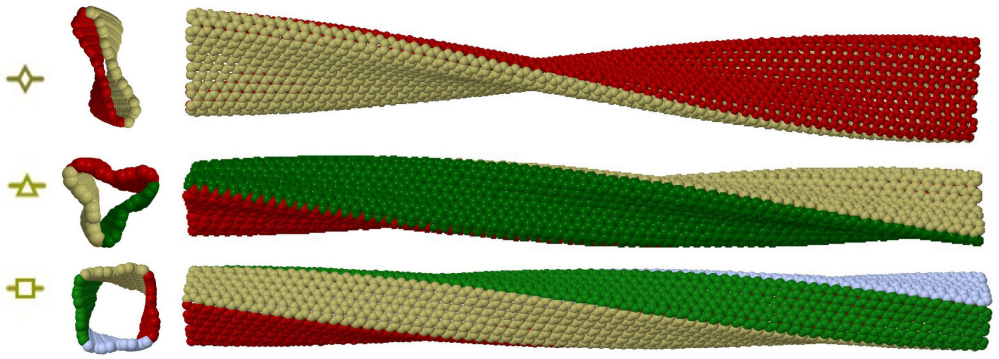

FIGURE 5.5: Rippling patterns in a (12,12) CNT under 10^0/nm twist. Colors correspond to azimuthal replicas of the repeating cell.

and torsion are employing a classical description of the carbon-carbon bonding, with the Tersoff-Brenner potential as the most widely used. In addition to the deficiencies of this potential outlined above, the difficulties in describing the fracture mechanics should be also noted. Recently, it has been demonstrated [128] that SWCNT fracture by direct bond breaking is a likely response mechanism of SWCNTs under large deformations. On the other hand, a quantum mechanical description such as tight-binding, would be able to describe alternative to buckling mechanisms that could involve the breaking of the bonds.

5.4 Rippled States in Carbon Nanotubes under *pure* Torsion via Symmetry-Adapted Molecular Dynamics

We indicate the utility of the symmetry-adapted MD method in situations involving bifurcation and complex shape changes under torsional deformations. The examples presented in Figure 5.5 demonstrate that we can describe severe buckling patterns that arise when a $(12, 12)$ tube is subjected to a twist of $10°$/nm. These wave-like modes involve long range rippling along axis, possessing larger translation periodicity with the repeating cell containing up to 1728 atoms.

In symmetry-adapted MD, the procedure for applying an arbitrary axial twist per unit length of α rad/nm at fixed strain is as follows: while preserving the

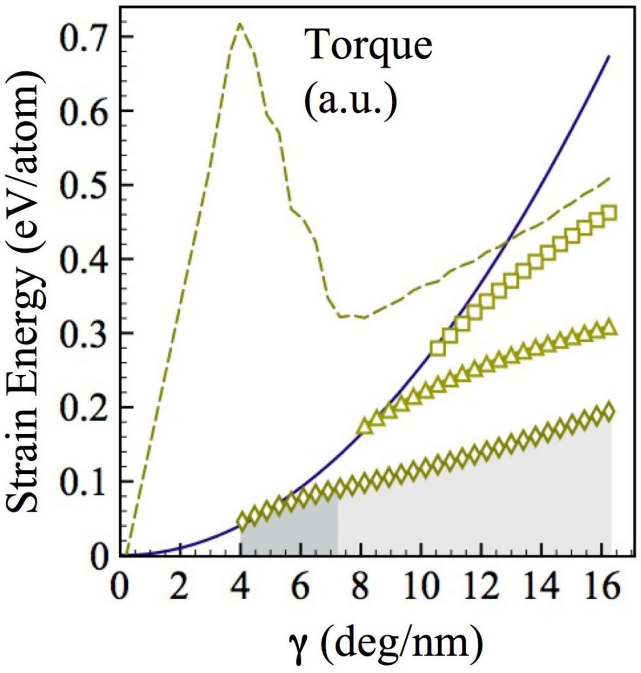

FIGURE 5.6: Strain energy vs. twist rate γ for cylinder idealized shape and rippling modes. Torque (in arbitrary units) for the two-lobe mode reveals two stages of rippling, also marked with two gray levels.

equilibrium value for $\mathbf{T}_1$, the angle θ_1 is modified to $\theta_1 - \alpha\,|\mathbf{T}_1|$. This simple procedure contrasts with the relative rigidity imposed by periodic MD, where α is constrained by the rotational symmetry of the tube and the number of unit cells. The wave-like modes were individually computed from three repeating cells delineated by the translational vector $\mathbf{T}$ but different θ_2 values, 180^0, 120^0, and 90^0. These cells contain 24, 18, and 12 atoms, respectively.

At this moment, it is also worth pointing out that in the translational MD frame, not only a large translational cell is inevitable but also discrete twist rate is allowed merely.

The capability of allowing an arbitrary twist along with the ability to study in a decoupled way the distinct deformation modes allows one to precisely pinpoint the critical level of twist beyond which the cylinder shape becomes unstable, i.e., the bifurcation point. To identify the optimal configurations we used symmetry-adapted MD as an optimization tool by carrying out a combination of MD followed

by conjugate-gradient energy minimizations. We were able to unambiguously identify the fundamental rippling mode and pinpoint the level of twist beyond which the cylinder shape becomes first unstable, i.e., the bifurcation point. The results of a series of careful energy minimizations are summarized in Figure 5.6, where plots of energy vs. the twist angle α are shown for three choices of repeating domains.

The importance range of the various modes can be judged from Figure 5.6, which shows the computed strain-energies vs. γ. The curve obtained from a 4 atom repeating cell with $\theta_2 = 30^0$ (thin line) is a useful reference as the CNT's cylinder shape is preserved. At lower strain this state is stable but beyond 4^0/nm the two-lobe buckling state lowers significantly the elastic energy. The perfect structure can also assume the three- and four-lobe buckled states at 7^0/nm and 9^0/nm, respectively, but the two-lobe morphology stays favorable. We conjuncture that modes exist as distinct states and twisting doesn't mix them by driving further circumferential rippling.

The evolution of torque (energy derivative with γ), Figure 5.6, reveals that the two-lobe rippling develops in two stages. The first is a transient one and initiates at the bifurcation, where the linear torque variation is interrupted by a rather abrupt drop. The cylinder shape develops ridges and furrows as the torque's rate is negative. The minimal distance between furrows decreases until a van der Waals equilibrium distance of 3.4 Å is reached at 7.2^0/nm. Here the transient stage is complete and torque's rate of growth switches from negative to positive. In this second stage there is no notable change in shape of the collapsed cross section.

We emphasize that although the nonlinear instabilities under torsion have been noticed before [5] and [6], the symmetry-adapted MD method allows for an unprecedented characterization of bifurcation points and a decoupled study of the various response modes. The planned tight-binding treatment will offer the first accurate description of the nonlinear response of nanotubes to severe torsional deformations. Because we will explicitly account for the electronic states, we will also be able to describe the changes in electronic properties under various levels of deformations. Such results are of great interest for the NEMS device [103].

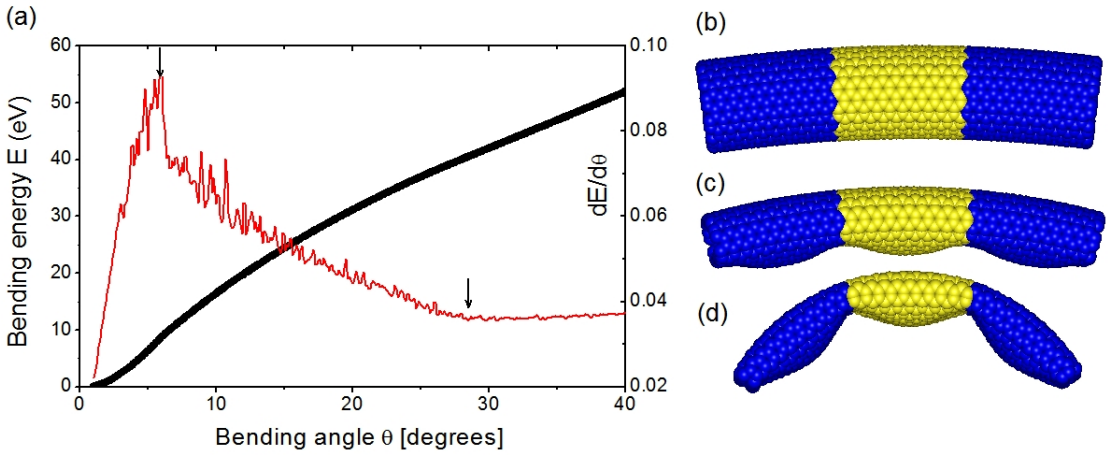

FIGURE 5.7: (a) Energy of a (12,12) SWCNT (black line) and its derivative $dE/d\theta$ (red line) as functions of bending angle. The two arrows indicate the critical bending angles where the quadratic growth of energy ends (left arrow) and where the linear growth of energy starts (right arrow). The shown nanotube structures correspond in (b) to linear elastic regime with $\theta_2 = 6°$ and to the nonlinear bending regime in (c) with $\theta_2 = 20°$ and (d) with $\theta_2 = 35°$. Simulations were carried out on a 480 atom cell shown in yellow. The blue atoms indicate replicas of the simulation cell.

5.5 Rippled States in Carbon Nanotubes under *pure* Bending via Symmetry-Adapted Molecular Dynamics

We also indicate how the method can be used to study bending deformations in nanotubes: In the framework provided by formula (3.23), bending can be imposed via the rotation matrix $\mathbf{R}_2$ and by choosing $\mathbf{R}_1 = \mathbf{I}$, $\mathbf{T_1} = \mathbf{0}$, while the selected simulation domain should capture the full circumference of the tube.

Figure 5.7(a) shows results from a series of optimization calculations performed on a translational cell containing 480 atoms from a $(12, 12)$ tube with a length of 2.6 nm. We found that the bending energy can be expressed as

$$E = \frac{1}{2} K \theta_2^a, \tag{5.2}$$

where K is the bending force constant. At small bending the energy measured

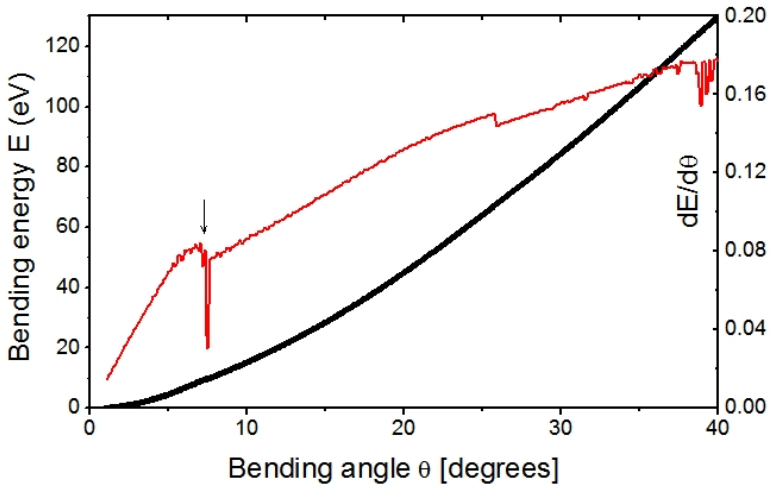

FIGURE 5.8: (a) Bending energy (dark line) and its derivative $dE/d\theta$ (red line) as functions of bending angle θ. Like in the previous figure, a (12,12) SWCNT containing 480 atoms was considered. However, here bending was imposed by freezing the end atoms.

grows quadratically ($a = 2$), where $K = 0.43$ eV rad^{-2}. The optimized bent geometry of Figure 5.7(b) presents the relaxed bent structure (yellow) and two replicas (blue) obtained with formula (3.23). Under higher bending for θ_2 beyond a critical angle of 7.1°, the SWCNT does not break but instead it buckles, as can be observed in Figures 5.7(c) and (d). The critical angle separating the linear-buckling regime was determined by analyzing the derivative of bending energy to the bending angle, shown in red curve in Figure 5.7(a). One can clearly see the descending of the derivative starting from the point marked by the first down arrow. The gradual decreasing of the red curve indicates $0 < a < 1$, corresponding to the transient regime identified recently from large scale atomistic simulations [122]. This regime is not well explored and many previous works on the subject did not identify such transient bending regime [4, 5]. The second down-arrow marks the ending of the transient regime. The derivative curve becomes horizontal indicating the linear growth of bending energy ($a = 1$). This regime was previously identified by most workers [4, 5]. We suspect that the difficulty of previous methods in describing the transient bending regime are related with the *ad hoc* method of imposing the bending deformation, by keeping the end atoms fixed. The same boundary conditions were used in Ref. [122] but the size of the nanotube was larger, such as the end effects became less important.

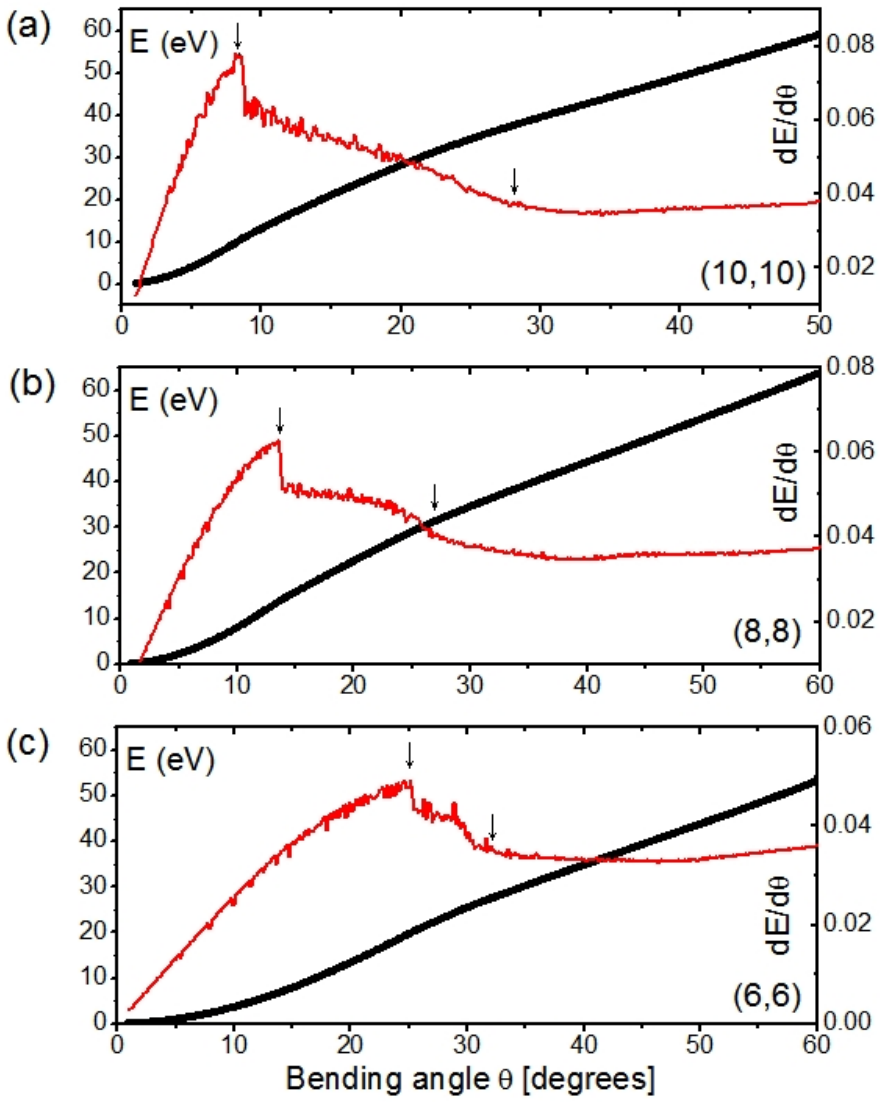

FIGURE 5.9: Bending energy E (dark line) as functions of the bending angle θ (a) (10,10), (b) (8,8) and (c) (6,6) SWCNT with a length of 2.6 nm. The derivative $dE/d\theta$ (red line) is also shown. As before, the down arrows mark transitions to another bending regime.

Interestingly, in our preliminary investigations we have seen that the bending-strain energy dependence is very different under the traditional fixed-ends boundary conditions. This is demonstrated in Figure. 5.8 showing the 480 atoms (12,12) CNT now bent under the traditional fixed-end boundary conditions. The strain dependence beyond the critical point (marked by the down arrow) is very different from the one noted in Figure 5.7, which confirms our suspicion and also illustrates the importance of the new approach.

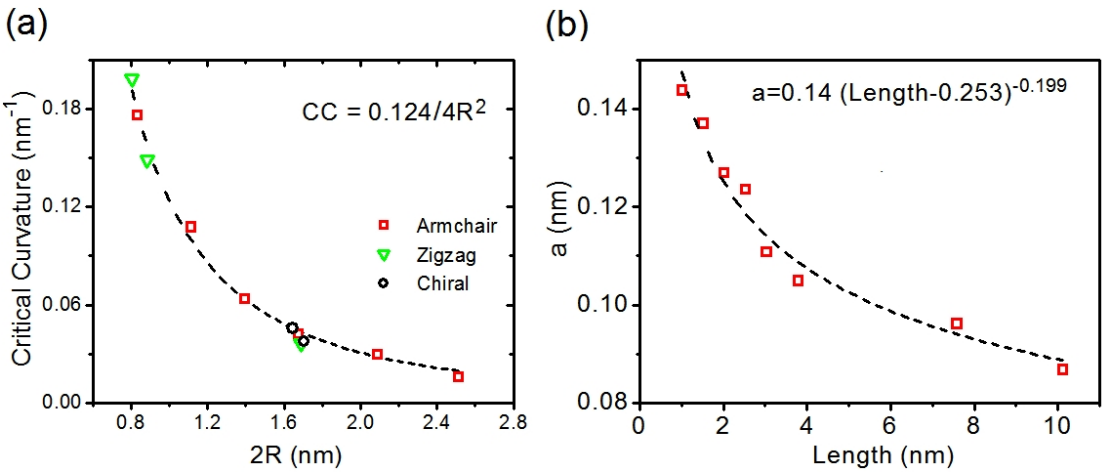

FIGURE 5.10: (a) Bending critical curvature (CC) as a function of diameter for armchair, zigzag and chiral SWCNTs. The dependence was fitted as $CC = a/4R^2$, where the $a = 0.124$ nm. (b) Critical curvature coefficient a as a function of length for a (6,6) SWCNT.

In order to further explore the observed $0 < a < 1$ buckling behavior, we have considered the role played by the diameter of SWCNT. We have performed bending simulations on $(6, 6)$, $(8, 8)$ and $(10, 10)$ SWCNT having the same length of 2.6 nm and studied their buckling behavior. As shown in Figure 5.9, the transient regime narrows with decreasing size but still exists. We plan to continue these investigations with the more precise tight-binding approach.

Turning to our symmetry-adapted MD calculations, we can also establish the dependence of the critical buckling curvature on diameter, length and chirality. Some obtained results are summarized in Figure 5.10. Figure 5.10(a) shows that the obtained dependence for the critical curvature, which varies inversely proportional with the square of diameter, which is consistent with previous works [4, 5]:

$$CC = \frac{a}{4R^2}. \tag{5.3}$$

The length of the various SWCNTs considered in the simulation was taken equal. The fitted value for the coefficient a was 0.124 nm. Figure 5.10(a) also shows that the critical curvature is almost independent of the chirality. We have also obtained that the critical curvature coefficient actually is function of length, as can be seen in Figure 5.10(b), showing the CC value for (6,6) SWCNT of various lengths L.

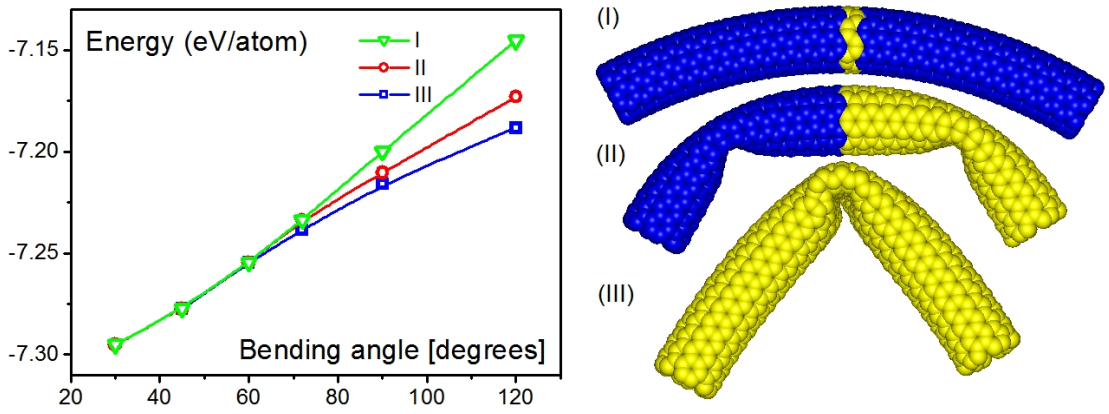

FIGURE 5.11: Bending energy is plotted according to different bending modes at different bending angles. For the atomistic $(6, 6)$ SWCNT structures, the sections marked with yellow color are used in the simulation: single translational cell (I), 15 translational cells (II) and 30 translational cells (III).

The fitted function was obtained as:

$$a = 0.14(L - 0.253)^{-0.911}. \tag{5.4}$$

Another interesting aspect of buckling state is that there may be several harmonic modes [5] along the axis of SWCNTs. We here show how various harmonic modes can be studied. We have selected a (6,6) SWCNT with a translational cell of length of $\sim$ 8 nm. Supercell bending calculations were performed and various bending instabilities appeared under the same bending conditions during the simulations carried out at various lengths. In Figure 5.11 the computational cells are again shown in yellow. The unbuckled state shown in (I) was obtained when a single translational cell where buckling cannot be acomodated. The buckling mode with two kinks (II) was simulated by using 15 translational cells while the buckling mode with single kink (III) emerged in a simulated using 30 translational cells. As can be seen in Figure 5.11, the buckling states are initialed at $\sim 60°$. In the energy aspect, the non-buckled state has the highest energy while the two buckled mode presents a lower energy. In agreement with continuum theory predictions, the single kink mode corresponds to the fundamental mode and has the lowest energy.

Chapter 6

Hexagonal Nanotube Structures as Screw Dislocations.

As discussed in Chapter 2, a stress free carbon nanotube can be described by a minimal two atom repeating domain with "helical-angular representation". When the repeating rule is modified from *translation* to *translation* + *rotation*, symmetry-adapted MD enables the economical computational costs in computing the elastic constants. However, this minimal two atom domain forbids structural relaxation beyond linearity. As discussed in Chapter 4, to study the nonlinear mechanical response of carbon nanotubes under external deformations, larger domains were employed. The feature of the nonlinear elasticity – buckling – was then obtained. Nevertheless, for the purpose to study the plasticity, what is the best choice of the repeating domain then?

6.1 Screw-Dislocation Construction of Hexagonal Nanotubes

Symmetry-adapted MD represents a generalization of the widely used MD under periodic boundary conditions (PBC). In PBC MD, the solution satisfies the specified translational invariance of a CNT. In symmetry-adapted MD, the helical

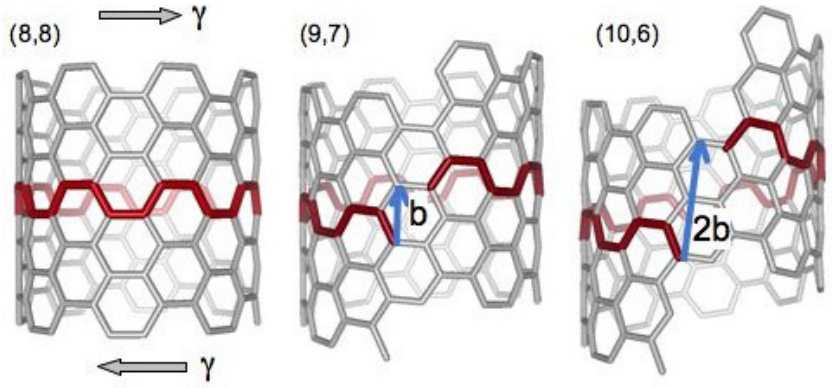

FIGURE 6.1: Symmetry-adated MD cells shown in red (dark), for $(8,8)$, $(9,7)$, and $(10,6)$ CNTs, all contain 32 atoms. Screw vectors $\mathbf{b}$ and $2\mathbf{b}$ specify the glide steps. Horizontal arrows show the right-handed applied-twist.

symmetry of a CNT is no longer concealed and the solution is invariant to the specified screw (translation and rotation) group operations of a CNT.

Figure 6.1 (left) shows a (n,n) CNT formed by rolling-up a carbon ribbon with zig-zag edges. The infinitely long tubule can be mathematically generated by repeated axial translations with Burgers vector $\mathbf{b_3} = \mathbf{a_1} - \mathbf{a_2}$ applied to the atoms located in the translational ring below. Figure 6.1(center) shows a $(n+1, n-1)$ NT obtained by rolling-up the same ribbon, followed by an additional axial glide with $\mathbf{b_3}$. This glide creates an axial screw dislocation with respect to the armchair NT, with Burgers vector $i\mathbf{b_3}$, where i is an integer. The glide induces a torque that produces an atomic-scale Eshelby's twist, and formation of a $(n+i,n-i)$ chiral pattern. For example, a $(10,6)$ CNT (Figure 6.1 (right)) is obtained with glide $2\mathbf{b}$.

In symmetry-adapted MD, we describe a chiral $(n+i, n-i)$ NT from the same N atoms belonging to the translational cell of the (n,n) hexagonal NT. Let $\mathbf{X}_j$ be their atomic positions after axial glide with $i\mathbf{b_3}$. This collection of N atoms stands for the new symmetry-adapted MD cell. Positions $\mathbf{X}_{j,\zeta}$ of the atoms located in the repeating cell replica indexed by integer ζ are obtained with

$$\mathbf{X}_{j,\zeta} = \mathbf{R}^{\zeta}\mathbf{X}_j + \zeta\mathbf{b}, \quad j = 1, ..., N. \tag{6.1}$$

Axial vector $\mathbf{b}$ combined with rotational matrix $\mathbf{R}$ of angle θ characterize the helical transformation. These structural parameters are analogous to the lattice

vectors in PBC MD.

Again, the major advantage of symmetry-adapted MD is that it treats on the same footing chirality and torsional deformations and thus can model chiral CNTs under *arbitrary* torsional distortion from relatively small repeating domains. By contrast, the widely-used PBC MD requires large translational cells or supercells, and describes only discrete torsional deformations, compatible with the assumed translational symmetry. The introduced simplifications in the number of atoms allows us to apply an accurate, quantum-mechanical treatment of the chemical binding [115].

6.2 Dislocation Onset and Glide in Carbon Nanotubes under Torsion

With this new repeating domain, we show that the plastic property – glide – can be also conveniently dealt with by symmetry-adapted MD. Despite the well known near circumferential glide in carbon nanotubes under tension deformation, we found that a near-axial glide can be achieved in nanotubes with hexagonal wall under torsion.

Our motivation of this work is invoked by the recent experiments on superplasticity [129, 130] where CNTs can undergo large elongation and thinning without abandoning their perfection and also the theoretical studies [131–133] indicating that superplasticity relies on primary microscopic mechanisms, like a mass-conserving glide along nearly-circumferential helical paths, as well as on a nearely-axial pseudoclimb, with dimers directly breaking out of the lattice. Remarkably, each mass-conserving glide step lowers the CNT's diameter and changes its index from (n,m) to (n,m-1) or (n-1,m). Plasticity under bending [134, 135] was also described in terms of the kink motion along the nearly-circumferential paths.

Indeed, the remarkable physical properties of CNTs originate in their objective atomic structure [39], where each carbon atom sees precisely the same environment up to rotation and translation. Modulating these properties is highly desirable for various applications and systematic ways to manipulate the perfect arrangement

of hexagonal rings are needed. Due to the strong carbon-carbon covalent bonding, inducing such structural changes requires high temperature and/or irradiation conditions. A wealth of experimental data [136] shows that the near-sublimation thermal agitation does not necessarily destroy CNTs. Instead, it can have a benefic effect, especially when combining the significant random agitation of the atoms with a coherent component caused by an externally-applied deformation.

Then, a logic question would be raised: Besides the near circumferential glide under tension, what other primary transformations can be induced by external deformation on the hot CNT lattice? To address this question we considered CNT's plasticity under another fundamental type of deformation – torsion. The popular atomistic modeling tools are unsuitable for modeling this deformation. We describe the CNT's torsional response with symmetry-adapted molecular dynamics (MD) and predict the possibility of a mass-conserving nearly-axial glide. We first indicate by direct calculation the susceptibility of twisted (n,m) CNTs to glide along this path. Next, we show that the practical realization does not necessitate any preexisting defects and it can be triggered by the nucleation of a 5-7-7-5 dislocation dipole. Once nucleated, the 5-7 kinks glide away from each other, leaving behind an (n+1,m-1) CNT.

6.2.1 Nearly Axial Glide Path in Carbon Nanotubes under Torsion

We now start to identify the slip path befitting single-walled CNTs under right-handed twist. It is convenient to represent the CNT's translational, rotational, and helical symmetry with vectors in the unrolled representation projected onto a graphene sheet. Screw vectors describe helical symmetry and have components along translational and circumferential vectors. The three Burgers vectors of graphene [130] indicate three non-equivalent helical slip paths for CNTs. We will show with direct symmetry-adapted MD calculations that the path indicated by the screw Burgers vector $\mathbf{b}$ with the smallest component in the circumferential direction [34] is desirable under twist. For right-handed CNTs, $\mathbf{b} = \mathbf{a}_1 - \mathbf{a}_2$, where $\mathbf{a}_1$ and $\mathbf{a}_2$ are graphene's lattice vectors. It is easy to see that a slip step achieved by a global network motion has the effect of changing the (n,m) CNT's circumference

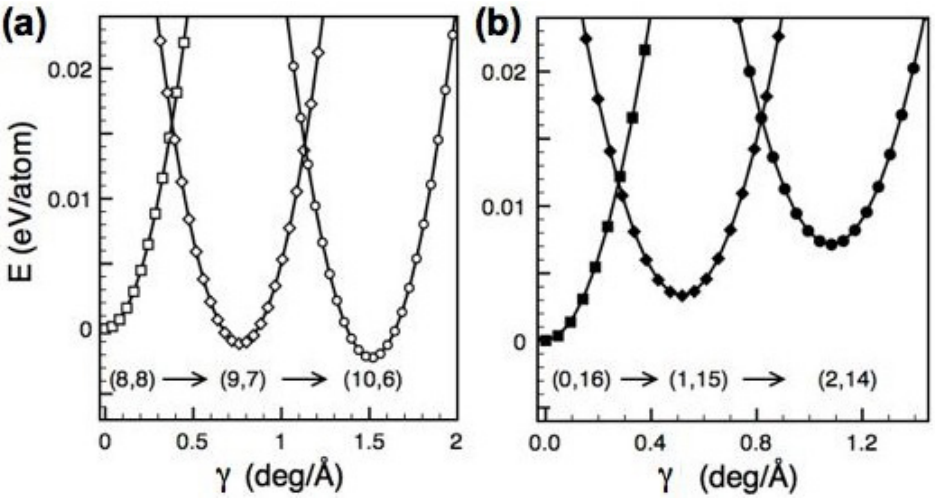

FIGURE 6.2: Strain energy versus the applied-twist rate, starting from (a) armchair and (b) zig-zag CNTs. The energy minima corresponds to the undeformed CNTs of indexes indicated below each curve.

vector from $\mathbf{C} = n\mathbf{a}_1 + m\mathbf{a}_2$ to $\mathbf{C}' = \mathbf{C} + \mathbf{b} = (n+1)\mathbf{a}_1 + (m-1)\mathbf{a}_2$, and thus leading to an (n+1,m-1) CNT. For example, starting from the (8,8) CNT, Figure 6.1, glide with $\mathbf{b}$ and $2\mathbf{b}$, leads to (9,7) and (10,6) CNTs, respectively. The (8,8) CNT of Figure 6.1 is described from the 32-atom translational domain, shown with red (dark gray). Thus, in eq. (6.1) $\mathbf{R}$ is the identity matrix ($\theta_0 = 0$) and index i runs over the atoms located in the translational domain of periodicity $\mathbf{T}$. Once the stress-free configuration was identified through conjugate gradient potential energy scans under different $|\mathbf{T}|$ values, a torsional strain rate $\gamma = (\theta - \theta_0)/|\mathbf{T}|$ was imposed by increasing the screw angle θ. The procedure was repeated for the (9,7) and (10,6) CNTs, both described from the 32-atom domain altered by $\mathbf{b}$ and $2\mathbf{b}$ glide steps, respectively.

The obtained strain energy (measured with respect to the energy of the (8,8) CNT) versus γ is presented in Figure 6.2. Starting from left, one sees the expected quadratic increase in the energetics of the (8,8) CNT. Beyond a 0.4 deg/Å twist rate the armchair structure becomes unfavorable against the reversely-twisted (9,7) CNT. As γ is further increased, the (9,7) CNT's strain energy decreases until the stress-free state is reached, beyond which this CNT is forwardly-twisted. Eventually (9,7) CNT looses its advantage to the (10,6) CNT and so on until the zig-zag (16,0) CNT is obtained after $8\mathbf{b}$ (not shown). The similar calculations presented in Fig. 1(c) started from the zig-zag case show that the vertical

glide introduces a change in handedness. The (16,0) CNT was represented as a (0,16) CNT from a 32-atom domain with a -8**b** slip and $\theta_0 = -11.25^o$, which is the new reference value for measuring γ. Under applied twist the (1,15) CNT (-7**b** glide left-handed) becomes quickly favorable, followed by (2,14) CNT (-6**b** glide, left-handed) and so on, until (8,8) CNT is regained.

6.2.2 The Onset of Dislocations in Carbon Nanotubes under Torsion

The next logical step is to investigate the realization of the glide through discrete dislocation motion rather than by the unlikely coherent motion of the graphene strip edges past one another. It is natural to conjecture the nucleation of a primary Stone-Wales (SW) defect with two 5-7 dislocation cores of $\pm$**b** Burgers vector. The importance of the SW defect in CNT's plasticity under tension and bending is well recognized [128, 134, 135, 137] but its role under torsion was not revealed.

In a pristine CNT, the SW defect forms via a 90^0 bond flip. The encountered energy barrier is high [128, 137] and the transformation requires high temperatures or irradiation. Notably, the SW defect structure will slightly elongate along the direction given by the pentagons. In the tubular geometry, the SW transformation of a non-circumferential or a non-axial bond, locally twists and lengthens the CNT. If the CNT is under torsion, a properly-oriented defect can relive strain and eventually make the SW defected state energetically favorable over the pristine one. For example the calculations presented in Figure **??**(a) show the energy dependence on the twist rate for the perfect and SW-defected (16,0) CNT. The minimum of the SW curve gives the twists rate $\gamma_{SW} = 0.17$ eV/Å and formation energy $E_{SW} = 4.0$ eV. The intersection of the two curves gives the critical twist rate $\gamma^* = 0.72$ eV/Å above which the defected state becomes energetically favorable.

We now focus on the χ-dependence of the plasticity onset. Generally, in a chiral CNT there are three sets of non-equivalent bonds, labeled 1, 2, and 3 in Figure **??**(b), that make distinct angles β with respect to the CNT axis. Depending on the bond to undergo the SW transformation, there are three possible non-equivalent defect orientations. Given an applied twist handedness, the most likely

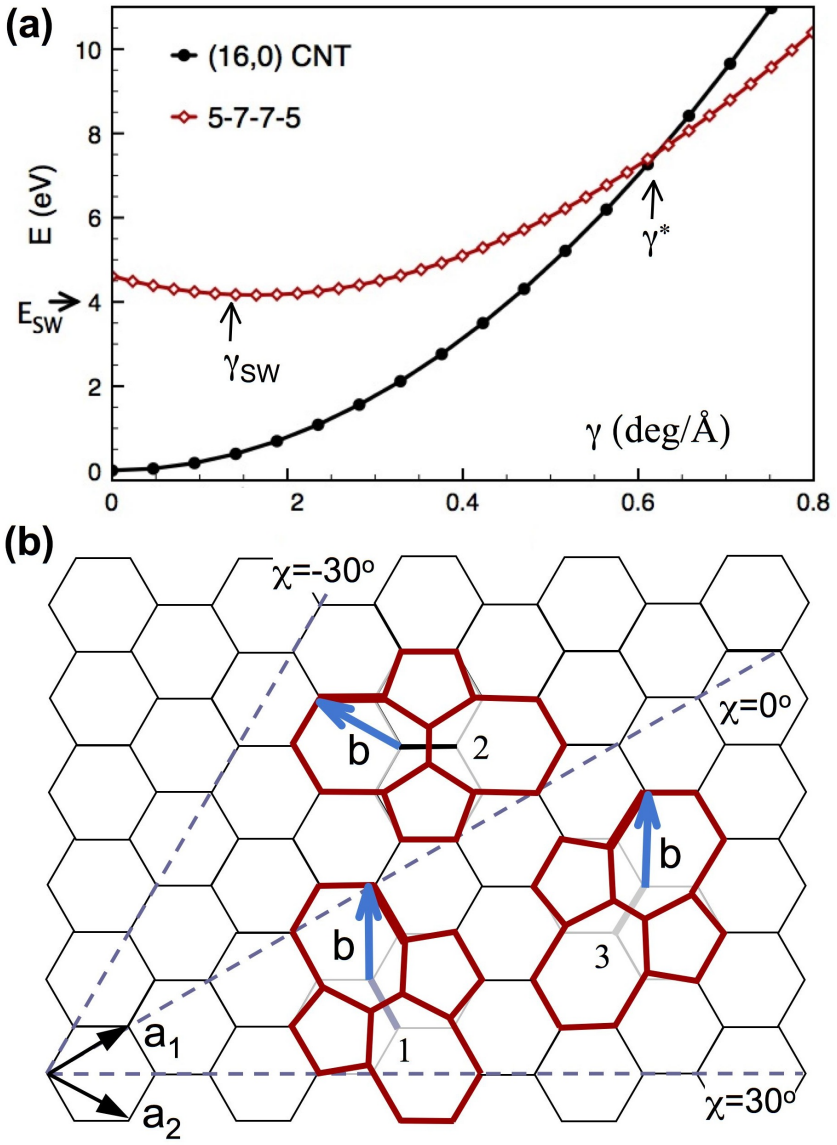

FIGURE 6.3: (a) Energy versus applied-twist rate for a perfect and SW defected $(16, 0)$ CNT. The simulation cell contains 128 atoms and it is derived from the translational cell of an $(8, 8)$ CNT via $8\mathbf{b}$ glide steps. (b) Schematics of the non-equivalent 5-7-7-5 dislocation dipoles formed by 90^0 rotation of the three non-equivalent bonds, labeled 1, 2, and 3. In (a), bond 2 underwent the SW transformation. Under twist, a 5-7 core can glide along the Burgers screw vectors $\mathbf{b}$, shown in blue (light gray), via a 90^0 rotation of the adjacent "shoulder" bond. Chirality is measured by the angle χ made by its projected circumference with graphene's lattice vector $\mathbf{a_1}$. Thus, dashed lines indicate the armchair ($\chi = \pm 30^0$) and zig-zag ($\chi = 0^0$) directions.

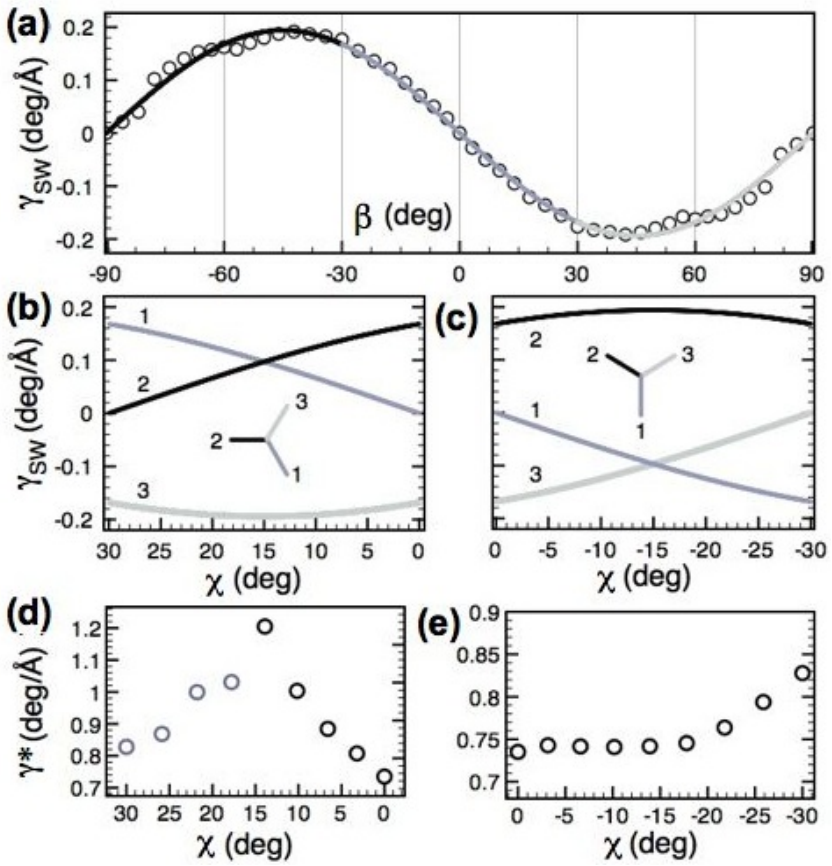

FIGURE 6.4: (a) The twist rate γ_{SW} introduced by the SW transformation of a bond that initially makes an angle β with respect to the CNT axis. Calculations (open circles) were carried out on the [(8,8), (9,7), ..., (16,0)] CNT family described from 128-atom repeating domains. The continuous line is the fitting to lowest order in β. The reduced-zone representation, i.e., γ_{SW} as a function of chirality, in (b) right- and (c) left-handed CNTs. The three branches 1, 2, and 3, correspond to the three distinct bonds in a CNT, shown in the schematics in the armchair and zig-zag orientations. Plasticity onset as a function of chirality in (d) right- and (c) left-handed CNTs.

bond to flip is the one that produces the largest γ_{SW} and thus the smallest γ^*. In order to quantify γ_{SW} and then determine [138] γ^*, we have carried out a series of SW calculations for a series of nearly-equal 5.8 Å in radius CNTs: (8,8), (9,7),..., (15,1), and (16,0), all described with the 128-atom translational supercell of the (8,8) CNT, as altered by the 0, **b**, ..., 8**b** glide steps, respectively. Calculations obtained $E_{SW} = 4.04 \pm 0.5$ eV and a distinct β-dependence for γ_{SW}, as evidenced by Figure 6.4(a). Fitting this atomistic data, to the lowest order in β we have $\gamma_{SW}/[\text{deg/Å}] = -0.19 \cdot sin(2\beta)$.

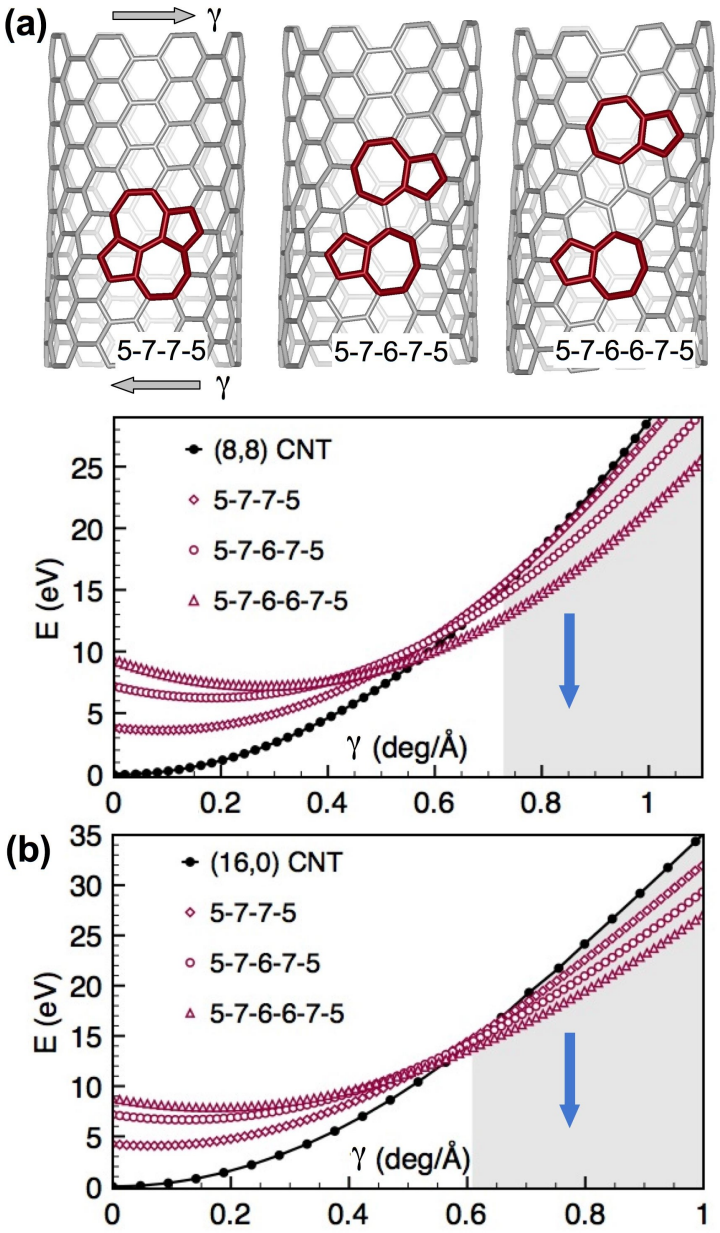

FIGURE 6.5: (a) Splitting of the 5-7-7-5 defect with axial glide of the 5-7 kink, in an (8,8) CNT under torsion. The first (7-7-6-7-5) and second (5-7-6-6-7-5) glide step configurations are next shown. (b) Energy versus applied twist rate for the pristine, SW defected, first, and second glide steps. Shaded area indicates the strain range where all defected CNTs become energetically favorable over the pristine one. The down arrow indicates the possibility of glide through the lower energetic states towards the (9,7) CNT.

More understanding can be gained by examining the added "reduced-zone" plots, that present γ_{SW} introduced by the three distinct sets of bonds in a CNT of chirality χ. As χ varies from armchair to zig-zag in right-handed CNTs, Figure 6.4(b), our data shows that at $\chi = 15^{\circ}$ the bond most prone to the SW flip changes from 1 to 2. When going from zig-zag to armchair (left-handed CNTs indicated by negative χ), Figure 6.4(c), only bond 2 can be flipped by applied twist. Note that the bonds identified here do not generally coincide with the ones prone to flip under external elongation [137]. The obtained χ-dependence for the onset of plastic deformation is correlated with the pronounced angular dependence of γ_{SW}. For right-handed CNTs, Figure 6.4(d), the γ^* dependence indicates that the thermodynamic conditions for plastic yield are met latest at $\chi \sim 15^0$ where a crossover-cusp dependence is noted due to the change on the most favorable bond choice. For left-handed CNTs, Figure 6.4(e), the dependence is smooth and bounded by the 0.7-0.85 deg/Å interval.

Once nucleated, the 5-7-7-5 defect splits into two 5-7 cores via a succession of 90^0 bond flips [132]. Notably, under applied twist the SW defect splits in a distinct way, such that the 5-7 core moves along the (n,m) CNT along the Burgers vector directions indicated in Figure 6.5(b), to leave behind an (n+1,m-1) CNT region. We demonstrate the initial stages of glide by direct calculations carried out on a (8,8) CNT described with a supercell containing 256 atoms. Figure 4 shows the the topology of the SW defect obtained by the rotation of bond 1, followed by the two initial stages of the glide process, as well as the energy dependence with the applied twist rate for these configurations. Several important features can be noted. All curves appear to have similar curvatures but their minimum points are shifted towards higher strain rate values, from 0 deg/Å for (8,8) CNT to 0.3 deg/Å for the second glide step. Additionally, the formation energy of the second glide step didn't increase much compared to the first. As a result, the configurations with more glide steps are intersecting the pristine (8,8) CNT curve earlier than the ones with fewer. By the time crossover of the SW curve with the pristine one occurs at 0.73 deg/Å, all following glide states would be lower in energy and the (8,8) CNT's lattice can slide down through a series of glide steps towards the energetically preferred (9,7) CNT.

6.3 Intrinsic Twist in MoS_2 Nanotubes

New findings often come with new viewpoints. Adopting the screw-dislocation NT construction view with symmetry-adapted MD, we find out a large collection of MoS_2 NTs are of lacking the standard translational symmetry. Thus, the usual roll-up construction needs to be amended: while the circumference vector is being rolled, the translation vector should turn into a helix. Deriving the parameters for this helix is complex and requires both the ability to describe the nonlinear microscopic response of the MoS_2 to rolling and an accurate description of the interatomic interactions.

It is likely that many other NTs have a locked twist, including very small diameter CNTs. With symmetry-adapted MD relying on the helical symmetry of the Eshelby's twist [139], the structure, properties and dynamical behavior for other chiral nanostructures, including lead sulphide [140] and lead selenide [141] nanowires grown via a screw dislocation mechanism, polymers and certain biomolecules can be also studied conveniently. Here we showed that helical MoS_2 NTs have intrinsic twist, and χ-dependent fundamental band-gaps and elastic responses. Although of practical interest [142], the elastic torsional response of MoS_2 NTs was not studied extensively until now due to the incompatibility of PBC with this type of deformation. The knowledge of the band-gap and elastic-constant variations with χ opens the possibility to design new NT-pedal [142] electromechanical devices and experiments using MoS_2 NT components.

Having the hexagonal wall lattice, the atomistic structure of MoS_2 nanotubes can be described as a screw dislocation similarly as in carbon nanotubes. Figure 6.6(a) (left) shows a (n, n) NT formed by rolling-up a MoS_2 ribbon with zig-zag Mo and S edges. The infinitely long tubule can be mathematically generated by repeated axial translations with Burgers vector $\mathbf{b_3} = \mathbf{a_1} - \mathbf{a_2}$ applied to the atoms located in the translational ring below. Figure 6.6(a)(right) shows a $(n + 1, n - 1)$ NT obtained by rolling-up the same ribbon, followed by an additional axial glide with $\mathbf{b_3}$. This glide creates an axial screw dislocation with respect to the armchair NT, with Burgers vector $i\mathbf{b_3}$, where i is an integer. The glide induces a torque that produces an atomic-scale Eshelby's twist, and formation of a $(n + i,n - i)$ chiral pattern.

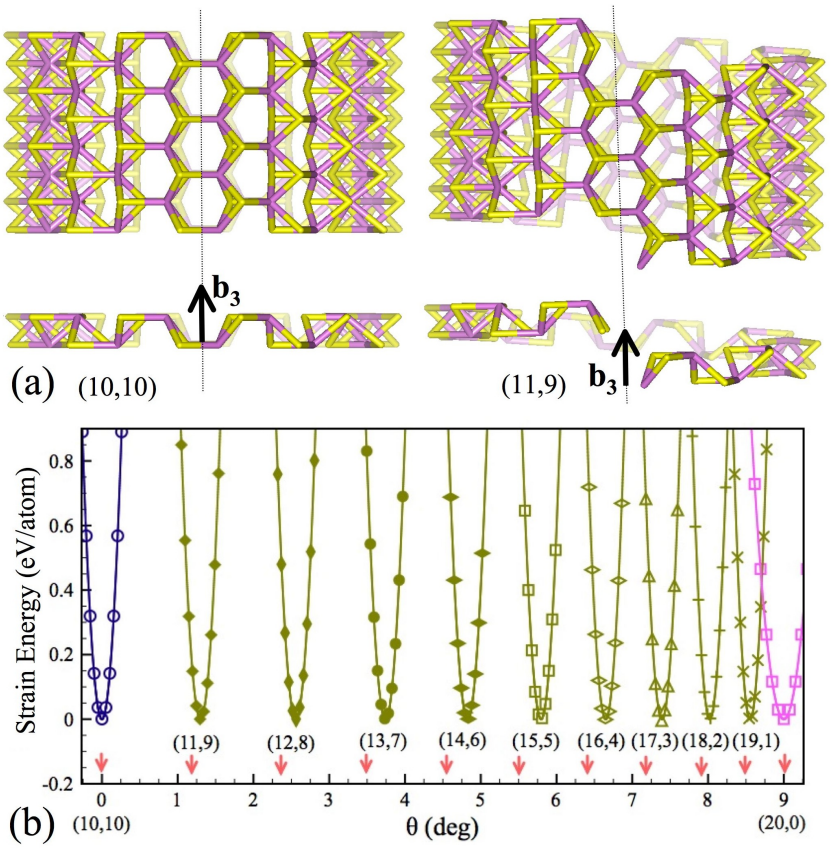

FIGURE 6.6: (a) Symmetry-adapted computational cells (below) for (10,10) (left) and (11,9) (right) MoS_2 NTs. The NT structures (above) were obtained by the helical replication of the symmetry-adapted MD cells along vector $\mathbf{b_3}$. (b) Strain energy vs. θ for the (10,10) ... (20,0) NT family with nearly-equal diameters. The energy minima correspond to the stress-free NTs of indexes indicated under each curve.

We have performed calculations on five families ($n = 10, 14, 16, 18$) generated by introducing axial screw dislocations in (n,n) NT structures. Additionally, a large collection of armchair and zig-zag NTs of $1 - 9$ nm diameter was considered. The initial structural information for a (n,m) NT is adopted from the rolled MoS_2 layer, for which the free parameters of eq. (6.1) can be obtained with the simple expressions $|\mathbf{b_0}| = \sqrt{3}a(n+m)/2\sqrt{n^2+nm+m^2}$ and $\theta_0 = \pi(n-m)/(n^2+nm+m^2)$. Parameter $a = 3.27$ Å is the length of the primitive vectors of the flat layer. Additionally, the radius of this tubule writes [38] $R_0 = |\mathbf{C_0}|/2\pi = a\sqrt{n^2+nm+m^2}/2\pi$. The stress-free atomic positions and the Eshelby's twist parameters ($|\mathbf{b}_E|$ and θ_E) are identified by applying a symmetry-adapted modeling procedure, symmetry-adapted MD within conjugate gradient minimization of the total potential energy.

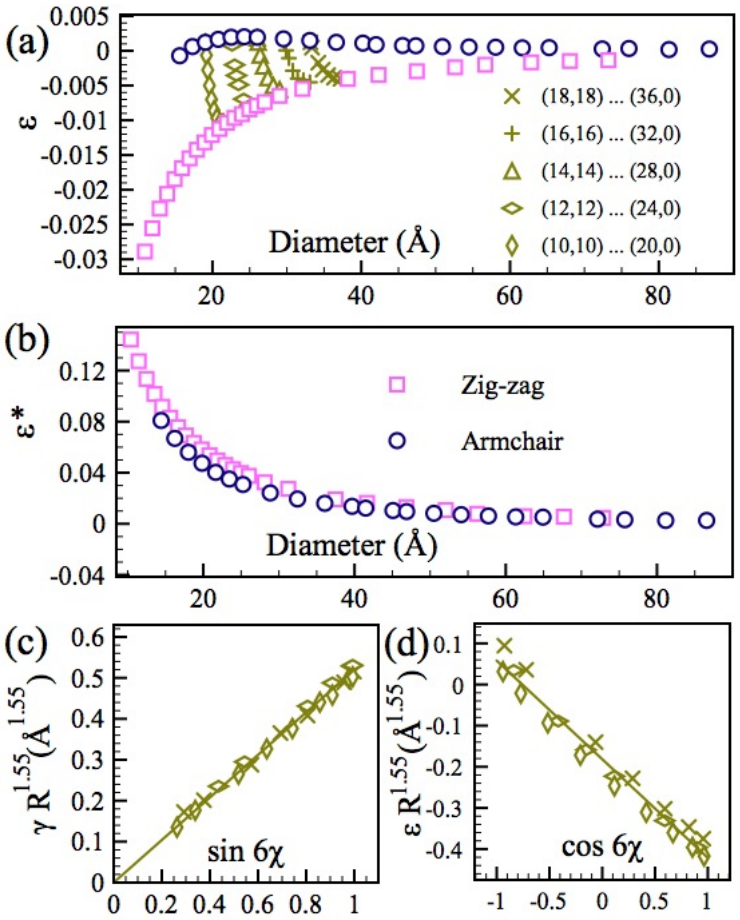

FIGURE 6.7: Scaling of the intrinsic (a) axial (ε), (b) radial (ε^*) strains with NT diameter. (c) Torsional shear strain and (d) axial strain (both multiplied by $R^{1.55}$) for the chiral MoS_2 NTs, as obtained from the DFTB model.

Most unusually, we find that for a large catalog of NTs the structural parameter predictions given by the roll-up are not adequate. This is exemplified in Figure 6.6(b) for the $(10, 10)...(20, 0)$ NT family. Indeed, axial relaxation under fixed angle θ_0 only is not sufficient, and further angular relaxation in the vicinity of relaxed $|\mathbf{b}_E|$ lowers the energy. The angle values of the stress-free chiral structures θ_E deviate from the predicted θ_0 indicated by down arrows. Thus, the chiral NTs possess an intrinsic twist with respect to roll-up configuration.

6.3.1 Nonlinear Mechanical Response of MoS_2 Monolayer to Rolling

More insight into the structural parameters of stress-free NTs is obtained by analyzing the variations shown in Figure 6.7(a) and (b). The axial prestrain $\varepsilon = (|\mathbf{b}_E| - |\mathbf{b_0}|)/|\mathbf{b_0}|$ and the radial prestrain $\varepsilon^* = (R - R_0)/R_0$ are essentially zero in the large diameter region. No intrinsic twist was found at these diameters and we conclude that pure roll-up is achieved for diameters larger than ~ 7 nm. At lower diameters however, the behavior is nonlinear. The rolling of the MoS_2 layer couples both with the in-plane strain and the rolling curvature. Figure 6.7(a) shows that while armchair NTs slightly elongate with increasing curvature, the zig-zag ones shrink. As a result, in chiral NTs the axial prestrain values are spread between these two curves. Concurrently, NTs undergo a decompression with respect to the rolled-up configuration, Figure 6.7(b), with practically no chirality dependence.

For a compact characterization, we combined simple symmetry arguments with the extensive numerical computations and derived simple functional forms for all prestrains. Ignoring the small chirality effect, the radial prestrain can be described by a simple fitting of the atomistic data, as $\varepsilon^* = 5.4(R/\mathring{A})^{-1.55}$. We further assume the same radial scaling for the other prestrains. At constant R, the developed anisotropy between special armchair and zig-zag directions implies that both ε^* and the shear prestrain $\gamma = (\theta_E - \theta_0)R/|\mathbf{b}_E|$, must have a 60^o period in their chirality angle dependence. Fig. 2(c) and (d) both show a nearly linear dependence of γ and ε (both $R^{1.55}$ augmented) to the symmetry-allowed lowest-order in chiral angle χ. Thus, to a good approximation $\gamma = 0.52(R/\mathring{A})^{-1.55} sin6\chi$ and $\varepsilon = -(R/\mathring{A})^{-1.55}(0.18 + 0.24 cos6\chi)$.

To summarize, a (n,m) NT obtained by pure rolling has translational symmetry, with $T_0 = \sqrt{3}|\mathbf{C_0}|/d$, where d is the greatest common divisor of $2n + m$ and $2m + n$ [34]. However, the nonlinear roll-up effect introduces an intrinsic twist. For example, a $(14, 6)$ MoS_2 NT locks a 0.87 deg/nm twist rate. How can we describe the atomic order in the chiral NTs without the translation property? Our comprehensive investigation of the fully relaxed structures found that the helical invariance is present to the extent that the NT structures can be described

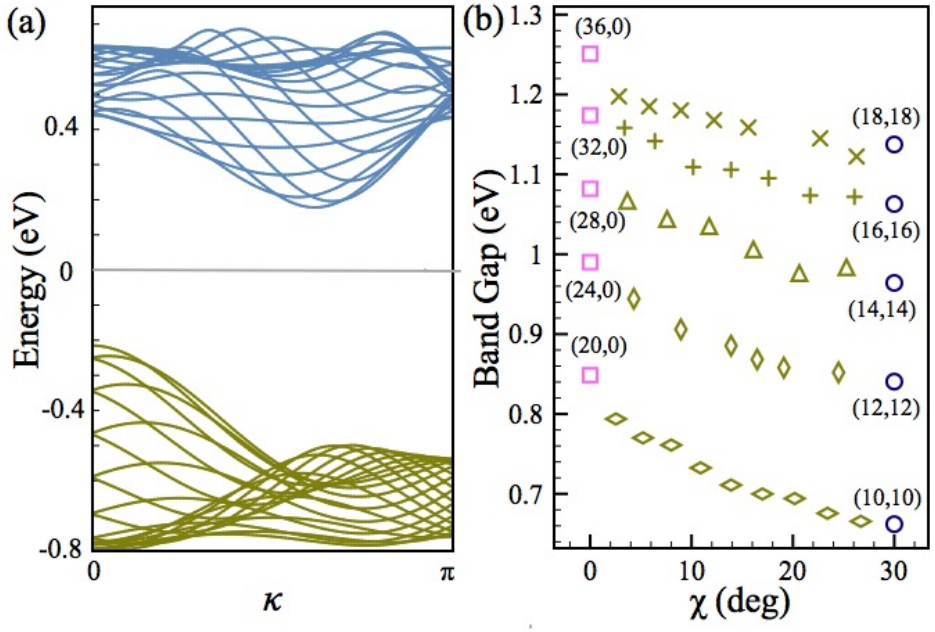

FIGURE 6.8: (a) Band structure for a (19,1) MoS_2 NT. The Fermi level, located at zero, is marked by a horizontal line. The horizontal axis represents the helical quantum numbers. (b) Calculated band-gap energies as a function of chirality.

by applying successive commuting helical transformations to the MoS_2 molecule, as

$$\mathbf{X}_{j,(\zeta,\zeta')} = \mathbf{R}'^{\zeta}(\mathbf{R}^{\zeta}\mathbf{X}_j + \zeta\mathbf{b}) + \zeta'\mathbf{T}, \quad j = 1, 2, 3. \tag{6.2}$$

Of course, the structural parameters for the old helical operator are $|\mathbf{b}_E|$ and θ_E. The new helical transformation is characterized by a translation $T = T_0(1 + \varepsilon)$ and an axial rotation matrix $\mathbf{R}'$ of angle $\theta' = \gamma T$. Note that, if γ is vanishingly small, eq. (6.2) becomes the translational-helical representation [34]. The helical polymers [143] generated with (6.2), regardless of the positions of the atoms in the molecule, belong to the larger class of recently defined objective molecular structures [39]. Informally, in an objective molecular structure corresponding atoms in different molecules see exactly the same environment up to orthogonal transformation (translation and rotation).

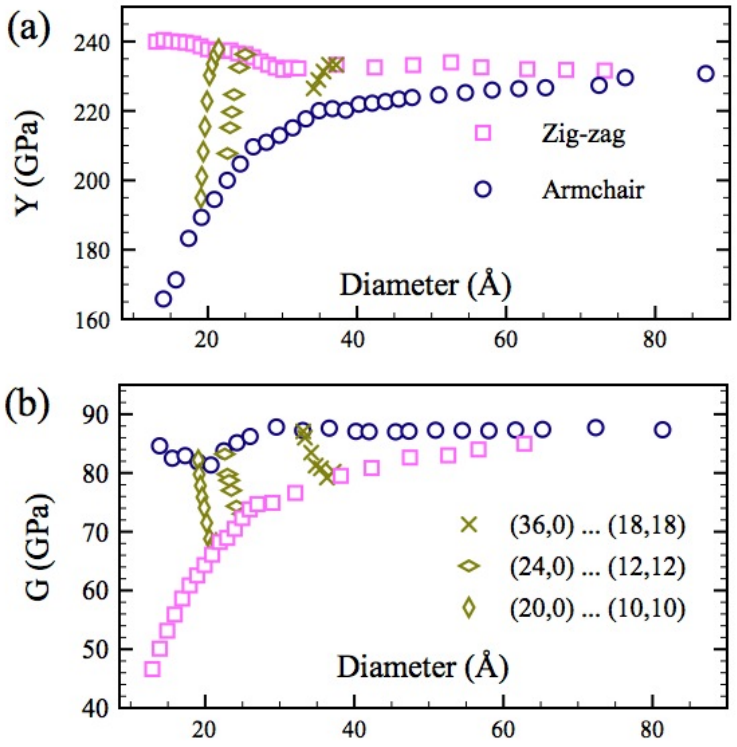

FIGURE 6.9: (a) Young's and (b) shear modulus vs. NT diameter. The wall thickness was taken to be 6.15 Å.

6.3.2 Chirality- and Size-Dependence of MoS_2 NTs Properties

The helical symmetry introduced by the Eshelby's twist combined with symmetry-adapted MD is a suitable framework to study the chiral MoS_2 NTs. For example, in PBC calculations the common way to analyze the electronic energy is by plotting the electronic bands as a function of the linear momentum. Analogously, in symmetry-adapted MD calculations electronic states are plotted as a function of the helical quantum number k, as exemplified in Figure 6.8(a) for the tight-binding states of a $(19, 1)$ NT. Our analysis found that all computed chiral NTs have indirect band-gaps. Within the same family, band-gap decreases smoothly with increasing χ, Figure 6.8(b). The chirality dependence is pronounced at smaller diameters.

If the structural parameters $|\mathbf{b}_E|$ and θ_E are varied around their optimized values, the NT's property of being an objective molecular structure is retained but helical

strain states are introduced [143]. Using this strategy we studied pure tensile and torsional deformations [144] within the adiabatic approximation, i.e. when forces on atoms are derived from the electronic ground state at each strain configuration. Evaluation of the elastic constants was then accomplished with simple second-order polynomial fits to the ground-state energy's dependence on strain.

When the nonlinear elasticity under rolling-up arises, this should alter the isotropic elastic behavior of the MoS_2 NTs. Indeed, for diameters under ~ 7 nm there is a discernible diameter- and chirality-dependent anisotropy in the elastic response, as can be seen in the obtained Young's Y and shear G elastic constants displayed in Figure 6.8. Microscopically, this originates in the significant distortion of the hexagonal lattice symmetry, as quantified by the ε, ε^*, and γ prestrains. The similarity between the elastic quantities of NTs and the flat MoS_2 layer holds only at diameters larger than ~ 7 nm, consistent with the prestrain analysis. In this region, typical values $Y = 230$ GPa, $G = 88$ GPa, and Poisson ratio $\nu = 0.3$ (obtained from the isotropic elasticity relation $G = Y/2(1 + \nu)$), and bending rigidity $D = 34.4$ eV/molecule (obtained from the strain energy of NTs) compare favorably with experiment [145], demonstrating the reliability of the employed treatment.

Chapter 7

Electromechanical Characterization of Carbon Nanotubes in Torsion via Symmetry-Adapted Molecular Dynamics.

Besides mechanical properties, carbon nanotubes also exhibits exceptional tunable-by-strain electronic properties under fundamental types of deformations. Indeed, it is now possible to perform conductivity measurements in CNT-pedal devices which employ CNTs as torsional springs [8, 103, 146]. Since experimental uncertainties are numerous, the atomistic simulation find an opportunity in such area. As we developed the capability of symmetry-adapted molecular dynamics, the complex morphology of deformed nanostructures can be economically modeled with a small repeating domain, the accurate quantum mechanical computation becomes affordable, where the electrons are explicitly accounted for.

As discussed in Chapter 5, under external deformations SWCNTs are susceptible to rippling. It is interesting to point out that such rippling gives rise to a new morphology of carbon nanostructures with helicoidal furrows and ridges. Due to the complex morphology, the electromechanical response of CNTs under rippling

cannot be computed with traditional methods. In spite of this complex morphology, we will show that the electromechanical response in rippled carbon nanotubes can be related the known electronic properties of flat graphene. Hence, we start this chapter by reviewing the electronic properties of idealized cylindrical carbon nanotubes under torsion, as derived directly from flat graphene.

7.1 Electronic Response of Idealized Carbon Nanotubes under Torsion

From a mechanical viewpoint, rolling of the isotropically-elastic graphene into a SWCNT is practically linear [147], i.e. it does not couple with other deformations such as twisting, as noted in MoS_2 NTs [148]. Curvature hardly affects the electronic states and the elastic [144] and electronic [34] properties can be understood from those of flat graphene. For example, the electronic bands of a SWCNT of radius R are equispaced $1/R$ sub-bands, labeled by the angular quantum number l, in graphene's band structure. For a (n, n) SWNT, $l = 0, ..., n-1$ and $\mathbf{k_F}$, the Fermi momentum of graphene, is located on the $l = 0$ sub-band. Notably, the changes imposed on the electronic states by a homogeneous deformation can still be derived from the flat graphene picture. A CNT's response to torsion is described by the Yang and Han (YH) nonperturbative model [149], formulated in terms of π-orbitals. Use the flat graphene representation, the hamiltonian of torsional deformed carbon nanotube can be easily obtained. Refer to Figure 2.1, the minimal repeating cell contains two carbon atoms, denoting two sub-lattice. Each of them has three nearest neighboring atoms. According to Bloch theory discussed in Chapter 3, the hamiltonian reads:

$$H = \begin{pmatrix} 0 & \sum_\zeta t_\zeta f_\zeta(k_a, k_c) \\ \sum_\zeta t_\zeta f_\zeta^*(k_a, k_c) & 0 \end{pmatrix}. \tag{7.1}$$

where, the sum runs over the three nearest neighbors of the referred carbon atom.

k_t and k_c are wavevector components in axial and circumferential directions, respectively. $f_\zeta(k_a, k_c)$ is the relative Bloch phase. Parameter t_ζ is the hopping energy varying according to Harrison relation: $t_\zeta = t_0 r_\zeta^2 / r_0^2$. Apparently, a quadratic energy dispersion is obtained as:

$$E^2 = |\sum_\zeta t_\zeta f_\zeta(k_a, k_c)|^2 \tag{7.2}$$

We note that although the axial component of wavevector k_a is continuous, the circumferential component is discrete. In our notation, k_c, associated the rotational symmetry of carbon nantubes, is replaced with an integer number l named as angular quantum number. Therefore, in the language of symmetry-adapted MD, the key features of Yang-Han π-orbital model are summarized as follows: When applying a torsional rate Γ, the wall of an ideal SWCNT experiences a homogeneous shear strain ΓR. The l sub-bands remain invariant under torsion. In a (n, n) SWNT torsion shifts the location of $\mathbf{k_F}$ in the circumferential direction by $\Delta k_F = \Gamma R / d_{C-C}$, where d_{C-C} is the equilibrium C-C bond length. Due to the linearity of the dispersion relation near $\mathbf{k_F}$, the band gap variation of a SWCNT is proportional to Δk_F. When $\Delta k_F = 1/R$, $\mathbf{k_F}$ reaches the $l = 1$ sub-band and the band gap of the twisted tube vanishes. The band-gap is maximum at the midpoint between these two sub-bands.

7.1.1 Demonstration of Yang-Han π-orbital Model via Symmetry-Adapted Molecular Dynamics

Efforts have also been made to obtain the driven-by-strain band gap. In one *ab* initio calculation [150], the improper boundary conditions where the atoms the edge was chosen to apply the external torsion. Due to the effect of edge, the band gap varies quite randomly. Thus it can not verify the Yang-Han prediction perfectly. Turning to symmetry-adapted MD, since arbitrary *pure* twist rate can be applied, the relation of band gap to the twist can be conveniently obtained. The first ever simulated band gap vs. twist rate γ is posted at Figure 7.2.

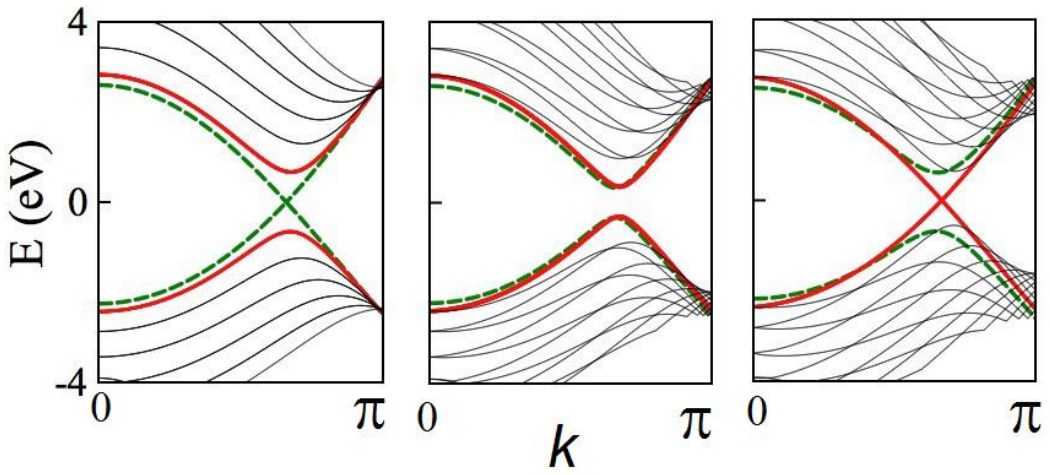

FIGURE 7.1: Electronic bands dispersion in (12,12) CNT, for two shapes and several γ values: (a) idealized strain-free (left), under 5 deg/nm (middle), and 10.5 deg/nm (right). Thick dashed (green) and continuous (red) bands have l of 0 and 1, respectively.

As we see, the band gap is periodically modulated. During one period $\Delta\gamma$, it grows in a linear fashion, reaches a maximum at halfway, then decreases to zero. These features are in agreement with predictions of Yang and Han [149] developed from the band structure of graphene: Uniformly twisted CNTs are metallic only when the metallic wavefunction of graphene is commensurated with the CNT's circumference. Otherwise they are semiconducting. Due to the linearity of the dispersion relation of graphene near its Fermi level, band gap varies in a linear fashion with a $3t_0R$ slope. R is the CNT's radius and t_0 is the TB hopping element. It also follows [149] that $\Delta\gamma = d_{C-C}/R^2$, where d_{C-C} is the C-C bond length. Fitting to our data gives $t_0 = 2.72$ eV and $d_{C-C} = 1.42$ Å, in agreement with the actual values of these parameters.

Next, it is instructive to identify the twist-related changes in the electronic band structure, Figure 7.1. In the strain-free case, the metallic character is due to the intersection of the non-degenerate $l = 0$ valence and conduction bands. Note that most bands in the strain-free structure appear double degenerate due to symmetry. Twisting the idealized cylinder SWCNT removes degeneracies, opens a fundamental direct gap between $l = 0$ valence and conduction and decreases the gap between $l = 1$ valence and conduction. Beyond 5.5 deg/nm, the gap is still

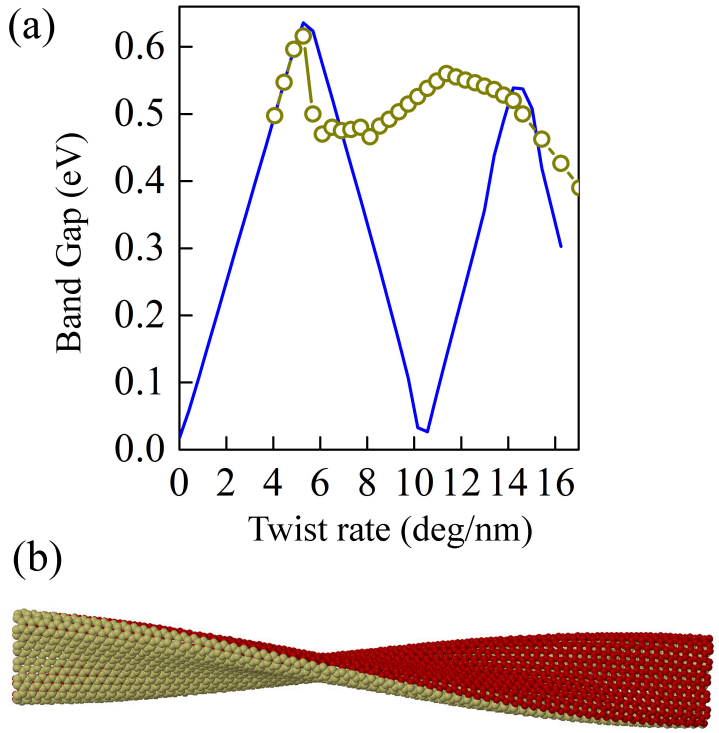

FIGURE 7.2: (a) Band gap vs. twist rate γ for cylinder idealized shape (solid blue line) and two-lobe rippling mode (open circle). The two-lobe rippling mode can be seen in (b): a side view of rippled (12,12) SWCNT under twist rate $\gamma = 10$ deg/nm.

direct and given by the $l = 1$ bands. The metallic character is regained when $l = 1$ bands intersect.

7.2 Electromechanical Response of Rippled Carbon Nanotubes under Torsion via Symmetry-Adapted Molecular Dynamics

However, from the discussion in Chapter 4, SWCNTs are susceptible to ripple under torsion, especially when the diameter is large. When accounting for rippling the band gap for all modes undergoes major changes, which are distinct form the idealized predictions. Focusing on the two-lobe mode in Figure 7.2(b), we note that in the transient mechanical stage (Figure 7.2(a)) band gap departs only

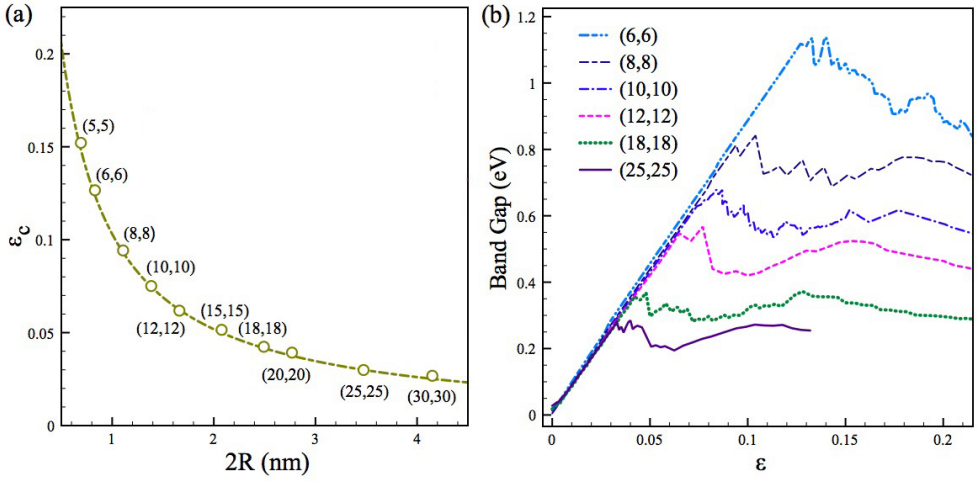

FIGURE 7.3: (a) Critical shear strain vs. CNT's diameter for SW armchair CNTs. (b) Changes in the band gap with the shear strain for armchair SWCNTs.

slightly from the idealized model. Immediately after bifurcation, when the formation of ridges is initiated, the band gap exhibits a small decrease. The sudden onset of inhomogeneous strain manifested in the creation of furrows is reflected in a ~ 0.15 eV band gap drop. Note that in this process the minimum distance between furrows drops from 10.3 Å to 6 Å, not enough to cause electronic coupling. Next, as rippling becomes pronounced and the distance between furrows decreases rapidly, reaching ~ 3.4 Å at 7.2^0/nm, the band gap maintains a constant value. This indicates that the now present electronic coupling between faces and the inhomogeneous strain effect cancel each other.

In the second mechanical stage of rippling, the idealized model of the band-gap variations is not applicable, even though the band gap is still related to the twist.

The generality of the above behavior is demonstrated in Figure 7.3, summarizing results from a series of similar calculations performed on armchair CNTs. During torsion the ideal CNT wall experiences a shear strain $\varepsilon = \gamma R$. Figure 7.3(a) plots the obtained critical shear ε_c, which exhibits a scaling $\varepsilon_c = 0.1([nm]/2R)^{0.99}$ qualitatively inconsistent the $\sim R^{-3/2}$ dependence [151] obtained with atomistic simulations using classical potentials and different boundary conditions. Figure 7.3(b) reveals the band gap dependence with ε. In agreement with the idealized model, the linear regime data collapses onto a common line with a $3t_0$ slope. However, beyond ε_c, the idealized model based on the homogeneous strain assumption cannot

be used.

7.3 Gapping by Effective Shear Strain in Rippled Carbon Nanotubes

Our symmetry-adapted MD data revealed the complexity of rippled carbon nanotubes. One can also conclude that the Yang-Han model constructed from the homogeneous torsional deformation in carbon nanotubes can not explain such results. Rippling represents a way of lowering energy by creating an inhomogeneous torsional strain coupled with the development of helicoidal ridges and furrows of positive and negative curvature, respectively. Recent experiment findings indicate that rippling is a popular phenomenon of hollow nanotube structures [152–155].

When rippling happens, the modification of electronic structures comes of several possibilities. In one class of experiments, it was found that small band-gaps (less than $\sim$ 100 meV) open under mechanical lateral squeezing of metallic CNTs. This behavior is attributed to the bilayer-coupling that arises between the two sides of the flattened tube [156]. The $\sigma - \pi$ orbital mixing due to the creation of inhomogenous curvature is secondary but it is suggested to become important under severe squeezing [157]. The consequences of the complex helical rippling that arises during mechanical manipulation, i.e, the locked twist state of a collapsed CNT [152, 155], are not yet understood. It is suggested that the observed changes in the electronic states [155] originate in the same bilayer-coupling and $\sigma - \pi$ orbital mixing effects.

Using perturbation theory and symmetry-adapted molecular dynamics, here we show that an intralayer effect and not the known bilayer-coupling and $\sigma - \pi$ orbital mixing dominate the gapping of metallic tubes. Relying on the new concept of the *effective* strain experienced by the CNT wall, the electromechanical response of rippled CNTs can be still related to the behavior of flat graphene. We first consider isolated SWCNTs and uncover the dominant role played by the inhomogenous helical strain present in the rippled wall, an effect that was not considered before. A developed π-orbital perturbative treatment defines an effective shear

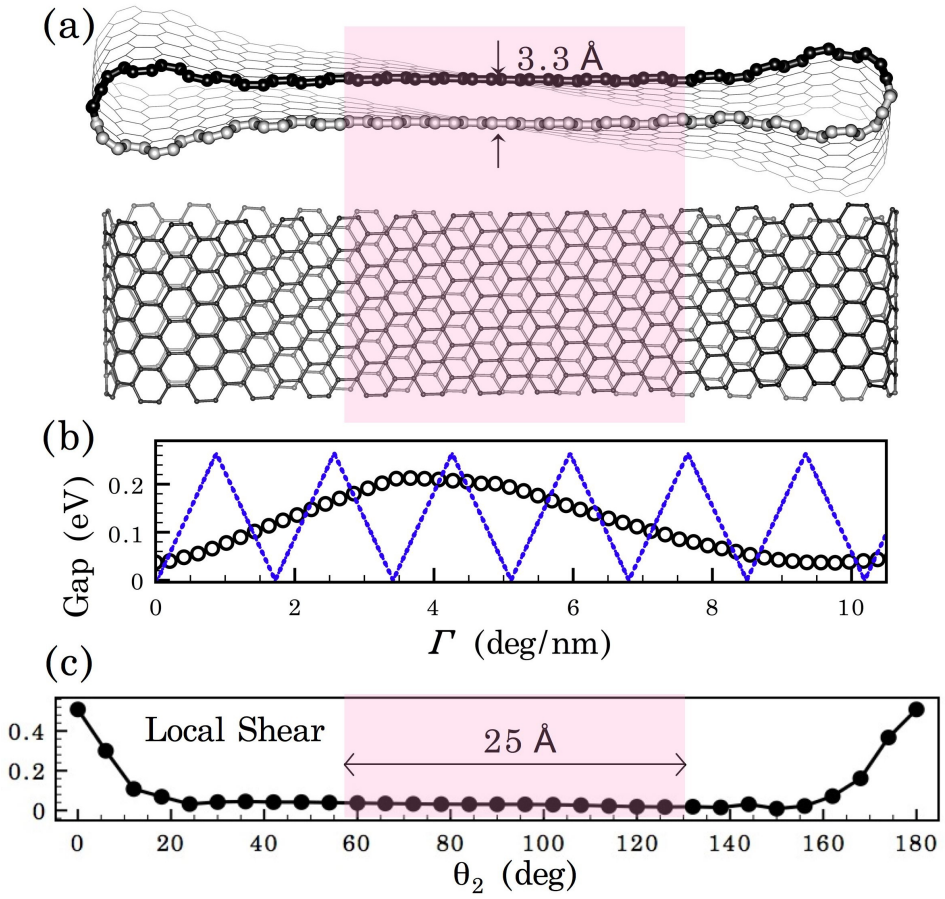

FIGURE 7.4: (a) Cross section (top) and side (bottom) views of a two-lobe rippled (30,30) SWCNT under 10.7^0/nm twist, as computed with DFTB symmetry-adapted MD. (b) Band-gap vs. the applied twist rate for the rippled state (circles). The ideal YH behavior (dotted) is shown for a comparison. (c) Circumferential distribution of the averaged shear strain on atom A. Shading indicates the region at the furrows stacked in a Bernal pattern.

strain under which the intra-wall band-gap variations follow the YH recurrent behavior of the ideal state in spite of the morphological change. These predictions are confirmed by symmetry-adapted MD calculations performed on a four-orbital symmetry-adapted [115] DFTB basis. Next, we simulate the consequences of the gradual presence of interior walls and give a clear mechanical interpretation of the effective strain. The observed differences between the applied strain and the effective strain has experimental implications. It suggests that some caution should be taken when using the YH model to interpret the conductivity measurements carried out in CNT-pedal devices when SWCNTs and MWCNTs with large diameter and small number of walls are employed.

7.3.1 Development of a Degenerate Perturbative π-orbital Model

Consider a $(30, 30)$ SWCNT. Such a large-radius tube is very susceptible to rippling [158] and exhibits large hysteresis in twisting-untwisting cycles with stable and metastable rippling states. In fact, this SWCNT remains locked in a squeezed shape upon complete untwisting. We first focus on the bilayer-coupling. Figure 7.4(a) suggests that rippling has electronic effects since a large portion of the contact within the van der Waals interaction distance stacks in a Bernal lattice pattern. For more insight, we model the bilayer coupling with degenerate perturbation theory in the framework of simple π-orbital tight-binding (TB). Only two quantities are essential: t, the intra-layer hopping between the A and B sublattices, and γ, the inter-layer coupling between the AA sites [159]. A (n,n) SWCNT is obtained from a two-atom AB cell under repeated N helical and n azimuthal operations [144], indexed by ζ_1 and ζ_2, respectively. The electronic bands $E_{l\kappa}$, labeled also by the helical quantum number $-\pi \leq \kappa < \pi$, are represented in terms of two symmetry-adapted Bloch sums [158]

$$|j, l\kappa\rangle = \frac{1}{\sqrt{nN}} \sum_{\zeta_1=0}^{N-1} e^{i\kappa\zeta_1} \big(|j, \zeta_1\rangle + e^{il\pi} |j, \zeta_1\rangle' \big), \quad j = A, B. \tag{7.3}$$

Here $|j, \zeta_1\rangle$ and $|j, \zeta_1\rangle'$ are partial sums $\sum_{\zeta_2} e^{il\theta_2\zeta_2} |j, \zeta_1\zeta_2\rangle$, with angular index ζ_2 limited over the upper and lower circumferential half, respectively. $|j, \zeta_1\zeta_2\rangle$ is the symmetry-adapted π orbital on the atom j of the ζ_1 and ζ_2 site, and $\theta_2 = 2\pi/n$. The interaction of the furrows at the κ points corresponding to the metallic state, couples strongly the valence and conduction bands with same l via the Hamiltonian

$$H_l = \begin{pmatrix} \gamma cos\pi l & \sum_\zeta t f_\zeta(l, \kappa) \\ \sum_\zeta t f_\zeta^*(l, \kappa) & 0 \end{pmatrix}. \tag{7.4}$$

The lower diagonal element is zero as the nonessential $B - B$ inter-layer coupling effect is being ommited. Index ζ runs over the three intra-layer nearest-neighbor atoms and $f_\zeta(l, \kappa)$ is the difference in Bloch factors. The bilayer-coupling results in the quadratic dispersion

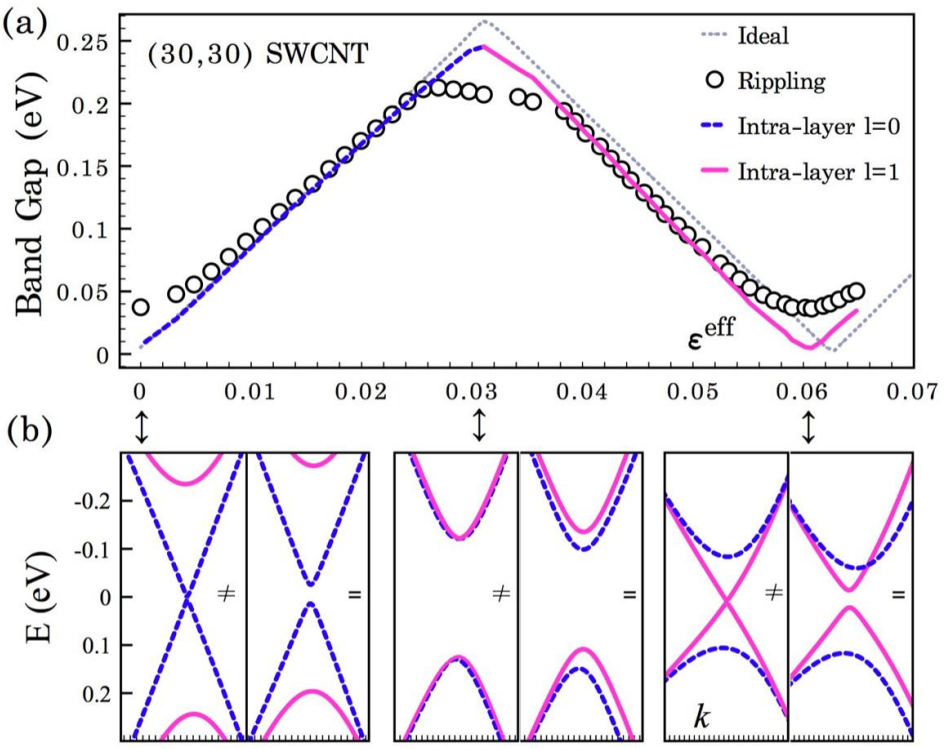

FIGURE 7.5: (a) Band-gap for a (30,30) SWCNT – ideal (dotted) and two-lobe ripping (circles) – vs. the effective shear strain. The intralayer contribution is shown for a comparison. (b) Closeups of the two bands around the Fermi level (set to zero) for the two-lobe rippling mode, without ($\neq$) and with ($=$) bilayer-coupling, at three ε^{eff} values, 0 (left), 0.03 (middle), and 0.06 (right), also indicated by vertical double arrows. The dashed (continuous) lines are bands with $l = 0$ ($l = 1$).

$$\left(E_{l\kappa} - \frac{\gamma}{2} cos\pi l\right)^2 = \left(\frac{\gamma}{2} cos\pi l\right)^2 + |\sum_{\zeta} t f_{\zeta}(l,\kappa)|^2. \tag{7.5}$$

Interestingly, the rigid $\gamma/2$ shift in energy moves the energy bands with even (odd) l up (down).

Turning to Figure 7.4(b), one notes that the DFTB band gap variations don't follow the ideal YH recurrent behavior. However, the band-gap γ of ~ 40 meV for the squeezed (30,30) SWCNT ($\Gamma = 0$) is much smaller than the ~ 200 meV gap calculated for the rippled state at $\Gamma = 4$ deg/nm. Thus, this effect alone cannot explain our electromechanical data.

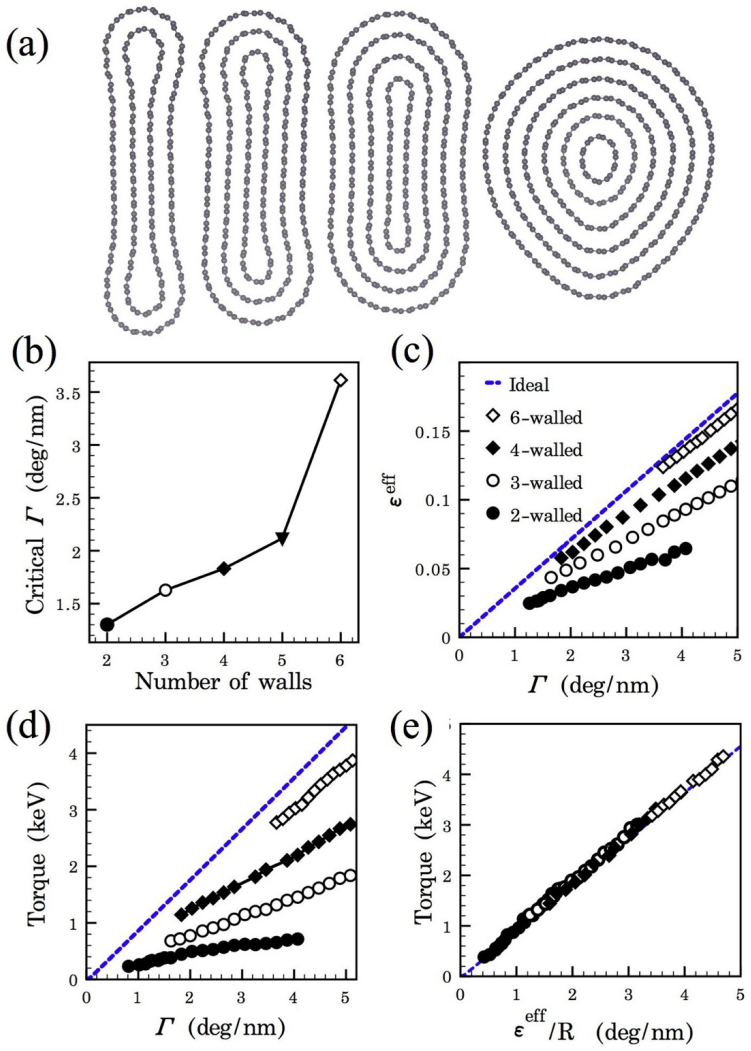

FIGURE 7.6: (a) Two-lobe rippling (cross-sectional view) in a MWCNT family with (30,30) SWCNT as the outermost wall. (b) Critical strain for rippling vs. the number of walls. (c) Effective strain in the outermost wall vs. applied twist rate. Torque in the outer wall (d) vs. twist rate and (e) vs. effective strain. Dashed line is the idealized case.

What is the origin of the large band-gap opening in rippled armchair SWCNTs? Rippling creates an inhomogeneous shear strain distribution, an effect that is not present in squeezed armchair CNTs. Thus, to answer this question we considered another possibility – gapping by shear strain. Figure 7.4(c) confirms the presence of local shear strain in typical two-lobe rippling. Turning back to Figure 7.4(c), one can distinguish around the circumference a low-strain nearly-homogeneous region located at the furrows and a narrow high-strain region at the ridges. This

distribution suggests a perturbative picture in which most of the SWCNT is under the influence of the averaged strain at the furrows ε^f and the unperturbed band-gap follows the YH behavior with a period d_{C-C}/R. We use the framework provided by the simple π-orbital TB and the Bloch sum basis (1) to account for the perturbation introduced by the averaged strain at the ridges ε^r. The effect of shear [73] is introduced in the off-diagonal elements of eq. (7.4) via the dependence of the hopping parameter on d_ζ, the bond length under shear, $t_\zeta \sim t(d_{C-C}/d_\zeta)^2$. If the perturbation acts alone, the eigenspectrum writes

$$\begin{aligned} E_{l\kappa}^2 &= |\sum_\zeta \left(t_\zeta(\varepsilon^f) + n_r[t_\zeta(\varepsilon^r) - t_\zeta(\varepsilon^f)]\right) f_\zeta(l,\kappa)|^2 \\ &\simeq |\sum_\zeta t_\zeta(\varepsilon^{eff}) f_\zeta(l,\kappa)|^2, \end{aligned} \tag{7.6}$$

where n_r is the fraction of A atoms at ridges and $\varepsilon^{eff} = \varepsilon^f + n_r(\varepsilon^r - \varepsilon^f)$. Thus, the intra-layer band-gap variations still follow the YH behavior but under an average strain ε^{eff}, interpreted as the *effective strain*. This effect could dominate gapping, as twist creates a band gap typically much larger than the bilayer-coupling one.

7.3.2 The Effective Shear Strain

We now confront these predictions with nonperturbative symmetry-adapted MD calculations of CNTs. When plotted against the ε^{eff} extracted from the DFTB data [160], the band-gap variations from the untwisting cycle display the YH behavior, Figure 7.5(a). This is because the response is dominated by the intra-layer contribution which shows ideal behavior, in agreement with eq. (7.6). Note that ε^{eff} has a nearly-linear dependence on Γ and equals ΓR for the ideal SWCNT. One concludes that the $\sigma - \pi$ mixing does not alter the band structure around the Fermi point.

Despite the decrease of inter-layer distance with increasing Γ (~ 3 $\mathring{A}$ at the largest Γ), the bilayer-coupling effect remains secondary. It is more visible at the cusp points of the YH variations: As detailed in the band structures of Figure 7.5(b), when the intra-layer band-gap vanishes, the coupling of the $l = 0$, Figure 7.5(b) left, and $l = 1$ bands, Figure 7.5(b) right, creates a direct band-gap predicted

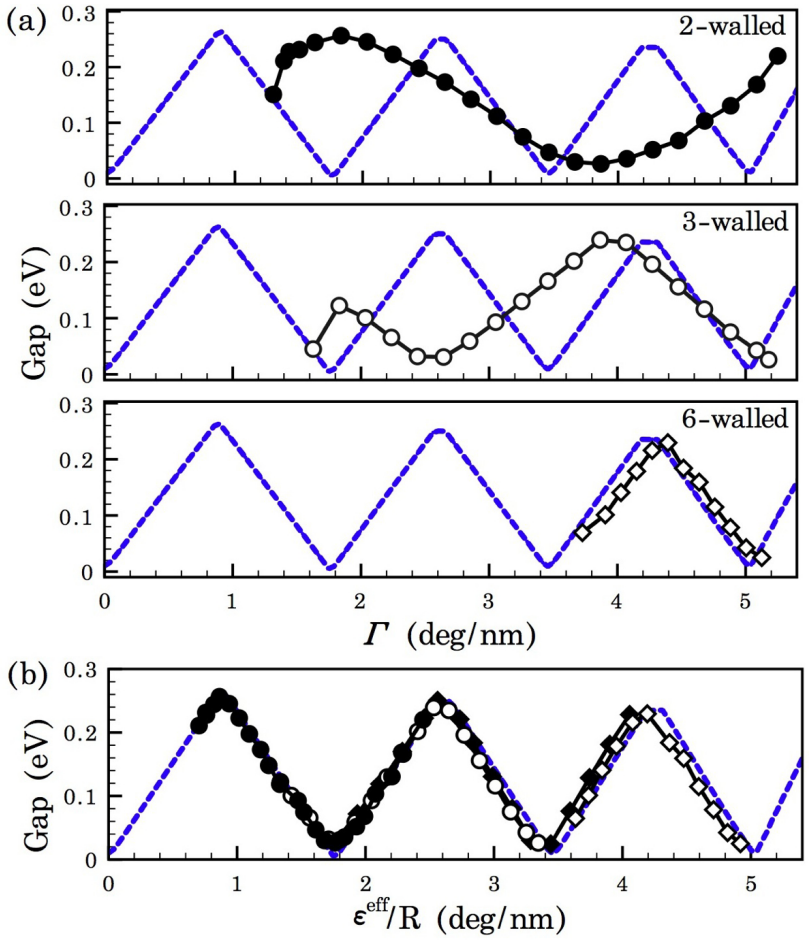

FIGURE 7.7: Band-gap in the rippled (30,30) outermost wall of a 2-, 3-, and 6-walled CNT vs. (a) the applied twist and (b) the effective strain. Dashed line is the idealized case.

by eq. (7.5). In the strain region around the central maximum, the intra-layer valence-conduction gaps of the $l = 0$ and $l = 1$ bands become comparable in size and are exactly equal at the cusp, Fig. 2(b) middle. The preferential $\gamma/2$ shift introduced by bilayer-coupling, irrelevant at other strain levels, now becomes important. By shifting the $l = 0$ ($l = 1$) bands downwards (upwards), it creates a lower, indirect band-gap.

MWCNTs also exhibit stable two-lobe rippling [158], Figure 7.6(a), and practically lack the hysteresis effect observed in SWCNTs. The critical torsional

strain marking the onset of rippling increases significantly as the core space of the $(30, 30)$ SWCNT is filled with concentric tubes, Figure 7.6(b). It is interesting to examine the effect of the inner walls on the ε^{eff} in the outermost wall, Figure 7.6(c). At a given Γ, the double-walled CNT has the lowest ε^{eff}. Rippling fades with the further addition of inner walls as the distinction between ε^{eff} and ΓR gradually washes out. In all cases ε^{eff} keeps a nearly-linear dependence on Γ.

Notably, the effective strain, derived earlier from the simple π-orbital model is also relevant in the mechanical domain, when σ bonding is significant. From the symmetry-adapted MD data, the rippling-induced changes in the elastic response of the outer wall can be obtained by studying the strain energy vs. Γ relation. For all the tested MWCNTs we find that the rippled outermost wall exhibits a nearly-linear elastic response with a reduced torsional constant when compared with the ideal state. This behavior can be clearly observed in the torque (energy derivative with Γ) vs. Γ plots of Figure 7.6(d), where the torsional constant represents the slope. Comparing Figure 7.6(c) and (d), one notes a striking correlation in how ε^{eff} and torque depend parametrically on the number of inner walls. It suggests that the apparent decrease in the torsional constant originates in the lower-than-ideal effective strain felt by the CNT wall. Indeed, when plotting the torque vs. ε^{eff} scaled by the CNT radius, Figure 7.6(e), data collapses onto the ideal behavior. This insight reveals that rippling lowers the strain energy by lowering the strain felt by the CNT wall, essentially without affecting the original sp^2 bonding of flat graphene.

Our findings bring a new perspective into the observed rippling-indiced electronic structure changes in collapsed CNTs [155]. In CNT-pedal experiments, ε^{eff} can be extracted from the measured torque-Γ relation. Our symmetry-adapted MD calculations presented in Figure 7.7 demonstrate that this knowledge is valuable in the electrical domain, for understanding the variations of the conductance oscillations: The inter-layer band-gap variations computed for the (30,30) outermost wall have various oscillation periods with Γ, Figure 7.7(a), depending on the number of inner walls. Only when $\varepsilon^{eff} \sim \Gamma R$, as in the closed core MWCNT case, the band-gap variations show overlap with the YH ideal behavior. However, all data collapses onto the ideal behavior when plotted against ε^{eff}, Figure 7.6(b), indicating the validity of the perturbative picture even under large torsion. Such

rescaling makes it possible to apply the simple YH model to any CNT. The effective strain concept and symmetry-adapted MD simulations can be applied to further our understanding of the electromechanical response of CNTs to other complex deformations, such as rippling under bending [161], and of other nanoscale forms of carbon, such as the twisted nanoribbons [162, 163] discussed in Chapter 8.

Chapter 8

Electromechanical Characterization of Graphene Nanoribbons in Torsion via Symmetry-Adapted Molecular Dynamics.

The newly discovered graphene nanoribbons (GNRs), the honeycombe atomic structures shaped into strips with nanometer-size widths, are mechanically robust and electrically conducting, and thus are well suited for use in nano nano-electromechanical systems (NEMS). The recent progress in preparation technologies [164, 165] and the demonstrated potential for use in NEMS [166], call for a rapid understanding of their electromechanical characteristics [167, 168]. At the same time, the vast knowledge gained so far about their seamless single-wall carbon nanotube (CNT) counterparts [8, 149, 158] viewed now as a paradigm nanomaterial, invites comparisons between the properties exhibited by the two nanostructures.

However, despite the scientific importance of graphene nanoribbons, little is known about their electronic structure other than in the ideal flat forms. In this chapter, we discuss the scaling rules for the band-gap of helical nanoribbons emerging from

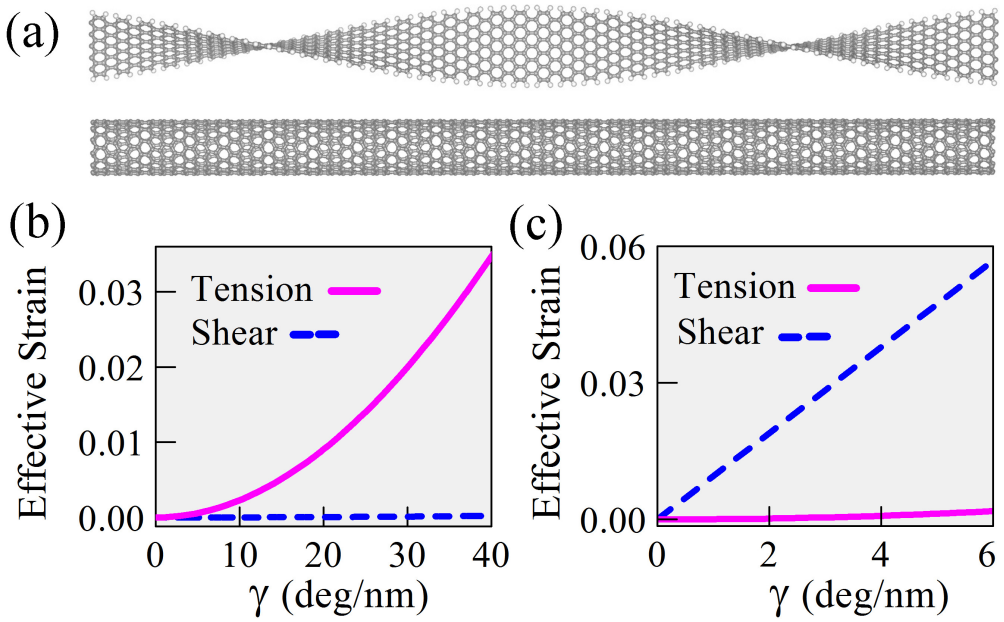

FIGURE 8.1: (a) Side view of 19 deg/nm twisted H-terminated 11 GNR with armchair edges and $(12, 0)$ CNT, as computed with symmetry-adapted MD. Effective shear and tension strain vs. twist rate for (b) 11 GNR and (c) $(12, 0)$ CNT.

torsional forces applied externally or internally by the edge chemistry in order to provide a critical atomistic mechanism for electromechanical response of GNRs under fundamental types of deformations. Helical atomistic structure created by torsion usually has inhomogeneous strain distribution.

To deal with these complex shapes, we rely on the concept of effective strain which was introduced when we were studying helically rippled carbon nanotubes. Indeed, in spite of the edge effects, the band-gap modulations in the effective strain rescaling appears strikingly similar with those encountered in carbon nanotubes. symmetry-adapted MD combined with density-functional-based tight-binding confirm these predictions and show that the effective strain enables links to the behavior of fractional carbon nanotubes.

8.1 Effective Tension Strain Induced by Twist in GNRs

We describe the response of H-terminated GNRs to various levels of twist using the technique of symmetry-adapted MD [38] coupled with symmetry-adapted density functional theory-based TB [40, 54, 147]. Because twisted GNRs typically have large translational periodicities, the usual translation-invariant quantum-mechanical (QM) microscopic formulation become computationally prohibitive. However, our computational method takes explicitly into account helical symmetry. This feature enables describing the interplay between the classical ionic and QM electronic degrees of freedom under an atomic-scale twist [144, 147, 148, 158] by considering only the atoms located in a primitive motif. We supplement the standard macroscopic elasticity concepts with an effective tensional strain ϵ^{eff} and develop a theory for the electronic states of GNRs under an arbitrary twist. ϵ^{eff} is a microscopically extracted quantity particularly useful for characterizing the strain stored in resilient one-layer-thin nanostructures. From the twisted GNRs morphologies we extract local tensional strains. On the basis of the analogy with the popular effective mass of electrons concept, we interpret the average over all atoms of these quantities as the effective tensional strain felt by electrons.

The utility of the effective strain concept first transpires from Figure 8.1, comparing a twisted H-terminated 11 GNR with a $(12, 0)$ CNT. Because of the similar orientation of the hexagonal atomic structure with the long axis, one may guess that these two nanostructures exhibit also a similar electromechanical response. However, Figure 8.1(b) and (c), reveals a sharp difference between the types of strains dominating the deformation of these two systems under the same γ: While in GNR, the honeycombed-shaped atomic structure is mostly in tension, the CNT's wall is mostly sheared. It is known that in zig-zag CNTs shear does not couple the conduction and valence bands [149]. However, the effective strain immediately reveals that a different microscopic mechanism operates inside GNRs and thus, band-gap variations could be expected.

New findings often come by using combinations of new investigation methods and

concepts. Due to the presence of two edges, the electronic behavior of GNR is ostensibly distinct from that of CNTs. Instead, we show that in the ϵ^{eff} rescaling of the deformation, twisted armchair GNRs exhibit band-gap variations similar with the ones encountered in axially elongated zig-zag CNTs. The ϵ^{eff} rescaling also helps delineate a pronounced Peierls effect in very narrow $N = 3p + 2$ GNRs. Symmetry-adapted MD simulations show that wider GNRs are susceptible to nonlinear-elastic rippling. Interestingly, the rippled GNRs assume the morphology of the recently synthesized fractional carbon nanotubes (FCNTs) [169, 170]. The role of the intra-wall strain in modulating the FCNT's band-gap is revealed here for the first time.

8.2 Electromechanical π-orbital Modeling Based on Effective Tension Strain

The presence of the two edges critically influences the GNRs' electronic properties. Consider the case of stress-free GNRs with H-saturated armchair edges. The GNR's width is commonly specified in literature in terms of the number of C-C dimer lines, N. *Ab initio* calculations predict a flat morphology in which the bonding characteristic changes abruptly at the edges, with atomic-scale compression in the 1 and N dimer lines [7]. The electronic character cannot be fully understood only by considering the quantum confinement effect in a simple $\pi-$orbital tight-binding (TB) [171] with hopping parameter $t_0 = 2.72$ eV. Indeed, the ideal model predicts N-dependent direct band gaps Δ_0 at the $k = 0$ wavevector given by $t_0|2-4cos(p\pi/N+1)|$, $t_0|2-4cos(p+1\pi/N+1)|$, and 0, for $N = 3p$, $3p+1$, and $3p + 2$ respectively. Here p is a positive integer. However, to obtain agreement with the *ab inito* calculated band-gaps, this ideal model needs to be enhanced by including the shrinking of the outermost dimers [7].

What is less commonly appreciated is that to predict the band-gaps in stress-free morphologies, the torsional response of GNRs is also needed. Indeed, if there is atomic-scale elongation at the edges, such as in the case of pristine [162, 163] and F saturated armchair edges, GNRs can give up on the two-dimensional planarity

and acquire an edge chemistry- and width-dependent intrinsic twist. This remarkably simple phenomenon can be exploited to establish new principles of design for objective nanostructures [39] with a high degree of control for the helical parameters. Because of the large translational periodicities, the objective molecular [38] description of such twisted GNR structure becomes fundamental. Informally, in an objective molecular structure corresponding atoms in different molecules see exactly the same environment up to orthogonal transformations (translation and rotation).

In symmetry-adapted MD, we describe the atomic locations $\mathbf{X}_{i,\zeta}$ of the twisted GNR with

$$\mathbf{X}_{i,\zeta} = \mathbf{R}^{\zeta}\mathbf{X}_i + \zeta\mathbf{T}. \tag{8.1}$$

Index i runs over the finite number of atoms located at positions $\mathbf{X}_i$ inside the primitive molecule motif. Index ζ labels the various identical molecules. Rotational matrix $\mathbf{R}$ of angle θ and the axial vector $\mathbf{T}$ characterize the discrete screw repetition rule applied to the molecule. Although the group operations indicated by eq. (1) are discrete, the shape of the twisted nanostructures computed with symmetry-adapted MD is nicely smooth, as confirmed by the morphologies depicted in Figure 8.2(a). It is interesting to note that unlike in the flat strip case, the distance between corresponding atoms in neighboring ζ cels varies along the GNR's width. Thus, twisted GNRs store an inhomogeneous tensional strain distribution, with the outermost dimer lines being the most stretched, Figure 8.2(b). Yet, the twisted structure can be described with only one unique axial length $|\mathbf{T}|$. We define the twist rate as $\gamma = \theta/|\mathbf{T}|$.

The electronic response to twisting can be predicted in the framework of simple π-orbital TB. For simplicity, our starting model is the widely-used idealized model [7], which at the important $k = 0$ position in the band structure is topologically equivalent with a two-leg ($u = 1, 2$) ladder system [7, 168] shown in Figure 8.2(c). The Hamiltonian writes

$$H_0 = -\sum_{n=1}^{N-1}\sum_{u=1}^{2}(t^{||}_{n,n+1}a^{\dagger}_{u,n}a_{u,n+1} + h.c.) - \sum_{n=1}^{N}(t^{\perp}_{n}a^{\dagger}_{1,n}a_{2,n} + h.c.) \tag{8.2}$$

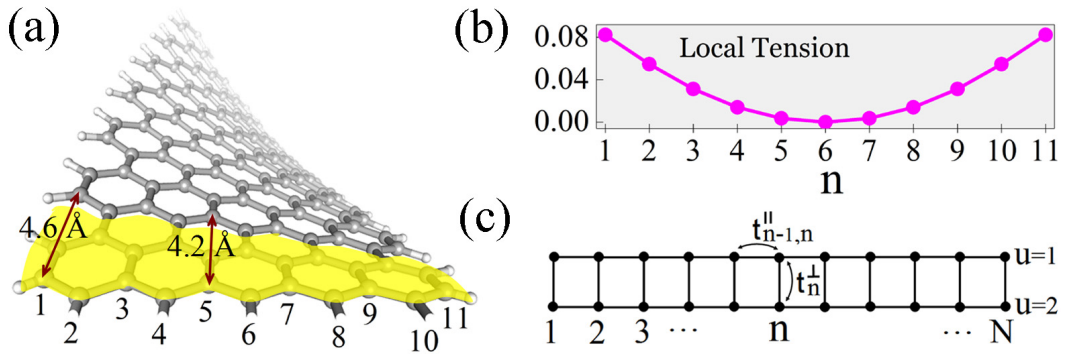

FIGURE 8.2: (a) Axial view of 19 deg/nm twisted H-terminated 11 GNR. The atoms located in the repeating molecule unit are shaded. The 11 C-C dimer lines are labeled. Along the directions delineated by the dimer lines, the distance between corresponding atoms in neighboring cells varies from 4.6 Å(outermost $n = 1$ line) to 4.2 Å(central $n = 5$ line). (b) Distribution of tensional strain along the dimer lines, as measured with respect to the stress-free GNR. (c) For the special $k = 0$ point, a two-leg ladder with N rungs is topologically equivalent to armchair N GNR [7].

where $a^{\dagger}_{u,n}$ ($a_{u,n}$) is the creation (annihilation) operator at the dimer site n and leg u. By assuming $t^{||}_{n,n+1} = t^{\perp}_{n} \equiv t_0$, the analytical eigenvectors write:

$$|\psi_l\rangle = (|\chi_l\rangle, |\chi_l\rangle)^{\dagger} \tag{8.3}$$

where $|\chi_l\rangle = \left(sin\frac{l\pi}{N+1}, sin\frac{2l\pi}{N+1}, ..., sin\frac{Nl\pi}{N+1}\right)^{\dagger}$.

Usually, the effect of edges is included in the above model or a third-neighbour one in a perturbative manner by accounting only for the length variations of the C-C bonds along the dimer lines [7]. However, applying the same procedure to capture the distinct mechanical effect of twisting turns out to be less satisfactory. Instead, we account for the inhomogeneous tensional strain along the dimer lines, via the induced changes in the two hopping strengths $t^{\perp}$ and $t^{||}$. Keeping only the linear corrections to the atomic displacements from their ideal positions, these changes write [168] $\delta t^{\perp}_{n} = 2t_0\epsilon_n$ and $\delta t^{||}_{n} = t_0(1 - 3\nu\bar{\epsilon}_n)$. Here ϵ_n in the tensional strain in dimer n, $\bar{\epsilon}_n = (\epsilon_n + \epsilon_{n+1})/2$, and $\nu = 0.26$ is the Poisson ratio [50]. Degenerate perturbation theory with respect to the intrinsic states of the ideal GNR gives a

correction to the band-gap Δ_0 as

$$\begin{aligned}|\delta\Delta| &= 4t_0\left(\epsilon^{eff} - \frac{1}{N+1}\sum_{n=1}^{N+1}\epsilon_n cos\frac{2n\alpha\pi}{N+1}\right)\\ &+ 2t_0(1-3\nu)\left(\epsilon^{eff} - \frac{1}{N+1}\sum_{n=0}^{N}\bar{\epsilon}_n cos\frac{(2n+1)\alpha\pi}{N+1}\right)cos\frac{\alpha\pi}{N+1}\\ &\approx t_0\left(4 - 2(1-3\nu)cos\frac{\beta\pi}{N+1}\right)\epsilon_{eff}.\end{aligned} \tag{8.4}$$

The last approximation is accurate at large N. The quantities ϵ_{N+1}, $\bar{\epsilon}_0$, and $\bar{\epsilon}_N$ all take the $-\epsilon^{eff}$ value. Index β takes the value p when $N = 3p$, and $p+1$ otherwise. Index α equals $N - \beta$. As defined earlier,

$$\epsilon^{eff} = (1/N)\sum_{n=1}^{N}\epsilon_n \tag{8.5}$$

The last result in eq. (8.4) can be further simplified by noticing that $cos(\beta\pi/N+1)$ $= 0.5$ when $N = 3p+2$ and ≈ 0.5 otherwise. Therefore, we obtain that for all GNR types, twisting leads to a linear variation of the HOMO-LUMO gap vs. ϵ^{eff} with a $3(1+\nu)t_0 = 10.3$ eV slope [172]. Thus, we predict that to describe the dominant contribution to the band-gap variations, only the average ϵ^{eff} of the detailed inhomogeneous tensional strain distribution is needed. Interestingly, the $3(1+\nu)t_0$ slope value is characteristic for a zig-zag CNT in tension [149].

8.3 The Effective Tensional Strain Concept

To probe this theory, we carried out symmetry-adapted MD simulations for a variety of H-terminated GNRs under various levels of twist. The agreement is evident from the analysis performed in Figure 8.3, plotting the band-gap variations for a set of narrow GNRs with $N = 9$, 10 and 11. Note that we considered the effect of elongation of $|\mathbf{T}|$ during the twisting process since it may introduce considerable band-gap deviations. Therefore, in Figure 8.3 we included data in which the axial component $|\mathbf{T}|$ was both kept fixed (open circles) and allow to relax (filled circles) at each twist level. In both cases, the quadratic band-gap variations with γ rescale

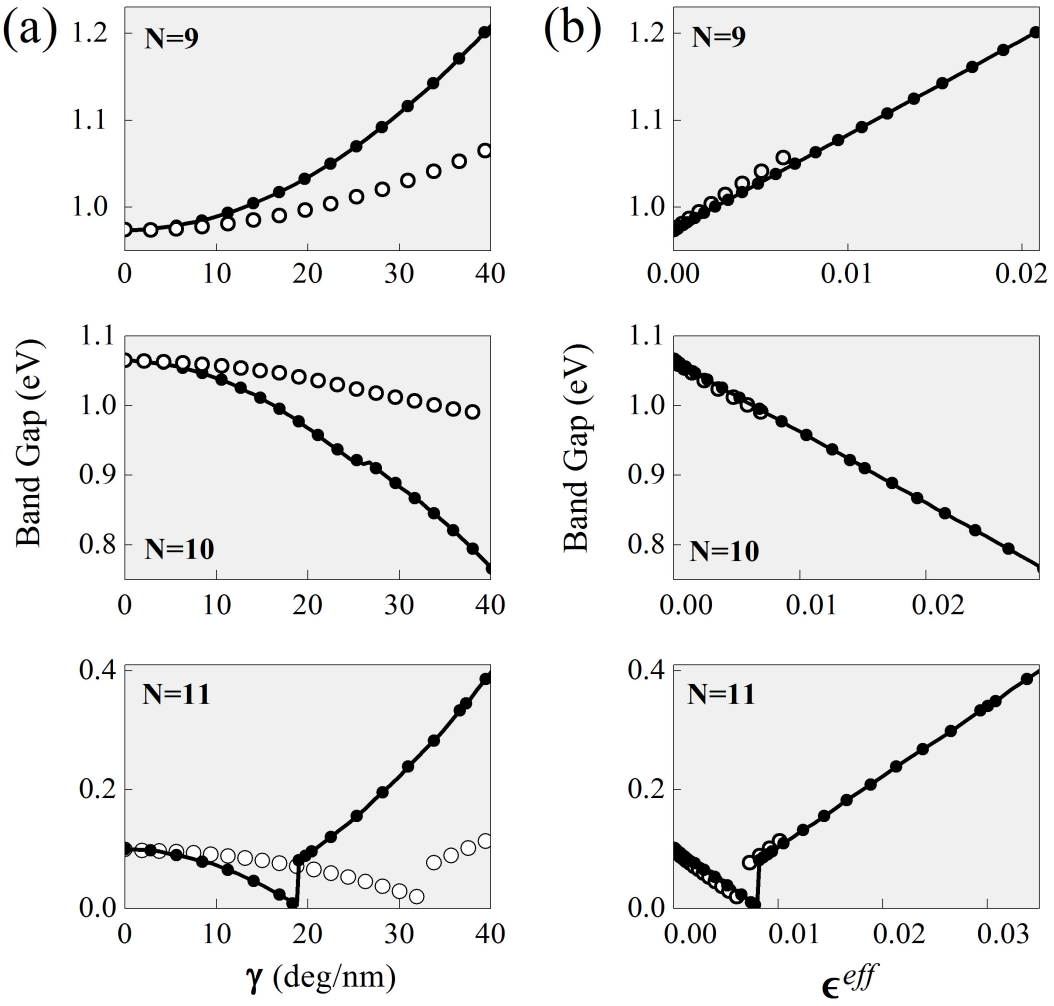

FIGURE 8.3: Fundamental band-gaps of H-terminated armchair GNRs with $N = 9$, 10 and 11 vs. (a) the applied twist rate and (b) the effective tension strain. Filled (open) circles correspond to simulations in which $|\mathbf{T}|$ was kept fixed (relaxed) during twisting.

into linear variations with ε^{eff}. The measured slopes, 10.7 eV ($N = 9$), 10.5 eV ($N = 10$), and 11.1 eV ($N = 11$) are all close in value.

The displayed band-gap variations with ϵ^{eff} for 11 GNR reveals an unexpected feature. The band-gap for the stress free state is solely due to the edge compression effect [7]. The application of twist gradually cancels this effect, leading to the closure of the gap noted earlier [173]. However, the jump exhibited immediately after, at $\gamma = 19$ deg/nm, is new, and not captured in the effective model. We interpret this behavior as a Peierls effect since the gap opening coincides with the relaxation of the twisted GNR into a Kekulé type bond alternation pattern [174],

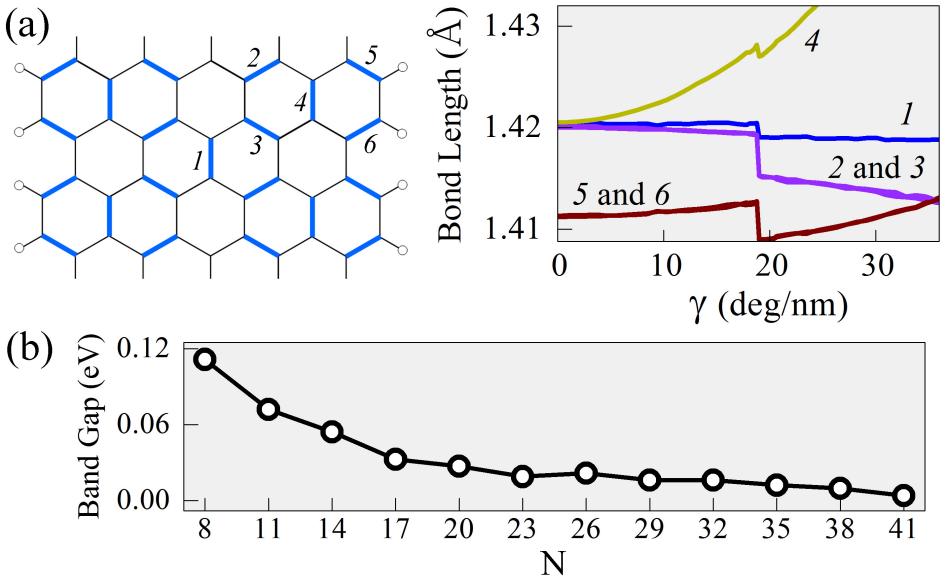

FIGURE 8.4: (a) Schematics of the Kekulé type bond alternation pattern in 11 GNR. The H atoms are represented with open circles. The thicker (blue) lines identify the bonds that suddenly shrink at 20 deg/nm. (left) Evolution of the selected bond lengths vs. twist rate. (right) (c) Broader view in the band-gap response to the Peierls distortion for twisted $N = 3p + 2$ GNR of various widths.

Figure 8.4(a). Although in wider $N = 3p + 2$ GNRs this effect emerges at lower γ, the resulted band-gap jumps are rapidly vanishing with N, Figure 8.4(b), and the behavior around the cusp is dominated by the averaged strain.

Further symmetry-adapted MD simulations reveal that the perturbative model based on ϵ^{eff} can be applied with confidence in wide GNRs as well. Interestingly, we uncovered rippling deformations, a phenomenon not reported before. The developed rippling state, Figure 8.5(a), represents a FCNT [169, 170], i.e., a bilayer GNR structure connected by one central ridge. The FCNT wall stores elastic tension, which is most significant at the two edges and the central ridge, Figure 8.5(b). Nevertheless, the effective strain lumps effectively this strain distribution, as it is evident from Figure 8.5(c). The emergence of rippling at $\gamma = 7$ deg/nm, interrupts the linear band-gap variation with γ, but becomes invisible in the ϵ^{eff} space.

Of special interest is the observation that in the ϵ^{eff} space, the H-terminated 41-GNR behaves similarly with the seamless $(42, 0)$ SWNTs in tension, Figure 8.5(c) right. (For CNT, the effective strain is identical with the homogeneous one.)

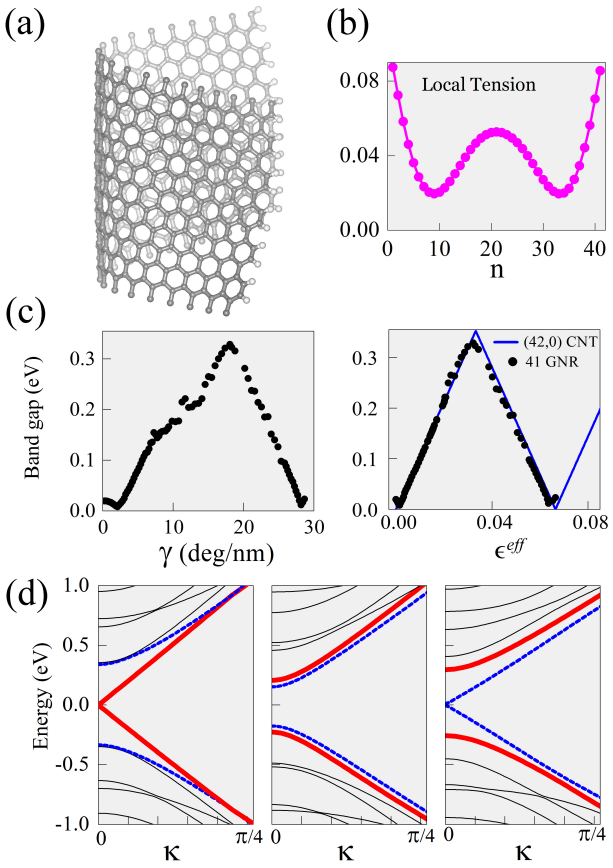

FIGURE 8.5: Electromechanical behavior of H-saturated 41 GNR (a) Under $\gamma =$ 21 deg/nm the GNR folds into a bilayer structure known as a fractional nanotube. (b) The distribution of local tensional strain in the molecule motif. Band gap vs. (c) twist rate and (d) effective tension strain. The bang-gap variation in a $(42, 0)$ CNT in tension (solid blue line) is shown for a comparison. (e) Closeups of the band structures around the Fermi level (set to zero) at three ϵ^{eff} values: 0.001, 0.032 and 0.064. Horizontal axis is the helical quantum number κ. The two bands around the Fermi level are depicted with distinct lines to show their coupling with γ.

While the identity in slope is no longer surprising, the coincidence in oscillation period deserves further investigation. The coupling to the frontier valence and conduction bands detailed in Figure 8.5(e), is qualitatively similar with the one observed earlier in CNTs [158]. A very small deformation leads to gap closure, Figure 8.5(d) left. Next, twisting couples in an inverse manner to the frontier bands: While it opens a gap between HOMO and LUMO bands (thick continuous line), at the same time it decreases the gap between the HOMO-1 and LUMO+1 one (thick dashed line). At the next shown sequence, Figure 8.5(e)-center, the

fundamental band-gap is already given by the HOMO-1 and LUMO+1 bands. Under further twisting, Figure 8.5(e) right, the metallic character is regained when the HOMO-1 and LUMO+1 bands intersect [175]. From the initial Hamiltonian H_0, we can obtain analytically that band-gap between the HOMO-1 and LUMO+1 levels follow an identical linear dependence with ϵ^{eff}. Knowing the initial HOMO-1 and LUMO+1 gap value and the $3t_0(1+\nu)$ decreasing slope, the obtained GNR' oscillation period is $\delta\epsilon^{eff} = 2\pi/\sqrt{3}(1+\nu)(N+1)$. Indeed, this oscillation period is characteristic for a (N+1,0) CNT [149].

Chapter 9

Conclusions

Computational nanomechanics is the very topic of this research. When size scales down to the nano level, the structure-property relationship differs from bulk. New effects, such the surface relaxation and interface interaction, have to be considered. Quantum confinement and structural discreteness also become important. New computational tools and theories are needed for runderstanding of these emerging phenomena. Symmetry-adapted MD is one of the responses.

Despite the complex morphology of nanostructures involving chirality, buckling, rippling, defects, and glide, we are able to extract the mechanical and electronic data via the newly developed symmetry-adapted MD capability. This is because, standing for a generalization of the conventional MD under periodic boundary conditions (PBC), symmetry-adapted MD displays more flexibility than PBC MD. In symmetry-adapted MD, we make recourse of helical symmetry instead of translation. We note that both translation and rotation can be treated as special helical symmetries. There are multiple choices of helical vectors. Hence the computation can be performed on a relative small repeating domain which is compatible to corresponding helical vector, disregarding the translational periodicity, which could be huge. On one hand, the helical symmetry exists in a large class of quasi-one dimensional nanostructures, so called nanowire, nanotube, nanorobe, nanoribbon and so on. On the other hand, the helical symmetry may also be created by the external fundamental type of deformations such as bending and torsion. We also note that the utility of helical symmetry comes from the fact that, without the

constrain on the point symmetry group of three dimensional bulks, other symmetry components than translation such as rotation, screw are available to simplify the computations.

Therefore the concept of symmetry-adapted MD opens a new area of computational nanomechanics which, on the contrary, is largely forbidden to PBC MD due to the computational limit for number of atoms that can be treated with quantum mechanical accuracy. Indeed, we have successfully perfomed the calculations of mechanical and electronic properties for carbon & MoS_2 nanostructures and the outcomes are useful.

For the first time, we present an extensive study on elasticity of carbon nanotubes (CNTs) under small tension or shear deformation lower than 0.5% and a scaling of elastic reponse of CNTs are obtained. The unique conjuncture of the size and chirality dependence for both Young's modulus and shear modulus validates the isotropic continuum idealization for CNTs with diameter > 1.25 nm.

Regarding the nonlinear elastic response of CNTs, we found a transient state intermediate between the linear regime and the buckling regime, which is allowed since *pure* bending or torsion is applied. On the contrary, in PBC MD, to study the nonlinear mechanics, a cluster representation is employed. The deformation is loaded to finite long CNTs via frozen atoms at the two ends. First, the carbon nanotubes are fully relaxed, then bent with uniform curvature or twisted with uniform twist rate. Finally, the ends were fixed and the SWCNTs were again relaxed. This frozen-atom boundary conditions screen the transient state out.

With symmetry-adapted MD, we are able to simulate NTs with hexagonal wall as screw dislocations. This new viewpoint bring us new findings. A near axial glide in NTs under torsion is revealed despite that the previous reported near circumferential glide of CNTs under tension. More interestingly, we found that in MoS_2 NTs, a non-vanishing intrinsic twist exists in most chiral NTs.

With symmetry-adapted MD, it is also convenient to obtain band structure information of NTs, which enables us to study the electromechanical response of CNTs under fundamental type of deformation, torsion, for example. Despite of the complex morphology of helically rippled CNTs and Graphene nanoribbons,

our efforts demonstrate that the turnable-by-strain electronic structures can be understood based on the well known behavior of flat graphene. Specifically, we introduce a new concept of *effective strain*, stimulated by the concept of effective mass in solid state physics.

Indeed, we found that the concept of *effective strain* is the key to understand the band-gap modulations in twisted carbon nanostructures including nanotubes and nanoribbons without involving any complex physics. It bridges the already-known CNT's and the less-known behaviors of rippled CNTs or GNRs. We indicate that for other nanotubes and nanoribbons made from a one-atom-thick planar sheets, such as boron-nitride systems, the concept of *effective strain* can be also valid.

Even though *effective strain* was introduced to provide a simple physics understanding in electronic domain, it can also be used in mechanical domain. For example, for multi-walled CNTs under torsional deformation, a second linear mechanical behavior was observed when the twist is beyond the idealized linear regime, where the rippling is initialized. This is known as bilinear behavior. However, when *effective strain* is used, this second linear regime resume the idealized linear behavior. Thus *effective strain* finds itself a mechanical interpretation.

9.1 Future Research

Therefore, towards multiscale modeling, the next step will construct the continuum description of nano-objectis with the symmetry-adapted MD data. This would be our ultimate goal of the research conducted in our group. To do this, here we would not try to derive all the formulations [21, 23–27, 126] to build the continuum by the means of Cauthy-Born rule, which could be another research. Instead, to delineate the logic concisely, we indicate the usage of symmetry-adapted MD data for continuum modeling by examples for carbon nanotubes (CNTs). In reality, CNTs have been employed to use as elastic spring. Figure 9.1 shows a nano electromechanical device made from single CNT, from which, both elasticity and conductivity could be studied by manipulating the rotating metal pendant suspended on the CNT. Such a problem is a paradigm where both atomistic (symmetry-adapted MD) and continuum treatments can be used.

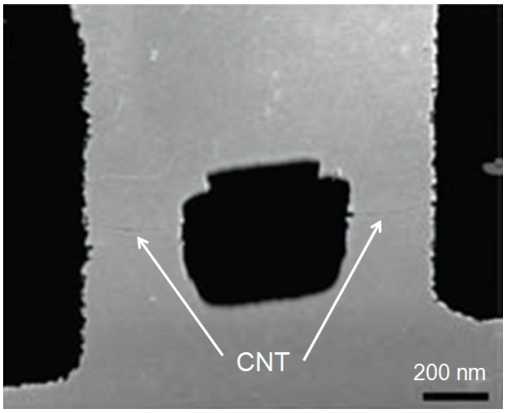

FIGURE 9.1: Torsional pendulum based on a SWCNT. Image shows a rotating metal block suspended on the SWCNT. Adapted from Ref. [8].

In practice, one is prone to choose the linear elasticity as the first trial. To conduct the mechanics, the macroscopic Hooke's law is employed. The force exerted on objects responses to the strain in a linear fashion. The strain energy is evaluated via an integral of strain. The only parameter needed is the force constant, κ, reflecting the resistance of materials, which can be measured microscopically in terms of elastic constants (Young's modulus and shear modulus).

Very often, CNTs will encounter severe mechanical manipulation. For example, a CNT under torsion with cylindrical shape will develop the helical rippled morphology when the twist is beyond certain threshold. SWCNTs will collapse completely into a flatten shape eventually. The dramatic change of morphology will alter the mechanical behavior of CNTs. Therefore the critical twist rate will reflects the mechanical properties of CNTs. Our symmetry-adapted MD calculations indicate that the critical twist heavily depends on the size of CNTs (Figure 7.3).

Rippling can also take place in multi-walled NTs under torsion. Figure 7.6 indicates that when the core consisting of small size CNTs are absented, MWCTNs can also collapse into flatten shape when the twist beyond the threshold. More interestingly, we see that the force constants (also called torque) of rippled MWCNTs vary linearly with twist, indicating that the rippled MWCNTs display linearly mechanical response to twist. We also note that no similar transient regime which links the idealized linear region and the rippled region as in SWCNTs was found. Those features are called bilinear mechanics [126].

As discussed in Chapter 7, compared to idealized MWCNTs, rippled MWCNTs become softer in the second linear regime, where MWCNTs are of lower value of torque than the idealized MWCNTs with cylindrical shape (Figure 7.6). We indicate that this softening can be understood with *effective strain*. Indeed, when the curve of torque is rescaled with *effective strain*, the MWCNTs resume the idealized linear behavior, indicating that Hooke's law for the idealized linear mechanics can be extended to study rippled states.

Therefore, for rippled MWCNTs in torsion, to construct the continuum description, two extra parameters are necessary – critical twist and of *effective strain* – besides the force constants in Hooke's law. We note that a parallel argument can also made to the rippling induced by bending deformation. Apparently, a database for critical twist and scaling of *effective strain* of a large class of CNTs has to be constructed by symmetry-adapted MD calculations.

Turning to the conductivity, another important aspect of CNTs, we also indicate how critical twist rate and effective strain can be used for continuum descriptions. For idealized CNTs in torsion, a standard Yang-Han π-ortibals modeling could be used to obtain the scaling of the fundamental energy gap tuned by twist. For large diameter CNTs, a zigzag periodical variation of energy gap between zero and a maximum can be achieved with moderate twist. Figure 7.4 shows several periods of the energy gap vs. twist. Therefore, even though the amplitude of the conductance could not be derived from the energy gap directly, a metal-semiconductor-metal/semiconductor-metal-semiconductor periodical transition, one of the most important functions expected for nano-devices can be obtained using energy gap information merely.

Figure 7.7 presents that such transition periods in terms of twist rate varies as the rippled state is initialized. But when we use *effective strain* rescaling, the period for idealized CNTs with cylindrical shape is resumed. Therefore, critical twist and *effective strain* can also be important parameters of continuum description of conductivity as well.

Bibliography

[1] T. Natsuki, K. Tantrakarn, and M. Endo. Prediction of elastic properties for single-walled carbon nanotubes. *Carbon*, 42(1):39–45, 2004.

[2] V.N. Popov, V.E. Van Doren, and M. Balkanski. Elastic properties of single-walled carbon nanotubes. *Physical Review B*, 61(4):3078–3084, 2000.

[3] J.P. Lu. Elastic Properties of Carbon Nanotubes and Nanoropes. *Physical Review Letters*, 79(7):1297–1300, 1997.

[4] S. Iijima, C. Brabec, A. Maiti, and J. Bernholc. Structural flexibility of carbon nanotubes. *The Journal of Chemical Physics*, 104(5):2089, 1996.

[5] B.I. Yakobson, C.J. Brabec, and J. Bernholc. Nanomechanics of Carbon Tubes: Instabilities beyond Linear Response. *Physical Review Letters*, 76 (14):2511–2514, 1996.

[6] Y. Shibutani and S. Ogata. Mechanical integrity of carbon nanotubes for bending and torsion. *Modelling and Simulation in Materials Science and Engineering*, 12(4):599–610, 2004.

[7] Y.W. Son, M.L. Cohen, and S.G. Louie. Energy gaps in graphene nanoribbons. *Physical Review Letters*, 97(21):216803, 2006.

[8] J.C. Meyer, M. Paillet, and S. Roth. Single Molecule Torsional Pendulum, *science*, 309, 1539–1541, 2005.

[9] S. Iijima. Helical microtubules of graphitic carbon. *Nature*, 354(6348):56–58, 1991.

[10] N.G. Chopra, R.J. Luyken, K. Cherrey, V.H. Crespi, M.L. Cohen, S.G. Louie, and A. Zettl. Boron Nitride Nanotubes. *Science*, 269(5226):966–967, 1995.

[11] H. Dai, E.W. Wong, Y.Z. Lu, S. Fan, and C.M. Lieber. Synthesis and characterization of carbide nanorods. *Nature*, 375(6534):769–772, 1995.

[12] P. Yang and C.M. Lieber. Nanorod-Superconductor Composites: A Pathway to Materials with High Critical Current Densities. *Science*, 273(5283):1836–1840, 1996.

[13] K. Nakada, M. Fujita, G. Dresselhaus, and M.S. Dresselhaus. Edge state in graphene ribbons: Nanometer size effect and edge shape dependence. *Physical Review B*, 54(24):17954–17961, 1996.

[14] M. Fujita, K. Wakabayashi, K. Nakada, and K. Kusakabe. Peculiar localized state at zigzag graphite edge. *Journal of the Physical Society of Japan*, 65 (7):1920–1923, 1996.

[15] D. Qian, G.J. Wagner, and W.K. Liu. A multiscale projection method for the analysis of carbon nanotubes. *Computer Methods in Applied Mechanics and Engineering*, 193(17-20):1603–1632, 2004.

[16] T. Belytschko, S.P. Xiao, G.C. Schatz, and R.S. Ruoff. Atomistic simulations of nanotube fracture. *Physical Review B*, 65(23):235430, 2002.

[17] K.M. Liew, C.H. Wong, X.Q. He, M.J. Tan, and S.A. Meguid. Nanomechanics of single and multiwalled carbon nanotubes. *Physical Review B*, 69(11): 115429, 2004.

[18] X. Li, W. Yang, and B. Liu. Bending Induced Rippling and Twisting of Multiwalled Carbon Nanotubes. *Physical Review Letters*, 98(20):205502, 2007.

[19] W.K. Liu, E.G. Karpov, S. Zhang, and H.S. Park. An introduction to computational nanomechanics and materials. *Computer Methods in Applied Mechanics and Engineering*, 193(17-20):1529–1578, 2004.

[20] W.W. Gerberich, W.M. Mook, C.R. Perrey, C.B. Carter, M.I. Baskes, R. Mukherjee, A. Gidwani, J. Heberlein, P.H. McMurry, and S.L. Girshick. Superhard silicon nanospheres. *Journal of the Mechanics and Physics of Solids*, 51(6):979–992, 2003.

[21] M. Arroyo and T. Belytschko. An atomistic-based finite deformation membrane for single layer crystalline films. *Journal of the Mechanics and Physics of Solids*, 50(9):1941–1977, 2002.

[22] M. Arroyo and T. Belytschko. Nonlinear Mechanical Response and Rippling of Thick Multiwalled Carbon Nanotubes. *Physical Review Letters*, 91(21): 215505, 2003.

[23] S. Zhang, S.L. Mielke, R. Khare, D. Troya, R.S. Ruoff, G.C. Schatz, and T. Belytschko. Mechanics of defects in carbon nanotubes: Atomistic and multiscale simulations. *Physical Review B*, 71(11):115403, 2005.

[24] A.Y.T. Leung, X. Guo, X.Q. He, H. Jiang, and Y. Huang. Postbuckling of carbon nanotubes by atomic-scale finite element. *Journal of Applied Physics*, 99:124308, 2006.

[25] B. Liu, H. Jiang, Y. Huang, S. Qu, M.F. Yu, and K.C. Hwang. Atomic-scale finite element method in multiscale computation with applications to carbon nanotubes. *Physical Review B*, 72(3):35435, 2005.

[26] P. Zhang, Y. Huang, P.H. Geubelle, P.A. Klein, and K.C. Hwang. The elastic modulus of single-wall carbon nanotubes: a continuum analysis incorporating interatomic potentials. *International Journal of Solids and Structures*, 39(13-14):3893–3906, 2002.

[27] P. Zhang, H. Jiang, Y. Huang, P.H. Geubelle, and K.C. Hwang. An atomistic-based continuum theory for carbon nanotubes: analysis of fracture nucleation. *Journal of the Mechanics and Physics of Solids*, 52(5): 977–998, 2004.

[28] L.V. Zhigilei, C. Wei, and D. Srivastava. Mesoscopic model for dynamic simulations of carbon nanotubes. *Physical Review B*, 71(16):165417, 2005.

[29] R.M. Martin. Electronic structure: basic theory and practical methods. *publisher: Cambridge University Press*, 2005.

[30] N.M. Ghoniem, E.P. Busso, N. Kioussis, and H. Huang. Multiscale modelling of nanomechanics and micromechanics: an overview. *Philisophical Magazine*, 83(31):3475–3528, 2003.

[31] W. Kohn and L.J. Sham. Self-Consistent Equations Including Exchange and Correlation Effects. *Physical Review*, 140(4A):A1133–A1138, 1965.

[32] J.C. Slater and G.F. Koster. Simplified LCAO Method for the Periodic Potential Problem. *Physical Review*, 94(6):1498–1524, 1965.

[33] C.M. Goringe, D.R. Bowler, and E. Hernández. Tight-binding modelling of materials. *Reports on Progress in Physics*, 60(12):1447–1512, 1997.

[34] R. Saito, G. Dresselhaus, and M.S. Dresselhaus. Physical properties of carbon nanotubes. *publisher: Imperial College Press*, 2005.

[35] C.T. White, D.H. Robertson, and J.W. Mintmire. Helical and rotational symmetries of nanoscale graphitic tubules. *Physical Review B*, 47(9):5485–5488, 1993.

[36] V.N. Popov. An equivalent non-orthogonal TB formalism using Bloch sums adapted for screw and translation operations can be found in . *New Journal of Physics*, 6(1):17, 2004.

[37] P.B. Allen. Nanocrystalline Nanowires: III. Electrons. *Nano Lett*, 7(5): 1220–1223, 2007.

[38] T. Dumitrică and R.D. James. Objective molecular dynamics. *Journal of the Mechanics and Physics of Solids*, 55(10):2206–2236, 2007.

[39] R.D. James. Objective Structures. *Journal of the Mechanics and Physics of Solids*, 54:2354–2390, 2007.

[40] R. Rurali and E. Hernández. Trocadero: a multiple-algorithm multiple-model atomistic simulation program. *Computational Materials Science*, 28 (2):85–106, 2003.

[41] P. Valentini, W.W. Gerberich, and T. Dumitrică. Phase-Transition Plasticity Response in Uniaxially Compressed Silicon Nanospheres. *Physical Review Letters*, 99(17):175701, 2007.

[42] E.B. Barros, A. Jorio, G.G. Samsonidze, R.B. Capaz, A.G. Souza Filho, J. Mendes Filho, G. Dresselhaus, and M.S. Dresselhaus. Review on the symmetry-related properties of carbon nanotubes. *Physics Reports*, 431(6): 261–302, 2006.

[43] Contescu C. I. Schwarz J. A. and Putyera K. *Dekker Encyclopedia of Nanoscience and Nanotechnology*. 5:3567, 2004.

[44] V. Sankaran, K.W. Kim, and G.J. Iafrate. Tight-binding study of optical properties in short-period $In_{0.53}Ga_{0.47}As/InP$ superlattices. *Physical Review B*, 53(11):6939–6942, 1996.

[45] D. Porezag, T. Frauenheim, T. Köhler, G. Seifert, and R. Kaschner. Construction of tight-binding-like potentials on the basis of density-functional theory: Application to carbon. *Physical Review B*, 51(19):12947–12957, 1995.

[46] C.H. Xu, C.Z. Wang, C.T. Chan, and K.M. Ho. A transferable tight-binding potential for carbon. *Journal of Physics: Condensed Matter*, 4:6047–6054, 1992.

[47] M. Born and G. R. Oppenheimer. Zur Quantentheorie der Molekeln. *Ann. Physik*, 84:457, 1927.

[48] W.A. Harrison. Electronic structure and the properties of solids: The physics of the chemical bond. *publisher: W. H. Freeman and Company*, 1980.

[49] P. Vogl, H.P. Hjalmarson, and J.D. Dow. Semi-empirical tight-binding theory of the electronic structure of semiconductors. *Journal of Physics and Chemistry of Solids*, 44(5):265–378, 1983.

[50] E. Hernández, C. Goze, P. Bernier, and A. Rubio. Elastic Properties of C and $B_xC_yN_z$ Composite Nanotubes. *Physical Review Letters*, 80(20):4502–4505, 1998.

[51] J.B. Wang, X. Guo, H.W. Zhang, L. Wang, and J.B. Liao. Energy and mechanical properties of single-walled carbon nanotubes predicted using the higher order Cauchy-Born rule. *Physical Review B*, 73(11):115428, 2006.

[52] R. Kaschner, Th. Frauenheim, T. Köhler, and G. Seifert. *J. Comp. Aided Mat. Design*, 4(20):53, 1997.

[53] D. Srivastava, C. Wei, and K. Cho. Nanomechanics of carbon nanotubes and composites. *Applied Mechanics Reviews*, 56:215, 2003.

[54] T. Frauenheim, F. Weich, T. Köhler, S. Uhlmann, D. Porezag, and G. Seifert. Density-functional-based construction of transferable nonorthogonal tight-binding potentials for Si and SiH. *Physical Review B*, 52(15):11492–11501, 1995.

[55] P.K. Sitch, T. Frauenheim, and R. Jones. A density functional tight-binding approach for modelling Ge and GeH structures. *Journal of Physics: Condensed Matter*, 8(37):6873–6888, 1996.

[56] J. Widany, T. Frauenheim, and W.R.L. Lambrecht. Investigation of the stability of the hexagonal–cubic born nitride prism interface. *Journal of Materials Chemistry*, 6(5):899–901, 1996.

[57] F. Weich, J. Widany, and T. Frauenheim. Paracyanogenlike Structures in High-Density Amorphous Carbon Nitride. *Physical Review Letters*, 78(17): 3326–3329, 1997.

[58] R. Gutierrez, T. Frauenheim, T. Köhler, and G. Seifert. Stability of silicon carbide structures: from clusters to solid surfaces. *Journal of Materials Chemistry*, 6(10):1657–1663, 1996.

[59] M. Haugk, J. Elsner, and T. Frauenheim. A density-functional based tight-binding approach to GaAs surface reconstructions. *Journal of Physics: Condensed Matter*, 9(35):7305–7315, 1997.

[60] M. F. Ciappina, A. Becker, and A. Jaroń-Becker. Multislit interference patterns in high-order harmonic generation in C_{60}. *Physical Review A*, 76 (6):63406, 2007.

[61] F.H. Stillinger and T.A. Weber. Computer simulation of local order in condensed phases of silicon. *Physical Review B*, 31(8):5262–5271, 1985.

[62] J. Tersoff. Modeling solid-state chemistry: Interatomic potentials for multicomponent systems. *Physical Review B*, 39(8):5566–5568, 1989.

[63] H. Balamane, T. Halicioglu, and W. A. Tiller. Comparative study of silicon empirical interatomic potentials. *Physical Review B*, 46(4):2250–2279, 1992.

[64] Tang C. Golberg D., Bando Y. and Zhi C. Boron Nitride Nanotubes. *Advanced Materials*, 19:2413–2432, 2007.

[65] A.P. Suryavanshi, M.-F. Yu, J.G. Wen, C.C Tang, and Y. Bando. Elastic modulus and resonance behavior of boron nitride nanotubes. *Applied Physics Letters*, 84(14):2527, 2004.

[66] V. Verma, V.K. Jindal, and K. Dharamvir. Elastic moduli of a boron nitride nanotube. *Nanotechnology*, 18(435711):435711, 2007.

[67] K.N. Kudin, G.E. Scuseria, and B.I. Yakobson. C_2, F, BN, and C nanoshell elasticity from ab initio computations. *Physical Review B*, 64(23):235406, 2001.

[68] D. Stojkovic, P.E. Lammert, and V.H. Crespi. Electronic Bisection of a Single-Wall Carbon Nanotube by Controlled Chemisorption. *Physical Review Letters*, 99(2):26802, 2007.

[69] X. Wang, R.Q. Zhang, S.T. Lee, T.A. Niehaus, and T. Frauenheim. Unusual size dependence of the optical emission gap in small hydrogenated silicon nanoparticles. *Applied Physics Letters*, 90:123116, 2007.

[70] I. Milošević, B. Nikolić, E. Dobardžić, M. Damnjanović, I. Popov, and G. Seifert. Electronic properties and optical spectra of MoS_2 and WS_2 nanotubes. *Physical Review B*, 76(23):233414, 2007.

[71] P. Koskinen, H. Häkkinen, G. Seifert, S. Sanna, T. Frauenheim, and M. Moseler. Density-functional based tight-binding study of small gold clusters. *New Journal of Physics*, 8(1):9, 2006.

[72] M. Yang, K.A. Jackson, C. Koehler, T. Frauenheim, and J. Jellinek. Structure and shape variations in intermediate-size copper clusters. *The Journal of Chemical Physics*, 124:024308, 2006.

[73] W. Yang. Direct calculation of electron density in density-functional theory. *Physical Review Letters*, 66(11):1438–1441, 1991.

[74] G. Dereli and C. Özdoğan. O (N) algorithms in tight-binding molecular-dynamics simulations of the electronic structure of carbon nanotubes. *Physical Review B*, 67(3):35415, 2003.

[75] W. Rhodes. Symmetry of Helical Polymers. Electronic States of Double-Stranded Polynucleotides. *The Journal of Chemical Physics*, 37:2433, 2004.

[76] I. Božović and J. Delhalle. Symmetry-adapted linear combination of atomic orbitals bases and band-structure computation for quasi-one-dimensional solids. *Physical Review B*, 29(8):4733–4746, 1984.

[77] W. Koch and F.F. Seelig. Symmetry orbitals for one-electron band-structure computations of one-dimensional crystals. *International Journal of Quantum Chemistry*, 32(2):249–264, 1987.

[78] The phase related with the atomic location inside the objective cell was not included as it can be eliminated by a unitary transformation. This intracell factor is typically included if needed, as for example to couple the system to an external field [176], a situation less applicable for OMD as the TB potential invariance could be altered.

[79] H.C. Andersen. Molecular dynamics simulations at constant pressure and/or temperature. *The Journal of Chemical Physics*, 72:2384, 1980.

[80] S. Nosé. A molecular dynamics method for simulations in the canonical ensemble. *Molecular Physics*, 100(1):191–198, 2002.

[81] S. Nosé. A unified formulation of the constant temperature molecular dynamics methods. *The Journal of Chemical Physics*, 81:511, 1984.

[82] W.G. Hoover. Canonical dynamics: Equilibrium phase-space distributions. *Physical Review A*, 31(3):1695–1697, 1985.

[83] M.Z. Bazant, E. Kaxiras, and JF Justo. Environment-dependent interatomic potential for bulk silicon. *Physical Review B*, 56(14):8542–8552, 1997.

[84] F. Ercolessi, E. Tosatti, and M. Parrinello. Au (100) Surface Reconstruction. *Physical Review Letters*, 57(6):719–722, 1986.

[85] M.S. Daw and MI Baskes. Embedded-atom method: Derivation and application to impurities, surfaces, and other defects in metals. *Physical Review B*, 29(12):6443–6453, 1984.

[86] D.D.D. Ma, C.S. Lee, F.C.K. Au, S.Y. Tong, and S.T. Lee. Small-Diameter Silicon Nanowire Surfaces, *science*, 299, 1874–1877, 2003.

[87] Y. Wu, Y. Cui, L. Huynh, C.J. Barrelet, D.C. Bell, and C.M. Lieber. Controlled growth and structures of molecular-scale silicon nanowires. *Nano Lett*, 4(3):433–436, 2004.

[88] M. Takeguchi, M. Tanaka, H. Yasuda, and K. Furuya. Real-time high-resolution transmission electron microscopy observation of the growth process of (001) surfaces on a nanometer-sized Si multiply twinned particle. *Surface Science*, 493(1):414–419, 2001.

[89] A.F. Morral, J. Arbiol, J.D. Prades, A. Cirera, and J.R. Morante. Synthesis of Silicon Nanowires with Wurtzite Crystalline Structure by Using Standard Chemical Vapor Deposition. *Adv. Mater*, 19:1347–1351, 2007.

[90] J. Bai, X. C. Zeng, H. Tanaka, and J. Y. Zeng. Metallic single-walled silicon nanotubes. *Proceedings of the National Academy of Sciences*, 101(9):2664–2668, 2004.

[91] T. Dumitrică, M. Hua, and B.I. Yakobson. Endohedral silicon nanotubes as thinnest silicide wires. *Physical Review B*, 70(24):241303, 2004.

[92] R. Rurali and N. Lorente. Metallic and Semimetallic Silicon $< 100 >$ Nanowires. *Physical Review Letters*, 94(2):26805, 2005.

[93] R. Kagimura, R.W. Nunes, and H. Chacham. Structures of Si and Ge Nanowires in the Subnanometer Range. *Physical Review Letters*, 95(11): 115502, 2005.

[94] Y. Zhao and B.I. Yakobson. What is the Ground-State Structure of the Thinnest Si Nanowires? *Physical Review Letters*, 91(3):35501, 2003.

[95] I. Ponomareva, M. Menon, D. Srivastava, and A.N. Andriotis. Structure, Stability, and Quantum Conductivity of Small Diameter Silicon Nanowires. *Physical Review Letters*, 95(26):265502, 2005.

[96] I. Ponomareva, M. Menon, E. Richter, and A.N. Andriotis. Structural stability, electronic properties, and quantum conductivity of small-diameter silicon nanowires. *Physical Review B*, 74(12):125311, 2006.

[97] K. Nishio, T. Morishita, W. Shinoda, and M. Mikami. Molecular dynamics simulations of self-organized polyicosahedral Si nanowire. *The Journal of Chemical Physics*, 125:074712, 2006.

[98] J.F. Justo, R.D. Menezes, and L.V.C. Assali. Stability and plasticity of silicon nanowires: The role of wire perimeter. *Physical Review B*, 75(4): 45303, 2007.

[99] F. Glas, J.C. Harmand, and G. Patriarche. Why Does Wurtzite Form in Nanowires of III-V Zinc Blende Semiconductors? *Physical Review Letters*, 99(14):146101, 2007.

[100] Y. Zhao, Y.H. Kim, M.H. Du, and S.B. Zhang. First-Principles Prediction of Icosahedral Quantum Dots for Tetravalent Semiconductors. *Physical Review Letters*, 93(1):15502, 2004.

[101] S.G. Hao, D.-B. Zhang, and T. Dumitrică. Effect of small shape changes on the optical response of highly symmetric silicon quantum dots. *Physical Review B*, 76(8):81305, 2007.

[102] A. Ramstad, G. Brocks, and P.J. Kelly. Theoretical study of the Si (100) surface reconstruction. *Physical Review B*, 51(20):14504–14523, 1995.

[103] AM Fennimore, TD Yuzvinsky, W.Q. Han, MS Fuhrer, J. Cumings, and A. Zettl. Rotational actuators based on carbon nanotubes. *Nature*, 424 (6947):408–410, 2003.

[104] AR Hall, L. An, J. Liu, L. Vicci, MR Falvo, R. Superfine, and S. Washburn. Experimental measurement of single-wall carbon nanotube torsional properties. *Physical review letters*, 96(25):256102, 2006.

[105] S. Zhang, S.L. Mielke, R. Khare, D. Troya, R.S. Ruoff, G.C. Schatz, and T. Belytschko. Mechanics of defects in carbon nanotubes: atomistic and multiscale simulations. *Physical Review B*, 71(11):115403, 2005.

[106] D.W. Brenner. Empirical potential for hydrocarbons for use in simulating the chemical vapor deposition of diamond films. *Physical Review B*, 42(15): 9458–9471, 1990.

[107] Y. Huang, J. Wu, and KC Hwang. Thickness of graphene and single-wall carbon nanotubes. *Physical Review B*, 74(24):245413, 2006.

[108] E.B. Tadmor, G.S. Smith, N. Bernstein, and E. Kaxiras. Mixed finite element and atomistic formulation for complex crystals. *Physical Review B*, 59(1): 235–245, 1999.

[109] Y. Wu, X. Zhang, A.Y.T. Leung, and W. Zhong. An energy-equivalent model on studying the mechanical properties of single-walled carbon nanotubes. *Thin-Walled Structures*, 44(6):667–676, 2006.

[110] A.Y.T. Leung, W. Yongdong, and Z. Weifang. Computation of Youngs moduli for chiral single-walled carbon nanotubes. *Applied Physics Letters*, 88:251908, 2006.

[111] D.W. Brenner, O.A. Shenderova, J.A. Harrison, S.J. Stuart, B. Ni, and S.B. Sinnott. A second-generation reactive empirical bond order (REBO) potential energy expression for hydrocarbons. *Journal of Physics: Condensed Matter*, 14:783, 2002.

[112] P. Zhang, Y. Huang, PH Geubelle, PA Klein, and KC Hwang. The elastic modulus of single-wall carbon nanotubes: a continuum analysis incorporating interatomic potentials. *International Journal of Solids and Structures*, 39(13-14):3893–3906, 2002.

[113] T. Halicioglu. Stress calculations for carbon nanotubes. *Thin Solid Films*, 312(1-2):11–14, 1998.

[114] AYT Leung, W. Yongdong, and Z. Weifang. Computation of Youngs moduli for chiral single-walled carbon nanotubes. *Applied Physics Letters*, 88: 251908, 2006.

[115] D.-B. Zhang, M. Hua, and T. Dumitrică. Stability of polycrystalline and wurtzite Si nanowires via symmetry-adapted tight-binding objective molecular dynamics. *The Journal of Chemical Physics*, 128:084104, 2008.

[116] E. Ertekin and DC Chrzan. Ideal torsional strengths and stiffnesses of carbon nanotubes. *Physical Review B*, 72(4):45425, 2005.

[117] B.W. Jeong, J.K. Lim, and S.B. Sinnott. Elastic torsional responses of carbon nanotube systems. *Journal of Applied Physics*, 101:084309, 2007.

[118] T. Vodenitcharova and L.C. Zhang. Mechanism of bending with kinking of a single-walled carbon nanotube. *Physical Review B*, 69(11):115410, 2004.

[119] G. Cao and X. Chen. Buckling of single-walled carbon nanotubes upon bending: Molecular dynamics simulations and finite element method. *Physical Review B*, 73(15):155435, 2006.

[120] O. Lourie, D.M. Cox, and H.D. Wagner. Buckling and Collapse of Embedded Carbon Nanotubes. *Physical Review Letters*, 81(8):1638–1641, 1998.

[121] J.Z. Liu, Q. Zheng, and Q. Jiang. Effect of a Rippling Mode on Resonances of Carbon Nanotubes. *Physical Review Letters*, 86(21):4843–4846, 2001.

[122] A. Kutana and K.P. Giapis. Transient Deformation Regime in Bending of Single-Walled Carbon Nanotubes. *Physical Review Letters*, 97(24):245501, 2006.

[123] Q. Wang, K.M. Liew, X.Q. He, and Y. Xiang. Local buckling of carbon nanotubes under bending. *Applied Physics Letters*, 91:093128, 2007.

[124] H. Liang and M. Upmanyu. Axial-Strain-Induced Torsion in Single-Walled Carbon Nanotubes. *Physical Review Letters*, 96(16):165501, 2006.

[125] E. Ertekin and D.C. Chrzan. Ideal torsional strengths and stiffnesses of carbon nanotubes. *Physical Review B*, 72(4):45425, 2005.

[126] I. Arias and M. Arroyo. size dependent nonlinear elastic scaling of multi-walled carbon nanotubes. *Physical Review Letters*, 100(1):085503, 2008.

[127] W. Yu, W.X. Xi, and N. Xianggui. Atomistic simulation of the torsion deformation of carbon nanotubes. *Modelling and Simulation in Materials Science and Engineering*, 12(6):1099–1107, 2004.

[128] T. Dumitrica, M. Hua, and B.I. Yakobson. Symmetry-, time-, and temperature-dependent strength of carbon nanotubes. *Proceedings of the National Academy of Sciences*, 103(16):6105–6109, 2006.

[129] JY Huang, S. Chen, ZQ Wang, K. Kempa, YM Wang, SH Jo, G. Chen, MS Dresselhaus, and ZF Ren. Superplastic carbon nanotubes. *Nature*, 439 (7074):281, 2006.

[130] JY Huang, S. Chen, ZF Ren, ZQ Wang, DZ Wang, M. Vaziri, Z. Suo, G. Chen, and MS Dresselhaus. Kink formation and motion in carbon nanotubes at high temperatures. *Physical review letters*, 97(7):75501, 2006.

[131] BI Yakobson. Mechanical relaxation and intramolecular plasticity in carbon nanotubes. *Applied Physics Letters*, 72:918, 1998.

[132] F. Ding, K. Jiao, M. Wu, and B.I. Yakobson. Pseudoclimb and dislocation dynamics in superplastic nanotubes. *Physical review letters*, 98(7):75503, 2007.

[133] F. Ding, K. Jiao, Y. Lin, and B.I. Yakobson. How evaporating carbon nanotubes retain their perfection? *Nano Lett*, 7(3):681–684, 2007.

[134] H. Mori, S. Ogata, J. Li, S. Akita, and Y. Nakayama. Energetics of plastic bending of carbon nanotubes. *Physical Review B*, 74(16):165418, 2006.

[135] H. Mori, S. Ogata, J. Li, S. Akita, and Y. Nakayama. Plastic bending and shape-memory effect of double-wall carbon nanotubes. *Physical Review B*, 76(16):165405, 2007.

[136] AV Krasheninnikov and F. Banhart. Engineering of nanostructured carbon materials with electron or ion beams. *Nature Materials*, 6(10):723–733, 2007.

[137] T. Dumitrică and B.I. Yakobson. Strain-rate and temperature dependent plastic yield in carbon nanotubes from ab initio calculations. *Applied Physics Letters*, 84:2775, 2004.

[138] T. Dumitrică, H.F. Bettinger, G.E. Scuseria, and B.I. Yakobson. Thermodynamics of yield in boron nitride nanotubes. *Physical Review B*, 68(8):85412, 2003.

[139] J.D. Eshelby. Screw Dislocations in Thin Rods. *Journal of Applied Physics*, 24(2):176, 1953.

[140] M.J. Bierman, YK Lau, A.V. Kvit, A.L. Schmitt, and S. Jin. Dislocation-driven nanowire growth and Eshelby twist. *Science*, 320(5879):1060, 2008.

[141] J. Zhu, H. Peng, AF Marshall, DM Barnett, WD Nix, and Y. Cui. Formation of chiral branched nanowires by the Eshelby Twist. *Nature nanotechnology*, 3(8):477–481, 2008.

[142] KS Nagapriya, O. Goldbart, I. Kaplan-Ashiri, G. Seifert, R. Tenne, and E. Joselevich. Torsional Stick-Slip Behavior in WS_ {2} Nanotubes. *Physical review letters*, 101(19):195501, 2008.

[143] HM Lawler, JW Mintmire, and CT White. Helical strain in carbon nanotubes: Speed of sound and Poisson ratio from first principles. *Physical Review B*, 74(12):125415, 2006.

[144] D.-B. Zhang and T. Dumitrică. Elasticity of ideal single-walled carbon nanotubes via symmetry-adapted tight-binding objective modeling. *Applied Physics Letters*, 93:031919, 2008.

[145] I. Kaplan-Ashiri, SR Cohen, K. Gartsman, R. Rosentsveig, G. Seifert, and R. Tenne. Mechanical behavior of individual WS2 nanotubes. *Journal of Materials Research*, 19(2):454–459, 2004.

[146] KS Nagapriya, S. Berber, T. Cohen-Karni, L. Segev, O. Srur-Lavi, D. Tománek, and E. Joselevich. Origin of torsion-induced conductance oscillations in carbon nanotubes. *Physical Review B*, 78(16):165417, 2008.

[147] D.-B. Zhang, RD James, and T. Dumitrică. Dislocation onset and nearly axial glide in carbon nanotubes under torsion. *The Journal of chemical physics*, 130:071101, 2009.

[148] D.-B. Zhang, T. Dumitrică, and G. Seifert. Helical Nanotube Structures of MoS_ {2} with Intrinsic Twisting: An Objective Molecular Dynamics Study. *Physical review letters*, 104(6):65502, 2010.

[149] L. Yang and J. Han. Electronic structure of deformed carbon nanotubes. *Physical review letters*, 85(1):154–157, 2000.

[150] A. Rochefort, P. Avouris, F. Lesage, and D.R. Salahub. Electrical and mechanical properties of distorted carbon nanotubes. *Physical Review B*, 60 (19):13824–13830, 1999.

[151] T. Chang. Torsional behavior of chiral single-walled carbon nanotubes is loading direction dependent. *Applied Physics Letters*, 90:201910, 2007.

[152] N.G. Chopra, L.X. Benedict, V.H. Crespi, M.L. Cohen, S.G. Louie, and A. Zettl. Fully collapsed carbon nanotubes. *Nature*, 377(6545):135–138, 1995.

[153] M.F. Yu, M.J. Dyer, J. Chen, D. Qian, W.K. Liu, and R.S. Ruoff. Locked twist in multiwalled carbon-nanotube ribbons. *Physical Review B*, 64(24): 241403, 2001.

[154] M.F. Yu, T. Kowalewski, and R.S. Ruoff. Structural analysis of collapsed, and twisted and collapsed, multiwalled carbon nanotubes by atomic force microscopy. *Physical Review Letters*, 86(1):87–90, 2001.

[155] C.E. Giusca, Y. Tison, and S.R.P. Silva. Evidence for Metal-Semiconductor Transitions in Twisted and Collapsed Double-Walled Carbon Nanotubes by Scanning Tunneling Microscopy. *Nano Lett*, 8(10):3350–3356, 2008.

[156] J.Q. Lu, J. Wu, W. Duan, F. Liu, B.F. Zhu, and B.L. Gu. Metal-to-semiconductor transition in squashed armchair carbon nanotubes. *Physical review letters*, 90(15):156601, 2003.

[157] H. Mehrez, A. Svizhenko, MP Anantram, M. Elstner, and T. Frauenheim. Analysis of band-gap formation in squashed armchair carbon nanotubes. *Physical Review B*, 71(15):155421, 2005.

[158] D.-B. Zhang, RD James, and T. Dumitrică. Electromechanical characterization of carbon nanotubes in torsion via symmetry adapted tight-binding objective molecular dynamics. *Physical Review B*, 80(11):115418, 2009.

[159] LM Malard, J. Nilsson, DC Elias, JC Brant, F. Plentz, ES Alves, AH Castro Neto, and MA Pimenta. Probing the electronic structure of bilayer graphene by Raman scattering. *Physical Review B*, 76(20):201401, 2007.

[160] The shear strain on a C-C bond is the ratio between its circumferential displacement and its axial projection.

[161] I. Nikiforov, D.-B. Zhang, RD James, and T. Dumitrică. Wavelike rippling in multiwalled carbon nanotubes under pure bending. *Applied Physics Letters*, 96:123107, 2010.

[162] VB Shenoy, CD Reddy, A. Ramasubramaniam, and YW Zhang. Edge-stress-induced warping of graphene sheets and nanoribbons. *Physical review letters*, 101(24):245501, 2008.

[163] K.V. Bets and B.I. Yakobson. Spontaneous twist and intrinsic instabilities of pristine graphene nanoribbons. *Nano Research*, 2(2):161–166, 2009.

[164] X. Wang, Y. Ouyang, X. Li, H. Wang, J. Guo, and H. Dai. Room-temperature all-semiconducting sub-10-nm graphene nanoribbon field-effect transistors. *Physical review letters*, 100(20):206803, 2008.

[165] L. Ci, Z. Xu, L. Wang, W. Gao, F. Ding, K.F. Kelly, B.I. Yakobson, and P.M. Ajayan. Controlled nanocutting of graphene. *Nano Research*, 1(2): 116–122, 2008.

[166] J.S. Bunch, A.M. van der Zande, S.S. Verbridge, I.W. Frank, D.M. Tanenbaum, J.M. Parpia, H.G. Craighead, and P.L. McEuen. Electromechanical resonators from graphene sheets. *Science*, 315(5811):490, 2007.

[167] L. Sun, Q. Li, H. Ren, H. Su, QW Shi, and J. Yang. Strain effect on electronic structures of graphene nanoribbons: A first-principles study. *The Journal of chemical physics*, 129:074704, 2008.

[168] Y. Lu and J. Guo. Band gap of strained graphene nanoribbons. *Nano Research*, 3(3):189–199, 2010.

[169] Z. Liu, K. Suenaga, P.J.F. Harris, and S. Iijima. Open and closed edges of graphene layers. *Physical review letters*, 102(1):15501, 2009.

[170] J. Feng, L. Qi, J.Y. Huang, and J. Li. Geometric and electronic structure of graphene bilayer edges. *Physical Review B*, 80(16):165407, 2009.

[171] K. Wakabayashi, M. Fujita, H. Ajiki, and M. Sigrist. Electronic and magnetic properties of nanographite ribbons. *Physical Review B*, 59(12):8271–8282, 1999.

[172] We also considered a 0.1 eV third-nearest neighbor hopping in H_0, as in A.H. Castro Neto et al., *Rev. Mod. Phys.* **81**, 109 (2009). This model gives a similar results but with t_0 replaced by the sum of the nearest- and third-nearest neighbor hoppings. The value for the slope then becomes 10.7 eV. .

[173] D. Gunlycke and CT White. Tight-binding energy dispersions of armchair-edge graphene nanostrips. *Physical Review B*, 77(11):115116, 2008.

[174] M. Fujita, M. Igami, and K. Nakada. Lattice distortion in nanographite ribbons. *Journal of the Physical Society of Japan*, 66(7):1864–1867, 1997.

[175] The small quasi-bilayer coupling effect is not included. .

[176] M. Graf and P. Vogl. Electromagnetic fields and dielectric response in empirical tight-binding theory. *Physical Review B*, 51(8):4940–4949, 1995.

Appendix

Publications

1. Dong-Bo Zhang and T. Dumitrică, *Effective Tensional-Strain Driven Bandgap Modulations in Helical Graphene Nanoribbons*, Physical Review Letters (under review).

2. Dong-Bo Zhang and T. Dumitrică, *Effective Strain in Helical Rippled Carbon Nanotubes: A Unifying Concept for Understanding Electromechanical Response*, ACS Nano (at press).

3. Dong-Bo Zhang and T. Dumitrică, *Effective Strain-Driven Electromechanical Response in Helical Rippled Carbon Nanotubes*, Physical Review B (at press).

4. Dong-Bo Zhang, T. Dumitrică and G. Seifert, *Helical Nanotube Structures of MoS_2 with Intrinsic Twisting: An Objective Molecular Dynamics Study*, Physical Review Letters **104**, 065502 (2010).

5. I. Nikiforov, Dong-Bo Zhang, R.D. James, and T. Dumitrică, *Wavelike Rippling in Multiwalled Carbon Nanotubes under Pure Bending*, Applied Physics Letters **96**, 123107 (2010).

6. Dong-Bo Zhang and T. Dumitrică, *Modulating the Optical and Electronic Properties of Highly Symmetric Si Quantum Dots*, Nanotechnology **20**, 445401 (2009).

7. Dong-Bo Zhang, R.D. James, and T. Dumitrică, *Electromechanical Characterization of Carbon Nanotubes in Torsion via Symmetry Adapted Tight-Binding Objective Molecular Dynamics*, Physical Review B **80**, 115418 (2009). Selected for Virtual Journal of Nanoscale Science & Technology 20 (13), September 28, 2009.

8. Dong-Bo Zhang, R.D. James, and T. Dumitrică, *Dislocation Onset and Nearly Axial Glide in Carbon Nanotubes under Torsion*, Journal of Chemical Physics [Communications] **130**, 071101 (2009). Selected for Virtual Journal of Nanoscale Science & Technology 19 (9), March 2, 2009.

9. Dong-Bo Zhang, and T. Dumitrică, *Elasticity of Ideal Single-Walled Carbon Nanotubes via Symmetry-Adapted Tight-Binding Objective Modeling*, Applied Physics Letters **93**, 031919 (2008). Selected for Virtual Journal of Nanoscale Science & Technology 18 (6), August 11, 2008.

10. Dong-Bo Zhang, M. Hua, and T. Dumitrică, *Stability of Polycrystalline and Wurtzite Si Nanowires via Symmetry-Adapted Tight-Binding Objective Molecular Dynamics*, Journal of Chemical Physics **128**, 084104 (2008).

11. S.G. Hao, Dong-Bo Zhang, and T. Dumitrică, *Effect of Small Shape Changes on the Optical Response of Highly Symmetric Silicon Quantum Dots*, Physical Review B [Rapid Communication] **76**, 081305 (2007). Selected for Virtual Journal of Nanoscale Science & Technology 16 (10), September 3, 2007.

12. T. Dumitrică, Dong-Bo Zhang and M. Hua, *Nanomechanics of Silicon Nanowires via Symmetry-Adapted Tight-Binding and Classical Objective Molecular Dynamics*, Proceedings of the ASME International Mechanical Engineering Congress and Exposition **13**, PTS A and B, 1199-1203 (2009).

◇ **Research in the News** Nov, 2009, Nanotechweb.org: New routes to adjusting light from artificial atoms. *http://nanotechweb.org/cws/article/lab/40964*